β-DECAY HALF-LIFE OF THE *rp*-PROCESS WAITING-POINT NUCLIDE ^{84}Mo

By

Joshua Bradshaw Stoker

A DISSERTATION

Submitted to
Michigan State University
in partial fulfillment of the requirements
for the degree of

DOCTOR OF PHILOSOPHY

Chemistry

2009

ABSTRACT

β-DECAY HALF-LIFE OF THE rp-PROCESS WAITING-POINT NUCLIDE ^{84}Mo

By

Joshua Bradshaw Stoker

^{84}Mo is an even-even $N = Z$ nucleus lying on the proton drip line that is thought to be created during explosive hydrogen burning in Type I X-ray bursts in the astrophysical rapid proton capture (rp) process. ^{84}Mo is an important waiting point in the rp-process reaction sequence, determining mass abundance at and procession beyond $A = 84$ for stable isotopes on the proton-rich side of the valley of stability [1]. A previous experiment established the half-life of ^{84}Mo to be $3.7^{+1.0}_{-0.8}$ s [2]. However, treatment of the decay-chain parameters and the poor statistics accumulated during that study left questions about the statistical and systematic errors in the measurement. The half-life of ^{84}Mo has been re-measured using a concerted setup of the NSCL β Counting System (BCS) [3] and 16 detectors from the Segmented Germanium Array (SeGA) [4]. The BCS relies on a highly-segmented Si detector to correlate implantations and subsequent β decays on an event-by-event basis. The correlation method employed to deduce half-lives and other properties of the β decay required that the average time between implantations be larger than the half-life of the nuclide under study. Consequently, the overall implantation rate into this detector must be carefully controlled, without negatively affecting the typically low rate of the desired isotope. The recently constructed Radio Frequency Fragment Separator (RFFS) [5] at NSCL was used to purify ^{84}Mo based on relative time-of-flight differences between the beam species of interest, isotonic contaminants, and contaminants due to the overlap of low momentum tails of high-yield beam species. A half-life of 2.2(2) s was deduced for ^{84}Mo, based on a sample of 1037 implantations, more than 30 times larger than the previous study. The new half-life reduced the uncertainty in the amount of ^{84}Mo formed in the *rp* process, and the consequent amount of ^{84}Sr, to less than a factor 2. Implications of the new half-life on theoretical treatments of nuclear level density near $A = 84$ along $N = Z$ will also be discussed. The performance capabilities of the RFFS in rejecting unwanted isotopes associated with the production of ^{84}Mo will be reported as well.

ACKNOWLEDGMENTS

I must start with my advisor, Paul, for at least one very good reason: without my advisor I would not be writing this page. Paul aided my Ph.D. progress by honing my mind to elucidate nuclear properties via β decay, but his influence didn't stop there. Paul, I appreciate the group lunches, Tuesday morning basketball games, trips to your cottage, and your ability to keep nearly any meeting to one hour or less.

I will always remember the support and friendship from my β group contemporaries Weerasiri, Jill, and Heather. You have been and will continue to be a good friends. Weerasiri, I appreciate your jovial personality and the chance that to take many classes together. Jill and Heather, thank you for always having a smile on your faces and for always caring. I appreciate your support throughout graduate school, especially in executing my thesis experiment, which I could not have completed on my own.

I thank also Paul's previous students, both those that I interacted with and learned from directly, and those that left a legacy to build on. I am also grateful for my several officemates. Thank you for your insights and conversations to breakup many tense work days.

My family certainly has a place here also, even if I was constantly badgered by my younger sisters for choosing a school so far from home. I appreciate that all of you care for my success and were willing to do whatever was in your power to assist me. Mom and Dad, thank you for it all.

And every shrewd turn was exalted among men … and simple goodness, wherein nobility doth ever most participate, was mocked away and clean vanished.

THUCYDIDES

The more ignorant men are, the more convinced are they that their little parish … is an apex to which civilization and philosophy has painfully struggled up.

SHAW

TABLE OF CONTENTS

LIST OF TABLES

LIST OF FIGURES

CHAPTER 1

Introduction

^{84}Mo is a β-unstable even-even nucleus with an equal number of protons and neutrons ($N = Z$), located near the extreme of neutron-deficient stability on the chart of the nuclides. The half-life of ^{84}Mo is of order seconds, decaying through the emission of a positron. This starts a chain of decay that ends with the β-stable ^{84}Sr, which is found on earth. However, even the most intense natural processes on earth do not create the necessary conditions of temperature, density, and composition for the synthesis of nuclei. Consequently, we must look elsewhere for the production of short-lived isotopes that help to explain the chemical makeup of the world we experience every day.

Stellar nucleosynthesis [6] describes the formative mechanisms for many of the stable elements. For nuclei of $Z > 26$, it is convenient to separate the nuclei into three categories termed the s-, p-, and r-nuclides. These categories are correlated with the location of these nuclei on the valley of nuclear stability and their production mechanism: The s-nuclei are the stable and longest lived nuclei for each element that are formed in neutron capture reactions that occur at a slower rate than their β decay. The r-process nuclei are generally the heaviest isotopes of a given element that are formed by the rapid capture of neutrons in an explosive environment. The lightest stable isotopes for each element with multiple stable masses are exclusively *p*-nuclides. The determination of other nuclei being either mixed or exclusively categorized depends upon the β shielding caused by stable isotopes for a given mass number [6].

1.1 The Astrophysical *rp* Process

The discovery of X-ray binaries occurred in 1976 [7]. Space observatories were required to view the emissions of these high energy photons because their energy lies outside the visible region of the electromagnetic spectrum and does not penetrate the atmosphere [8]. X-ray binary systems provide the stellar reaction conditions for the *rp* process. The *rp* process begins with the accretion of hydrogen and helium rich matter onto neutron stars from nearby companion stars, as is illustrated in Figure 1.1. Gravitational energy is released in the form of X rays as matter reaches the surface of the neutron star. The matter is compressed as it forms an accretion disk and travels through the gravitational field gradient towards the neutron star, which eventually results in thermonuclear burning. The time evolution of an X-ray burst is characterized by a peak X-ray emission (thermonuclear burning) on top of a persistent X-ray flux (gravitational contraction). The tail of the burst peak is typically long relative to the rise time indicating explosive ignition and the gradual consumption of hydrogen as the burst proceeds. Understanding the mechanism of X-ray bursts provides information about the neutron stars involved [9], and is crucial to determining the relative abundances of stable isotopes formed during the burning process. Formally, the *rp* process is a sequence of (p,γ) reactions and intermingled β^+ decays beginning at ^{41}Sc (see Figure 1.2). The ^{41}Sc seed nuclei are produced by a series of fast (α,p) and (p,γ) reactions on CNO-cycle nuclei. The alternating (α,p) and (p,γ) reactions up to ^{41}Sc result in a net consumption of 10 He nuclei per ^{41}Sc produced. The formation of ^{41}Sc

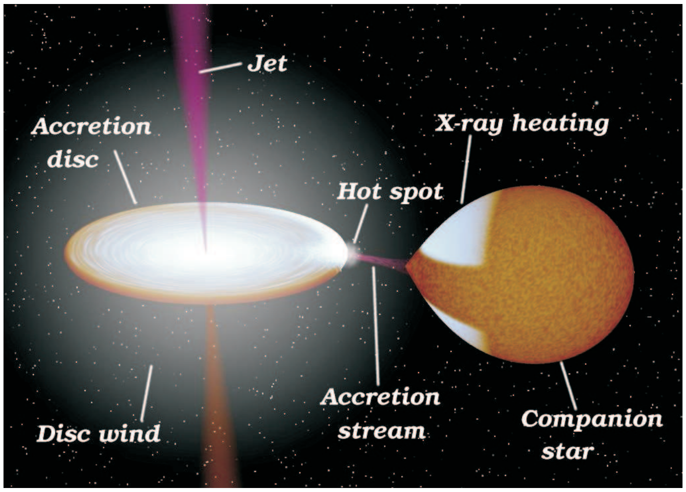

Figure 1.1. Artist's rendition of an X-ray binary system. Description in text. Modified from Ref. [11].

from all the available helium leaves 90 H nuclei per Sc atom prior to the sequence of rapid proton captures and β decays finishing out the nucleosynthesis, assuming that hydrogen and helium are accreted with a ratio typical of the 9 H to 1 He solar abundance ratio and that this ratio is maintained until burst ignition. An unchecked sequence of roughly 1:1 alternating proton captures and β decays could end the X-ray burst cycle somewhere in the region of $Z \approx 66$. However, the mass procession of the *rp* process is influenced by the properties of the binary star system; these properties govern the overall duration and peak temperature of the nuclear burning stage of X-ray bursts [10]. Schatz *et al.* [10] demonstrated that the *rp* process cannot proceed beyond ${}^{107,108}_{52}\mathrm{Te}$, since known ground state α emitters create a process ending cycle. In Figure 1.3 the reactions are shown that are calculated to occur at the closeout of the *rp*-process pathway where Te undergoes (γ,α), beginning an Sn-Sb-Te cycle [10].

Accurate modeling of X-ray bursts requires nuclear physics data for over a thousand isotopes. Masses, proton capture Q values, and β-decay half-lives are all necessary data for the *rp* process. To determine the proton capture rates, the masses and excitation energies of *rp*-process nuclides should be known within 10 keV [12]. While

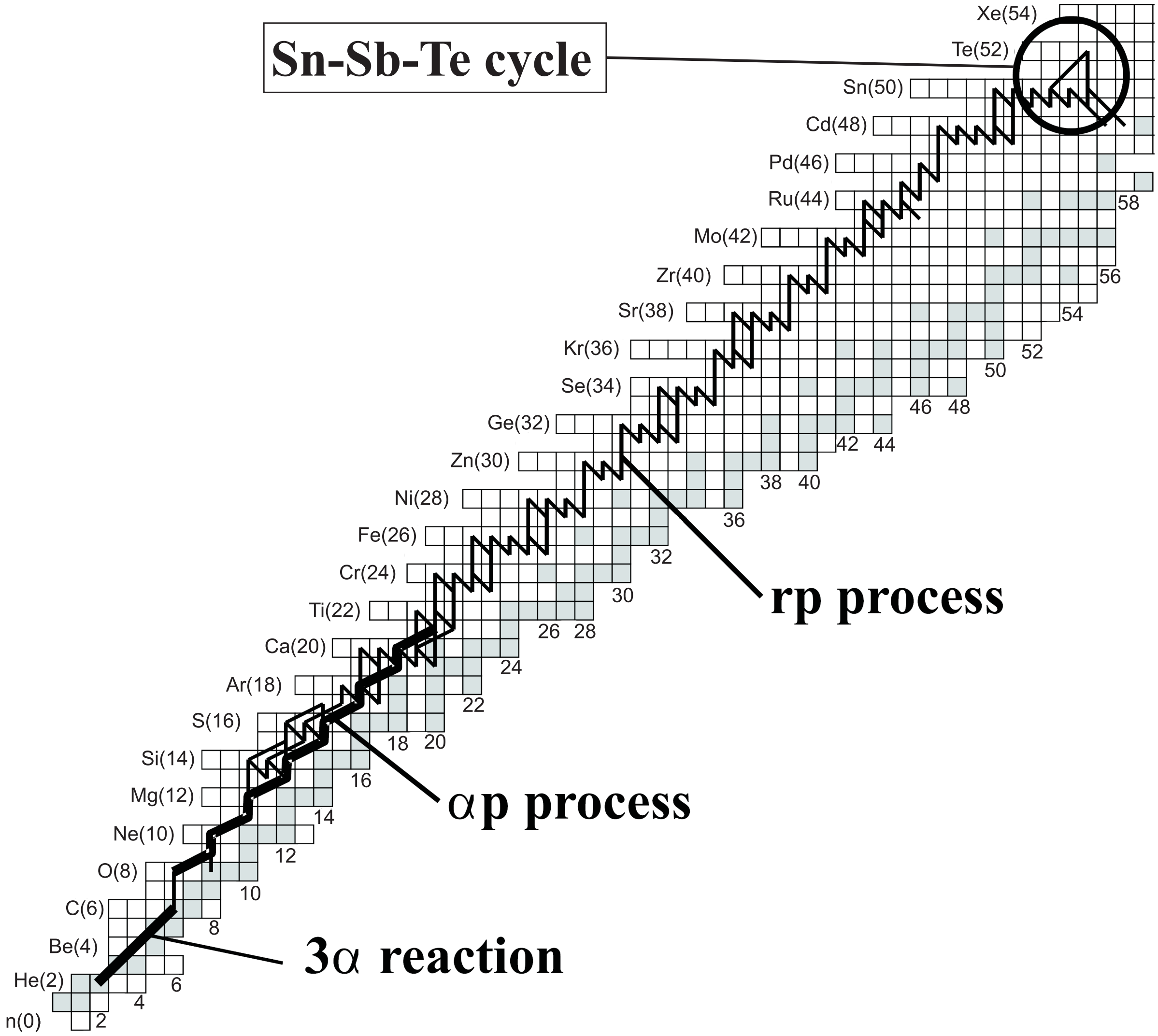

Figure 1.2. Reaction flow time integrated over a complete X-ray burst. The Sn-Sb-Te cycle is shown in detail in Figure 1.3. Modified from Ref. [9].

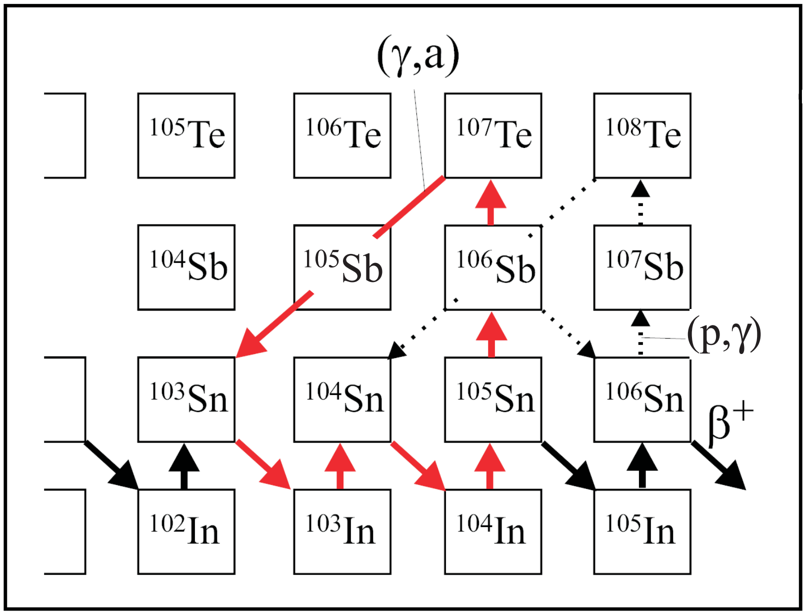

Figure 1.3. The reactions in the Sn-Sb-Te cycle during an X-ray burst. Reaction flows of more than 10% (solid line) and 1%-10% (dashed line) are shown. Modified from Ref. [9].

mass measurements are ongoing, mass uncertainties of proton-rich isotopes along the *rp* process path of order 100 keV are still present for many nuclei in this region, limiting the accuracy of proton capture rates in X-ray burst simulations. In addition, recent mass measurements [12] in the region $A = 80$ have demonstrated differences from previously adopted values of order 1 MeV in some cases. The accuracy of *rp* process rate calculations will improve as such discrepancies in the relevant masses are resolved. Concerning the overall rate, temperature independent β decays are the dominant contributor. Even-even nuclei along the *rp*-process path are in general longer lived with respect to β decay than the other *rp*-process reaction intermediates. At the proton drip-line, further mass processing through proton capture reactions is blocked until β decay takes place and proton capture can again proceed through bound nuclei. Such proton unbound nuclei are termed "waiting points" along the *rp*-process pathway. At higher and higher densities, reaction flow through these "waiting points" are increasingly bridged to higher masses also via two-proton (2p) capture. Schatz *et al.* [1], using the 1992 Finite Range Droplet Model for masses, demonstrated that the contribution of 2p capture to the overall reaction rate can become significant at densities of order 10^6 g/cm^3, resulting a faster procession to heavier nuclei. Mass procession continues until the burst reaction freezes out due to a lack of fuel. The unstable nuclei decay back to the valley of stability, making up the ash of the *rp* process.

1.1.1 X-ray Burst Nucleosynthesis

Certain *p*-nuclei are produced in abundances that are not explained by current nucleosynthesis models. For example, the solar abundances of the *p*-nuclei ^{92,94}Mo and ^{96,98}Ru are at odds with current nucleosynthesis models. X-ray bursts remain an intriguing process to possibly explain the solar abundances of these *p*-nuclei [10] because the mechanism is so suited to producing them. However, the high gravitational field in the vicinity of neutron stars hinders the ejection of all but the most energetic ash, limiting the contribution of X-ray binaries to solar abundances [13]. The amount emitted into the interstellar medium depends on the amount of *p*-nuclei produced in each burst, the frequency of burst occurrences that produce *p*-nuclei, and the fraction that escapes the gravitational field of the neutron star[14]. The bulk of nuclei synthesized in the *rp* process would not escape the gravitational field. Nevertheless, the amount of ejected material is still being debated and the composition of material produced in an *rp*-process event relies on experimental data, and in instances where these data are lacking, predictions from nuclear structure models [8]. The produced material that is not ejected remains in the star crust and consequently affects the later chemical evolution in the neutron star. The half-life of ^{84}Mo affects the mass processing above $A = 84$, and so is a necessary experimental parameter for modeling reaction flow. ^{84}Mo most directly determines the abundance of ^{84}Sr. Measuring the ^{84}Mo half-life would allow comparison of the corresponding ^{84}Sr overproduction factor to those determined for ^{92,94}Mo and ^{96,98}Ru.

1.1.2 ^{80}Zr-^{83}Nb Cycle

Schatz *et al.* [1] also investigated specific contributions of ^{84}Mo, a projected waiting point nucleus, to the *rp* process. The finite range droplet mass model (FRDM 1992) employed by Schatz *et al.* predicts substantially smaller α-binding energies near $Z = 42$ than other mass models [12]. Low α-binding energies correspond to high (p,α) cross sections, making the ^{83}Nb(p,α)^{80}Zr reaction more important in the reaction network. At high temperatures ($\geq$ 2 GK), a low α-separation energy for ^{84}Mo would induce a Zr-Nb cycle (see figure 1.4). Such a reaction cycle could significantly impact the *rp*-process outcomes, including reaction flow and mass processing beyond $A = 84$. The β-decay half-life for ^{80}Zr is essential to determining the flow into this Zr-Nb cycle, while the ^{84}Mo half-life governs leakage out of it. The half-life for ^{80}Zr was previously measured in an experiment performed at the Holifield Radioactive Ion Beam Facility [15]. The ^{80}Zr half-life was found to be shorter than the theoretical half-life employed by Schatz *et al.*, so that any bottleneck in this region will be determined largely by the β-decay half-life of ^{84}Mo [16]. The previously measured ^{84}Mo half-life of $3.7^{+1.0}_{-0.8}$ s is longer than the 1.1 s value used by Schatz [1], which would make the Zr-Nb cycle bottleneck more pronounced than predicted.

1.2 Shape Deformation Along $N = Z$

Given the importance of the heavy $N = Z$ nuclei in astrophysical processes, it is useful to review the nuclear structure of these nuclei. Deformed nuclei in general exhibit different single-particle level spacing and higher level densities than spherical nuclei. Single-particle levels, level densities and nuclear masses are important ingredients for

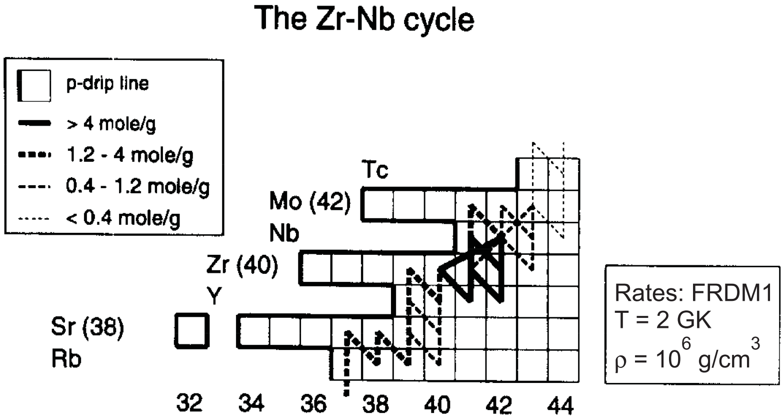

Figure 1.4. The time integrated reaction flow for the Zr-Nb cycle at a density of 10^6 g/cm^3 and a temperature of 2 GK. The legend shows the limits of the proton drip-line as well as the density of reaction flow. Taken from Ref. [1].

calculating proton-capture rates and β-decay half-lives [1]. The ratio of the 4^+ and 2^+ yrast state energies [$R_{4/2} \equiv E(4_1^+)/E(2_1^+)$] can be used as an indicator of shape deformation in even-even nuclei, with a smaller value representing a less deformed nucleus [17]. The $R_{4/2}$ ratio for even-even nuclei along the $N = Z$ line reveals a deformation maximum at ^{76}Sr and ^{80}Zr (see Fig. 1.5) [18]. The smaller $R_{4/2}$ ratio of 2.52 for ^{84}Mo marks the beginning of a transition towards the presumed spherical, doubly magic ^{100}Sn.

Theoretical predictions for the β-decay half-life of ^{84}Mo within the Quasi-particle Random Phase Approximation (QRPA) vary from 2.0 s by Sarriguren *et al.* [21] to 6.0 s by Biehle *et al.* [22]. Fig. 1.6 shows a comparison of the half-lives calculated by Sarriguren *et al.* (QRPA-Sk3, QRPA-SG2) and Biehle *et al.* (QRPA-Biehle) with experiment. The principle difference between these theoretical approaches is the set of nuclei used to calibrate the self-consistent interaction parameters for the particle-particle coupling strength and the nuclear deformation.

The QRPA-Biehle prediction relies on the nuclei ^{88,90}Mo, ^{92}Ru, and ^{94}Pd, which do not exhibit the same level of deformation ($2.1 \leq R_{4/2} \leq 2.23$) [23, 24, 25, 26] as

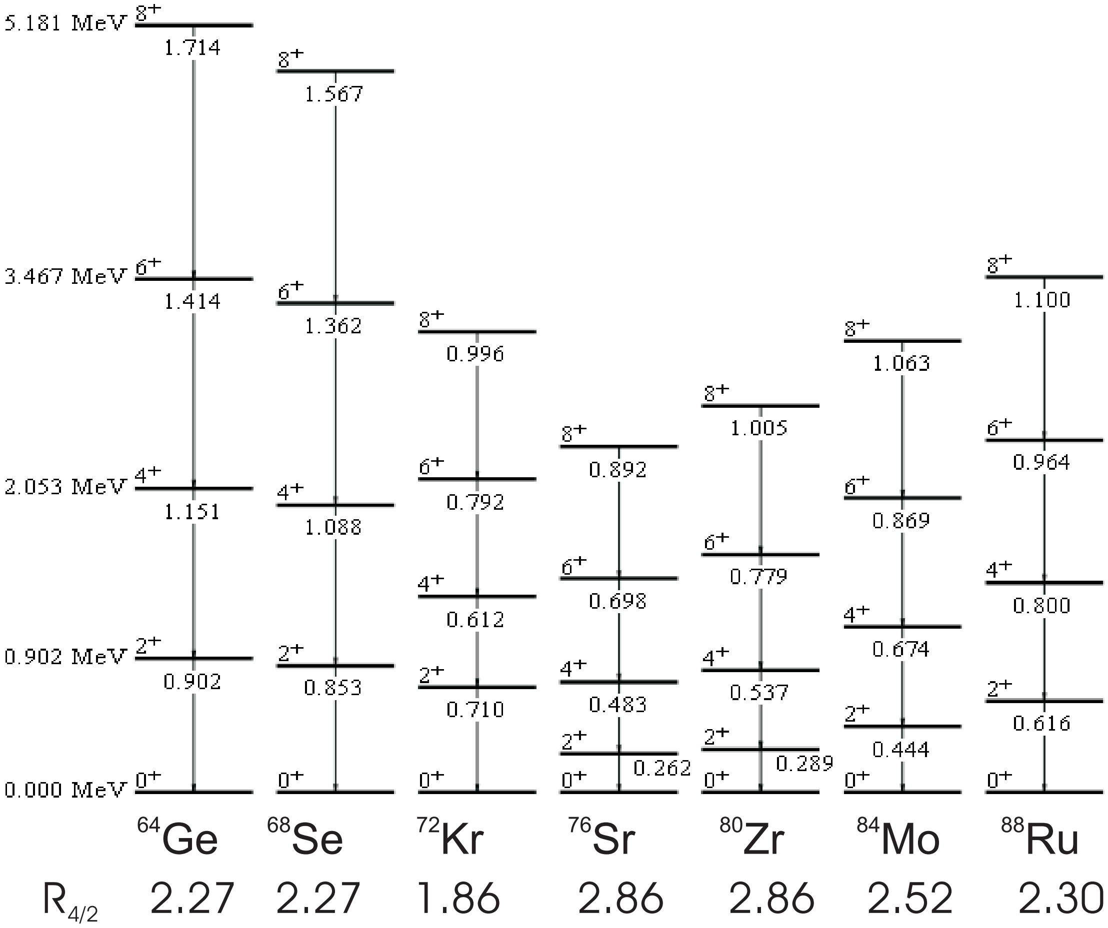

Figure 1.5. Yrast states up to 8^+ in even-even N=Z nuclei. The transition energies are given in keV. $R_{4/2}$ ratios are shown just below 0^+ state. Modified from Ref. [19, 20]

that observed in the $N = Z$ region near $A = 80$, lengthening the predicted half-lives. On the other hand, the self-consistent parameters for the QRPA-Sk3 and QRPA-SG2 cases were derived from experimental data from nuclei in the region of interest, and mostly reproduce the experimental half-lives using self-consistent deformations that minimize the energy. The previously measured half-life of ^{84}Mo reported by Kienle *et al.* [2] falls between the two calculations. This would imply a level of deformation unique to the mass region, perhaps inconsistent with the observed trend of measured $R_{4/2}$ ratios in the even-even $N = Z$ nuclei.

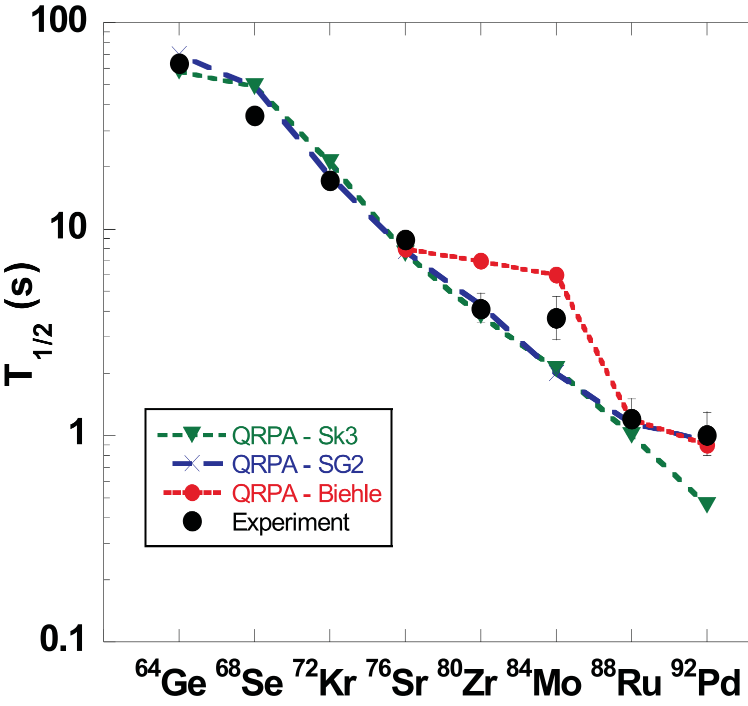

Figure 1.6. Half-lives of even-even $N = Z$ nuclei ($A = 64 - 92$) deduced using the QRPA. Details of different theoretical self-consistent parameters are given in text [21, 22]. Theoretical predictions are compared to reported experiment values for $A = 64, 68, 72, 76, 80$ [27] and $A = 84, 88, 92$ [2].

1.3 Previous ^{84}Mo Measurement

The previous ^{84}Mo half-life measurement reported by Kienle *et al.* provides only a few details on the measurement and treatment of the background [2, 28]. It is difficult to draw a conclusion about the accuracy of the measurement based on the published information but there are indications from subsequent work that some of the reported half-life values measured by Kienle *et al.* are too long [15, 29]. The half-life of ^{84}Mo was reported as $3.7^{+1.0}_{-0.8}$ s in a set of multiple β-decay half-lives obtained by a maximum likelihood analysis [30] that accounted for the decay contribution of the parent, daughter, and granddaughter nuclei during a fixed observation time. The experimental setup employed a highly segmented Si detector system to correlate β decays to specific implantations. After each implantation and decay, the daughter nucleus remains in the detector system, and will subsequently decay if radioactive. Consequently, the background rate in each pixel is directly related to the implantation rate into that pixel, as well as the number of β decays that must occur for each parent to reach β stability. The β decays from previous implantations are the chief source of background in these systems. Neither the measured background rate nor a method to approximate the background rate is mentioned in the work by Kienle *et al.* [2]. The reliability of their fitting method was demonstrated by separately fitting the previously known β-decay mean lifetimes of the ^{78}Y ground and isomeric states. Kienle *et al.* reported half-life values of 55^{+9}_{-6} ms and 5.7(7) s that agreed well with the previously measured values of 55(12) ms [31] and 5.8(6) s [32] for the ^{78}Y ground and isomeric states, respectively.

This good agreement for ^{78}Y was used by Kienle *et al.* to validate their half-lives deduced for other isomeric and ground state parent decay. However, this example does not ensure that the Kienle *et al.* half-lives determined from multi-generation decay chains are similarly correct. The Kienle *et al.* report also leaves out the values of the daughter and granddaughter decay generation half-lives provided for each parent decay fit. Such details are necessary to reproduce the results reported in the Kienle *et al.* study.

Table 1.1. Experimental half-lives determined by Kienle *et al.* [2] compared with [15, 29] β-γ correlated measurements.

Nucleus	J$^{\pi}$	Kienle *et al.* [2]	β-γ correlated
^{80}Zr	(0^{+})	$5.3^{+1.1}_{-0.9}$	$4.1^{+0.8}_{-0.6}$ [15]
^{93}Rh	$(9/2^{+})$	$13.9^{+1.6}_{-0.9}$	$11.9^{+0.7}_{-0.7}$ [29]
^{92}Rh	$(\geq 6^{+})$	$5.6^{+0.5}_{-0.5}$	$4.66^{+0.25}_{-0.25}$ [29]
^{91}Rh	$(9/2^{+})$	$1.7^{+0.2}_{-0.2}$	$1.47^{+0.22}_{-0.22}$ [29]

The relative rates of background and isotope decays are important for gauging potential contributions of systematic error to the deduced half-life. A log-linear plot of parent-decay activity vs. decay time gives a straight line with a slope determined by the half-life. The slope becomes less steep for longer parent half-lives. Resolving the slope of a parent decay-curve from background becomes increasingly difficult as the parent decay constant decreases and the background rate increases. Having relatively few events in the decay curve exacerbates this problem. High background rates impact the slope of the fit, of course, always leading to a half-life value that is too long. The number of implantations collected in the Kienle *et al.* study are available for each analyzed isotope in a dissertation [28], but the unreported β detection efficiency prevents an estimate of the observed number of β events. β detection efficiencies may have been anywhere from 30-70% for the system employed in the Kienle *et al.* study. Counts of 40 and 80 β events for the respective ^{78}Y ground and isomeric states are estimated based on a β efficiency of 40% and no contribution from background or daughter decay events. The β decay correlation time following each ^{78}Y implantation is not provided so it is not possible to determine the contribution of ^{78}Sr daughter or the contribution of background events, which are not reported. The half-life of ^{78}Sr is 2.65 min, which would not impact a fit to either the ^{78}Y ground or isomeric state.

However, the daughter half-lives of some of the other nuclei in the Kienle *et al.* study, including ^{84}Mo, are short enough to impact a fit to the parent decay. In addition, the half-life of the ^{84}Mo daughter has since been re-measured. Though the daughter half-life used in the Kienle *et al.* fit was not reported, it is likely that Kienle *et al.* used the previously published value of 12(3) s [33], which is longer than the newer value of 9.5(1.0) s [34]. Given identical data sets, using a longer daughter half-life to fit multiple decay generations will yield a longer value for the extracted parent half-life. Extending the β efficiency approximation of 40% to ^{84}Mo indicates that 14 decay events should have been observed from the 37 reported implantations [28]. The half-life of the ^{84}Mo daughter, ^{84}Nb, is relatively short. This assures that some portion of those 14 β events are from the daughter, consequently reducing the actual number of parent decays. The low number of β events collected from ^{84}Mo decay would make extracting an accurate half-life difficult in any background environment. Without knowing the β decay correlation time or background rate, the parent half-life fitting conditions cannot be accurately reproduced.

The probability density functions in the maximum likelihood fit used by Kienle *et al.* are intended to deconvolute the decay events correlated to a single nucleus into parent, daughter, granddaughter, and background decay components. The extracted half-life represents a half-life deduced solely from parent decay events if: 1) the probability density functions are correctly formed, and 2) the fixed input parameters are correct. Another approach to removing non-parent decay generation events and background is through selecting only β events that occur in coincidence with γ rays in the daughter nucleus. The results of subsequent measurements of the half-lives for ^{80}Zr [15] and ^{91,92,93}Rh [29], using γ gating for background suppression, are shown in Table 1.1. These background-suppressed measurements are all systematically lower than the Kienle *et al.* values, at times by more than 1σ, suggesting a systematic error due to background and/or non-parent decay events in the Kienle *et al.* study.

1.4 Re-measurement of the ^{84}Mo Half-Life

The potential systematic uncertainty in the Kienle *et al.* $T_{1/2}$ values along $N = Z$ could have a dramatic impact on the *rp*-process simulations. This dissertation details a re-measurement of the $T_{1/2}$ value of ^{84}Mo. The goal was to determine the accurate ^{84}Mo half-life within an uncertainty of better than ± 0.2 s, a factor 5 improvement over the previous measurement. The measurement was performed at NSCL with a concerted setup of the NSCL β Counting System (BCS) and 16 detectors from the Segmented Germanium Array (SeGA) aimed at reducing the background by obtaining a γ-gated decay curve. Achieving the optimum performance with this setup for fragment-β-γ correlation requires a balance among the overall implantation rate, the half-lives of the implanted species of interest, and the number of daughter decays by each implanted isotope to reach β stability. Production of ^{84}Mo through projectile fragmentation produces a myriad of (unwanted) fragments that dominated the beam composition due to the exotic nature of the desired product, inflating the overall implantation rate to unmanageable levels. Additional selective beam reduction was required beyond that usually achieved at NSCL with the A1900 separator. Therefore a new device, the NSCL Radio Frequency Fragment Separator (RFFS), was implemented to reduce the beam rate of proton-rich nuclei to make the measurement of fragment-β correlations for ^{84}Mo experimentally tractable.

The details of experimental conditions, setup, and results are provided in later chapters as follows: Chapter 2 provides a review of the physics principles relevant to this dissertation. The experimental apparatus, setup, and calibration procedures are described in Chapter 3. Chapter 4 entails the identification and isolation of each principle nucleus produced during this study. Chapter 5 details of the experimental analysis and astrophysical and theoretical implications based on the new half-life result for ^{84}Mo. Chapter 6 provides a brief summary and outlook.

CHAPTER 2

Technique

The goal of the present study was to measure the β-decay half-life of ^{84}Mo and then determine the rate of mass processing above $A = 84$ in the astrophysical *rp*-process. This chapter discusses the β and γ decay processes relevant to the ^{84}Mo measurement.

2.1 β Decay

Any process of radioactive decay where the nuclear mass number A remains constant while the atomic number Z changes is classified as β decay. In general, nuclear species β decay along a given isobar chain until they reach the most stable nuclide (lowest mass). Relative nuclear stabilities can be calculated from the mass of a given nucleus with the expression:

$$M_Z(Z, A) \cdot c^2 = [Z \cdot M_H + (A - Z) \cdot M_N] \cdot c^2 - E_B \tag{2.1}$$

where the masses in the expression are multiplied by c^2 to express their values in units of energy. $\mathrm{M}_Z \cdot c^2$ is the atomic mass and $\mathrm{M}_H \cdot c^2$ and $\mathrm{M}_N \cdot c^2$ are masses of the hydrogen atom (938.791 MeV) and the neutron (939.573 MeV), respectively [35]. E_B is the nuclear binding energy which contains all the information on the relative stability of the nuclei and can be expressed using the semi-empirical mass formula:

$$\begin{aligned} E_B &= c_1 A \cdot \left[1 - k\left(\frac{N-Z}{A}\right)^2\right] - c_2 A^{2/3} \cdot \left[1 - k\left(\frac{N-Z}{A}\right)^2\right] \\ &\quad -c_3 Z^2 A^{-1/3} + c_4 Z^2 A^{-1} + \delta. \end{aligned} \tag{2.2}$$

When E_B is expressed in units of MeV, the coefficients take on the following values: $c_1 = 15.677$ MeV, $c_2 = 18.56$ MeV, $c_3 = 0.717$ MeV, $c_4 = 1.211$ MeV, and $k = 1.79$. δ represents the nuclear pairing energy and takes on the value of $+(\text{-})11/A^{1/2}$ MeV for even-even (odd-odd) nuclei, and is zero for all other nuclei. Equation (2.1), with Equation (2.2) substituted for E_B, can be shown to be second order in Z and is a parabola for constant A. One can find the minimum Z along an isobar chain through differentiation of Equation (2.1) with respect to Z, holding A constant. The set of nuclei that lie at the minimum of each mass parabola form what is called the valley of β stability. Nuclei that are not at the bottom of the mass (energy) parabola are unstable and may decay towards stability through the weak process, or β decay.

There are three types of β decay that occur depending upon the relative position of the nucleus relative to the most stable isotope and atomic number.

$$\beta^-(M_Z > M_{Z+1}) \;:\; {}^A_Z X_N \rightarrow {}^A_{Z+1} Y_{N-1} + \beta^- + \overline{\nu} + Q_\beta \tag{2.3}$$

$$\text{Electron Capture}(M_Z > M_{Z-1}) \;:\; {}^A_Z X_N + e^- \rightarrow {}^A_{Z+1} Y_{N-1} + \nu + Q_\beta \tag{2.4}$$

$$\beta^+(M_Z > M_{Z-1} + 2m_e) \;:\; {}^A_Z X_N \rightarrow {}^A_{Z-1} Y_{N+1} + \beta^+ + \nu + Q_\beta \tag{2.5}$$

where m_e is the electron mass, e^- an electron, $\beta^\pm$ is a β particle, ν is a neutrino, and $\overline{\nu}$ an anti-neutrino. Q_β is the difference in mass (energy) between the ground states of the decaying parent nucleus and the daughter. M_Z represents the atomic mass of a nucleus with Z protons. β^+ decay is possible only if the decay energy exceeds $2m_e\mathrm{c}^2$ (1.02 MeV), the amount of energy necessary to create an electron/positron pair. Competition between Electron Capture (EC) and β^+ decay increasingly favors β^+ decay as Q_β increases above the 1.02-MeV threshold.

Table 2.1. β-decay selection rules.

Decay Mode	ΔI	$\Delta\pi$	Δl
Allowed	0,1	no	0
First-forbidden	0,1,2	yes	1
Second-forbidden	2,3	no	2
Third-forbidden	3,4	yes	3
Fourth-forbidden	4,5	no	4

The energy of the positron emitted during β^+ decay is attenuated through interaction with the surrounding medium and it eventually becomes thermalized. At this point, the positron will combine with an electron and annihilate, producing two 511 keV γ rays that propagate in opposite directions. The principle nuclei produced in the present study are β^+ emitters and the presence of their associated 511-keV γ rays was seen throughout the β-delayed γ spectra.

Conservation Laws

Conservation laws dictate that the angular momentum, shared by the recoiling parent nucleus and emitted β and neutrino, must be conserved during β decay. This conservation governs the likelihood of decay from the initial ground state to final states of particular spin (J) and parity (π) in the daughter. Decays are classified into two main types: Gamow-Teller (GT) and Fermi, depending on the orientation of the spins of the created β particle and neutrino being parallel (GT) or anti-parallel (Fermi). Where there is no change in the orbital angular momentum, $\Delta l = 0$, the decays are termed "allowed." The change in total nuclear spin, ΔI, in this case is determined solely by the vector coupling of the β particle and neutrino. Possible values for ΔI are then 0 and 1 for GT decay, and 0 for Fermi decay. The feature that $\Delta\pi = (-1)^l$ forces the parity between the initial and final states to be the same for allowed decays.

Decays where $\Delta l > 0$ are termed "forbidden," but actually occur in nature with decreasing probability for each incremental increase in Δl. Forbidden decays are formally distinguished as first forbidden, second forbidden ... corresponding to $\Delta l = 1, 2 \ldots$. Possible values for ΔI must include the orbital angular momentum contribution to the β particle and neutrino vector coupling so that a Δl value of 1 would give ΔI values of 0 or 1 for Fermi decay and 0, 1, or 2 for GT decay. A summary of the selection rules associated with β-decay transitions are shown in Table 2.1.

β Decay Kinetics

A β-decay half-life determination requires monitoring the rate of β decays from a known sample as a function of time. The disintegration of a parent nucleus into a daughter nucleus through β decay is a first-order reaction with respect to the amount of the parent nucleus. Therefore, the β-decay rate of change of a radioactive sample of N parent nuclei into daughter nuclei per unit time ($-d[N]/dt$) is described by the product of the decay constant λ and the total number of parent nuclei in a given sample at time, t, and is defined as the activity (A) of a sample:

$$A = -\frac{d[N]}{dt} = N\lambda \tag{2.6}$$

$$\frac{N_t}{N_0} = e^{-\lambda t} \tag{2.7}$$

Integration of (2.6) and use of the boundary condition that $N = N_0$ at $t = 0$ yields (2.7), where t is time, N_0 is the number of parent nuclei at time zero, and N_t is the number of parent nuclei at time t. The half-life of a nucleus represents the average time needed for a parent sample to satisfy the condition $N_t/N_0 = 1/2$, and is therefore defined as:

$$t_{1/2} = \frac{ln2}{\lambda}. \tag{2.8}$$

The process of β decay may feed one or more states in the daughter nucleus, with a unique rate observed for the decay into each state. A partial rate constant can be defined for each transition if the branching ratio of β feeding into each state is known via the expression:

$$\lambda_i = BR_i \cdot \lambda \tag{2.9}$$

where λ_i is the rate of decay into a particular daughter state i and BR_i is the branching ratio into that state. The half-life of state i can then be found by replacing λ with λ_i in Equation (2.8), which will give a partial half-life, t_i, of the parent nucleus. The comparative half-life, relating to the "allowedness" of a particular transition, is commonly reported as the logft value, where t is the t_i for a particular state and f is the Fermi phase-space function, which depends on the endpoint energy of the β decay and the Z of the daughter nucleus. Empirical expressions for log$f$ are available for atomic numbers from $0 < Z \leq 100$ and endpoint energies from 0.1 MeV $< E_0$ $<$ 10 MeV. The expression used for the log$f$ value for a positron decay in this work was:

$$\log f_{\beta+} = 4.0\log E_0 + 0.79 - 0.007Z_D - 0.009(Z_D + 1)(\log\frac{E_0}{3})^2. \tag{2.10}$$

The maximum kinetic energy of the β^+ particle, E_0, is entered in MeV and Z_D is the atomic number of the daughter nucleus [35].

The decay of a nucleus far removed from β stability begins a decay chain of parent $\rightarrow$ daughter $\rightarrow$ granddaughter... until stability is reached. Bateman formulated a solution for the activity of the ith member of a chain based on the assumption that at $t = 0$ only the parent substance is present [35, 36]:

$$\lambda_i n_i(t) = \lambda_i \lambda_1 \lambda_2 \ldots \lambda_{i-1} n_1(0) \sum_{j=1}^{i} \frac{e^{-\lambda_j t}}{\prod_{\substack{k=i \\ k \neq j}} (\lambda_k - \lambda_j)} \tag{2.11}$$

where λ_1, λ_2, λ_3 are the decay constants of the parent, daughter, and granddaughter, respectively. $n_i(t)$ represents the number of nuclei present at time t for the parent

($i = 1$), daughter ($i = 2$), or granddaughter ($i = 3$). The total activity of the chain can be described by the sum of $\lambda_1 n_1(t) + \lambda_2 n_2(t) + \ldots + \lambda_i n_i(t)$. In this work up to three generations of a given decay chain need to be considered, so the expanded form of equation 2.11 is given for $i = 1$ to $i = 3$:

$$\lambda_1 n_1(t) = \lambda_1 n_1(0) e^{-\lambda_1 t} \tag{2.12}$$

$$\lambda_2 n_2(t) = \frac{\lambda_2 \lambda_1}{\lambda_2 - \lambda_1} n_1(0) \left[e^{-\lambda_1 t} - e^{-\lambda_2 t} \right] \tag{2.13}$$

$$\begin{aligned} \lambda_3 n_3(t) = \lambda_3 \lambda_2 \lambda_1 n_1(0) \Bigg[& \frac{e^{-\lambda_1 t}}{(\lambda_2 - \lambda_1)(\lambda_3 - \lambda_1)} + \\ & \frac{e^{-\lambda_2 t}}{(\lambda_1 - \lambda_2)(\lambda_3 - \lambda_2)} + \frac{e^{-\lambda_3 t}}{(\lambda_1 - \lambda_3)(\lambda_2 - \lambda_3)} \Bigg] \end{aligned} \tag{2.14}$$

Experimentally, the assumption for an isolated parent population generally does not hold, necessitating the addition of a background term in Equations (2.12), (2.13), and (2.14) to fit the total activity.

2.2 γ Decay

Many nuclear processes (i.e., β decay, α decay, neutron capture) leave the product nucleus in an excited state. γ-ray decay is the process by which an excited nucleus releases excess energy without undergoing transmutation. This process is governed by the electromagnetic interaction and is the emission of a photon with discrete energy. The excited states of nuclei, generally represented as X^* for a nuclear species X, have specific energies and character defined uniquely by the structure of a given nucleus. γ-ray decay is represented as:

$$^{A}X^{*} \quad \rightarrow \quad ^{A}X + \gamma.$$

γ rays are grouped in two categories for this work, those that are emitted from excited levels populated after β decay are termed "delayed," whereas those from excited-state decay of implanted nuclei prior to particle decay are termed "prompt." Prompt and delayed γ-ray emissions were monitored to elucidate the low-energy quantum states and serve as a background filter for β-decay half-life determinations. This work assigns γ rays to either β decay events or fragment implantation events based on the total energy and type of event in coincidence with the γ ray (discussed below). Coincidence filtering of the data stream through the use of "gates" in software was used in this work for the assignment of γ rays to either prompt or β-delayed γ-ray spectra.

γ-ray emission spectra consist of discrete lines corresponding to transition energies. The observed transitions vary between energies of 10 keV to 10 MeV. De-excitation schemes generally form a series of one or more transitions ending in the ground state. However, certain nuclei have energy states that are hindered from decaying due to some combination of parity, spin, or energy differences between the states. Relatively long lived excited state energy levels, generally with half-lives on the order of nanoseconds or longer, are known as isomeric states.

Understanding the different character of photons emitted during γ decay provides insight into the structure of the nucleus. The initial and final energy states of the nucleus have a definite angular momentum and parity, and so the photon emitted during the transition between these two states must conserve this momentum. The angular momentum of the initial and final states exists in discrete amounts as $I\hbar$. The change in angular momentum l is defined $l \equiv \Delta I = |(I_i - I_f)|\hbar$. $\Delta I = 0$ is, in fact, forbidden as every photon must carry at least one unit of angular momentum. The photon may take on higher values of ΔI so that $|(I_i - I_f)| \leq l \leq (I_i + I_f)$ represents the full range of allowed values of angular momentum for a photon. However, photons with larger values of l are progressively hindered.

The dependence of photon emission on parity can be understood through the physical relationship of electric and magnetic fields. Protons are charged particles with spatial and orbital distribution in the nucleus. Spatial rearrangement of protons alters the electric field within the nucleus, whereas orbital or axial alignment changes the associated magnetic field. The character of a particular decay is matched to the change in angular momentum and parity between the initial and final states of the decaying nucleus. The character can be labeled as an electric (El) or magnetic (Ml) transition for possible l values and $\Delta\pi$. Even l values for transitions with no parity change ($\Delta\pi$=no) require electric and odd values require magnetic transitions. The reverse is true for transitions where a change in parity occurs. This relation is described as:

$$\Delta\pi(El) = (-1)^{l} \tag{2.15}$$

$$\Delta\pi(Ml) = (-1)^{l+1} \tag{2.16}$$

The rate of γ-ray decay is inversely related to the angular momentum change, so the transition with the smallest l value usually dominates. The transition rates for a given character depend on the energy of the photon and the mass of the decaying nucleus.

Table 2.2. Weisskopf single-particle transition rates (Rates given in units of s^{-1}, E$_{\gamma}$ is in MeV). Table modified from Ref. [37].

	Transition Rate	
l	Electric	Magnetic
1	1.03×10^{14} A$^{2/3}$E$_{\gamma}^{3}$	3.15×10^{13} E$_{\gamma}^{3}$
2	7.28×10^{7} A$^{4/3}$E$_{\gamma}^{5}$	2.24×10^{7} A$^{4/3}$E$_{\gamma}^{5}$
3	3.39×10^{1} A^{2}E$_{\gamma}^{7}$	1.04×10^{1} A$^{4/3}$E$_{\gamma}^{7}$
4	1.07×10^{-5} A$^{8/3}$E$_{\gamma}^{9}$	3.27×10^{-6} A^{2}E$_{\gamma}^{9}$

Weisskopf derived separate expressions for the reduced magnetic and electric transition probabilities by assuming that the transitions result from the change of a single particle inside a nucleus of uniform density. These expressions can be evaluated for different l values to provide relative transition rates as a function of mass and decay energy. The Weisskopf single-particle transition rates for electric and magnetic transitions with l values from 1 to 4 are listed in Table 2.2. The rate equations show that for heavy nuclei an “$l+1$” electric transition can compete favorably with an “l” magnetic transition [37].

CHAPTER 3

Experimental Setup

3.1 Isotope Production

Radioactive species are created in stellar environments, and most exist only for a short time after their formation. For laboratory study at NSCL, radioactive nuclei are synthesized through fragmentation reactions between two stable species. A projectile nucleus is accelerated up to 40% the speed of light and impinged on a stationary target, fragmenting some fraction of the projectiles. Projectile fragmentation results in a cocktail mixture of fragments that was selectively filtered using the NSCL A1900 Fragment Separator and Radio Frequency Fragment Separator (RFFS) before being transported to the experimental endstation. This work measured β^+-decay half-lives by monitoring the time until β^+ emission after the implantation of a known parent nuclei in the detection system. The rate constant λ was extracted and a half-life determined from a fit of the β^+-decay activity as a function of time. All β unstable particles analyzed in this study were β^+ emitters. This chapter presents the experimental subsystems in detail utilized to produce ^{84}Mo and measure its half-life.

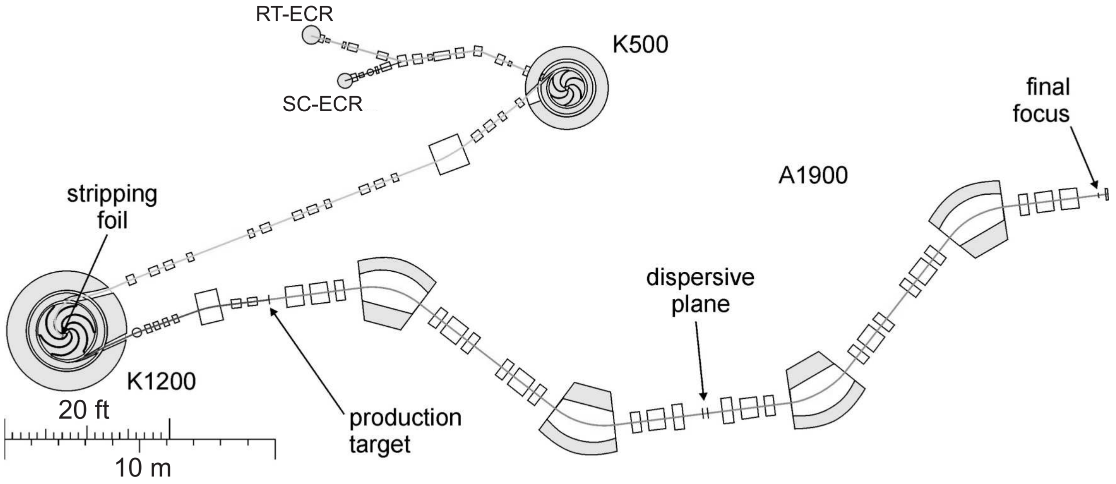

Figure 3.1. Layout of the K500, K1200, and A1900 components of the NSCL

3.1.1 Projectile Fragmentation

The nuclei for this study were produced via the fragmentation of ^{124}Xe projectiles accelerated to 140 MeV/nucleon in the NSCL coupled K500 and K1200 cyclotrons. The ^{124}Xe beam was impinged inelastically upon a 305 mg/cm^2 ^{9}Be target. A nucleus-nucleus collision fragmented the projectile through a two-step process of abrasion-ablation [38]. The abrasion step resulted in the formation of two or more fragments that are left in excited states, which may lose additional nucleons during a decay process termed ablation. Virtually all of the fragments retain enough forward momentum to be transported through the A1900 Fragment Separator [39].

3.1.2 A1900 Projectile Fragment Separator

The A1900 separation scheme employs a combination of magnetic rigidity and energy loss filtering, denoted Bρ-ΔE-Bρ, to discriminate the products of the intermediate energy collision by q, Z, and A. Magnetic rigidity is defined as:

$$B\rho = p/q = mv/q \tag{3.1}$$

Table 3.1. A1900 and K1200 settings for the ^{84}Mo production runs. The location of the target and dispersive image are indicated in figure 3.1. Effective values represent values input into LISE++ [40] simulations to approximate experimental conditions

Parameter	**Nominal Value**	**Effective Value**
K1200 Radiofrequency	23.14550 MHz	23.145 MHz
^{124}Xe Projectile Energy	140 MeV/u	142.35 MeV/u
^{9}Be Target Thickness	305 mg/cm^2	327.986 mg/cm^2
Dispersive Image Momentum Cut	1%	$0 \pm 29.5\,mm$
$B\rho_{1,2}$	2.9493 T· m	2.9493 T·m
Dispersive Image Al wedge	180 mg/cm^2	187.7 mg/cm^2
$B\rho_{3,4}$	2.5635 T·m	2.5635 T·m

where B is the magnetic field strength, ρ the radius of curvature, p the momentum, m the mass, v the velocity, and q the charge state of the ion. The first A1900 Bρ selects nuclei based on the mass-to-charge ratio because the fragmentation mechanism produces all nuclei with nearly the same initial velocity [37]. A wedge-shaped degrader is placed at the intermediate image of the A1900 to induce an energy loss, which is proportional to the square of the fragment nuclear charge, the fragment mass, and energy as

$$-\frac{\partial E}{\partial X} \propto \frac{AZ^2}{E} \tag{3.2}$$

The wedge position is indicated by the "dispersive plane" label in figure 3.1. By means of this wedge, the velocity, and therefore Bρ, is changed for all fragments prior to passing through the second half of the A1900.

Values for the first and second Bρ selection are set corresponding to the central momentum of a particular isotope, which was ^{84}Mo for this study. The specific settings for the projectile energy, target, and A1900 are listed in Table 3.1.

The fragment selection consisted of a cocktail beam of species matching the magnetic rigidity of ^{84}Mo. A simulation of the yields of the principle fragments produced in this study as a function of Bρ is shown in Figure 3.2. The simulated peak production Bρ for ^{84}Mo was slightly higher than the observed peak production Bρ. The shaded region in Figure 3.2 labeled "1% Δp/p cut" illustrates the range of Bρ values for the observed peak ^{84}Mo production and corresponds to the experimental B$\rho_{1,2}$ values listed in Table 3.1 accepted through the first A1900 Bρ selection. The yields of the principle beam contaminants are produced of order 10^5 times more than ^{84}Mo.

3.1.3 Radio Frequency Fragment Separator

The momentum distribution of nuclei produced in fragmentation reactions is asymmetric, resulting in a long low-momentum "tail" that overlaps the central momentum region of other products (see Figure 3.2). The central Bρ selection of neutron-deficient nuclei near the drip-line therefore overlaps with tails from more stable and consequently much more abundantly produced nuclei. The production rate from the low-momentum tails of more stable species exceeded the peak production rate of ^{84}Mo to such a degree that a decay experiment was not feasible without additional beam purification after the A1900. The installation of the NSCL RFFS enabled new experimental studies on the neutron-deficient side of β stability.

A schematic of the RFFS is shown in Figure 3.3. The RFFS [5] consists of two horizontally parallel plate electrodes 1.5 m long, 10 cm wide, and 5 cm apart installed inside a vacuum chamber attached to a straight section of beam line. An electric current supplied to a RF loop inserted into the chamber, such that the plane of the loop is oriented vertically. The electric current in the coil induces a magnetic field inside the chamber, with field lines that are in a plane perpendicular to the vertically oriented RF loop. The induced magnetic field forms a standing wave inside the chamber with a node located at the vertical center of the chamber; therefore the upper and lower halves of the chamber are always 180 degrees out of phase. The magnetic field induces an electric field that charges the upper and lower parallel plates with the opposite charge, creating a voltage potential across the plates with

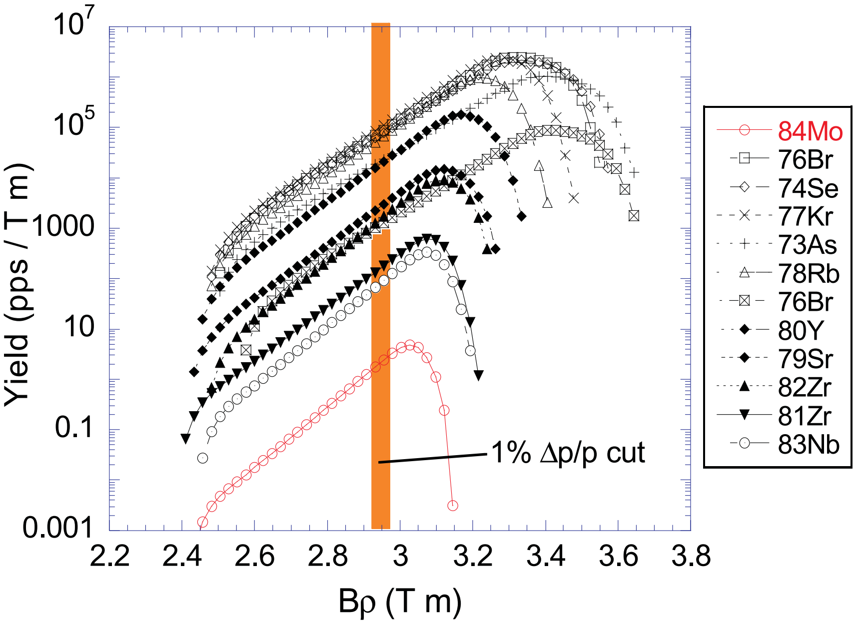

Figure 3.2. The isotope yield in particles per second (pps) as a function of Bρ for the principle isotopes in this study as simulated by LISE++ [40]. The asymmetric momentum distribution of ions came from the "phenomenological" model in the code with the effective values listed in Table 3.1.

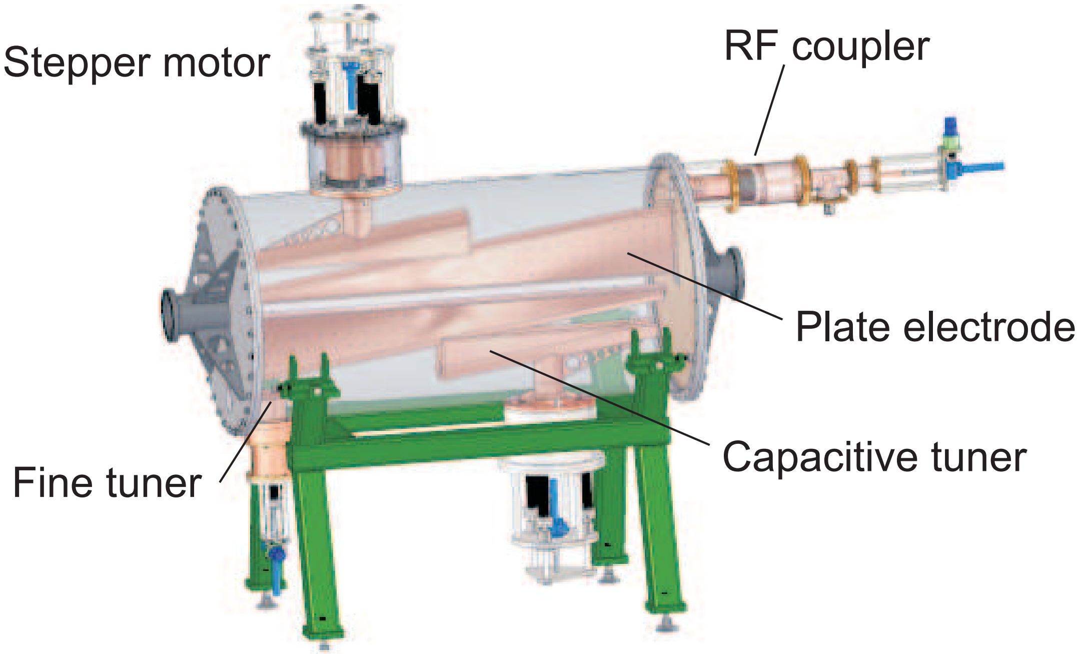

Figure 3.3. Schematic drawing of the RFFS. The outer wall of the RFFS chamber is transparent to make the components within visible. The parallel plate electrodes are the two larger triangularly shaped objects within the chamber. The smaller two triangular objects are capacitive tuners that control the amount of charge transferred to the plates from the RF loop, and may be adjusted by the stepper-motors attached at the upper and lower positions on the chamber. The RF loop is inserted from the RF coupler attached on the upper right part of the chamber. A fine tuner is attached at the lower left part of the chamber, which serves as a conductor to reduce the density of the induced electric field in the chamber. This fine tuner is wired to be automatically adjusted based on feedback from the resonant condition of the cavity i.e., to minimize the difference between the measured phase and the phase setting of the chamber. Figure modified from J. Ottarson.

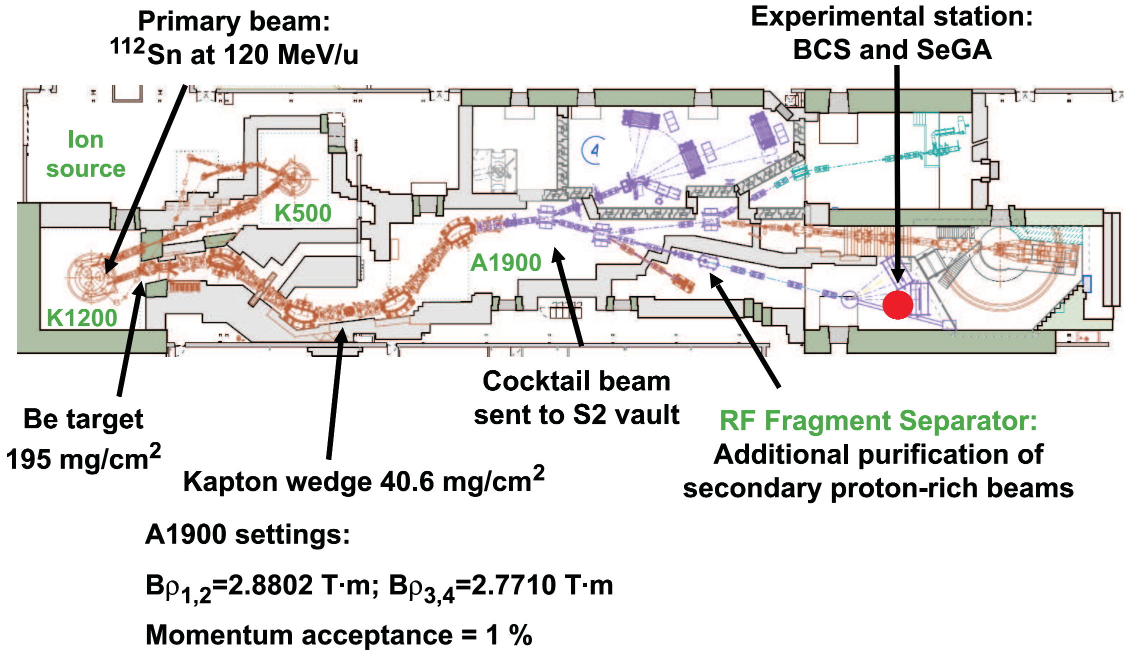

Figure 3.4. Overhead view of NSCL beamline with nominal operational settings indicated. The location of the RFFS in the S2 vault is shown just upstream of the BCS endstation with 16 detectors from SeGA.

an amplitude up to 100 kV$_{pp}$. A voltage of 47 kV$_{pp}$ was applied for this work. The polarity of the electric current supplied to the RF loop alternates in time at a frequency matched to that of the K1200 cyclotron, which was 23.145 MHz (see Table 3.1).

The RFFS is located approximately 51 meters downstream from the production target in the NSCL S2 vault, represented schematically in Figure 3.4. The drift space results in a time-of-flight (TOF) separation of about 5 ns between successive isotones under the reaction conditions described in Table 3.1. The settings for the second Bρ cut selected species with an average velocity of 11 cm/ns. An ion traveling the full 1.5 m length of the RFFS at this velocity takes roughly 1/3 of a RF period. The distribution of the beam species in TOF resulted in each fragment experiencing a different 1/3 of the voltage cycle, and therefore receiving a different vertical deflection.

After exiting the RFFS, the fragments drifted a distance of 5.38 m before entering a diagnostic box consisting of an adjustable vertical slit system sandwiched between two

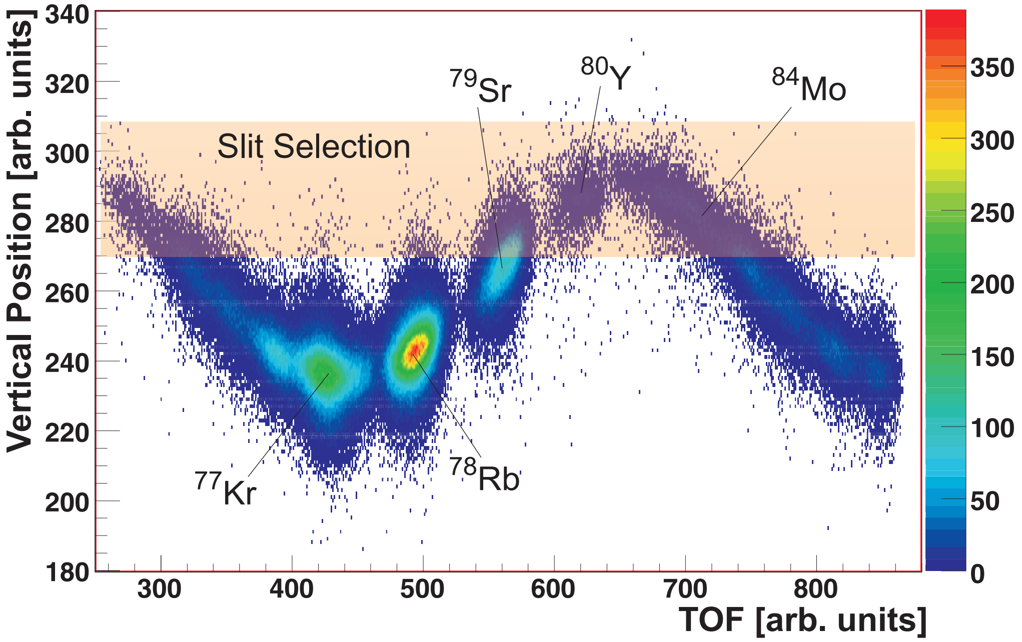

Figure 3.5. Plot of the vertical beam position as a function of TOF after the RFFS. The gray rectangle highlights the region allowed to pass through the vertical slit system in the experiment reported here. The fragment of interest, ^{84}Mo, was placed at the peak of the sinusoid so that the slits would block fragments that were not deflected by the RFFS, preventing damage to detectors at the end station in the event of a unexpected shutoff of the RFFS. Data were taken at the RFFS diagnostics port located 5.38 m downstream of the RFFS

retractable parallel-plane avalanche counters (PPAC), which are followed downstream by a retractable telescope of Si PIN detectors. The PPACs are position sensitive detectors used to set the slit position for selective removal of unwanted fragments. A plot of the vertical position of fragments in the secondary beam after deflection in the RFFS is shown in Figure 3.5. The mass-specific vertical deflection after fragments have drifted to the RFFS diagnostic box is apparent in the figure. The phase of the RFFS can be adjusted relative to the cyclotron RF so that the fragment of interest

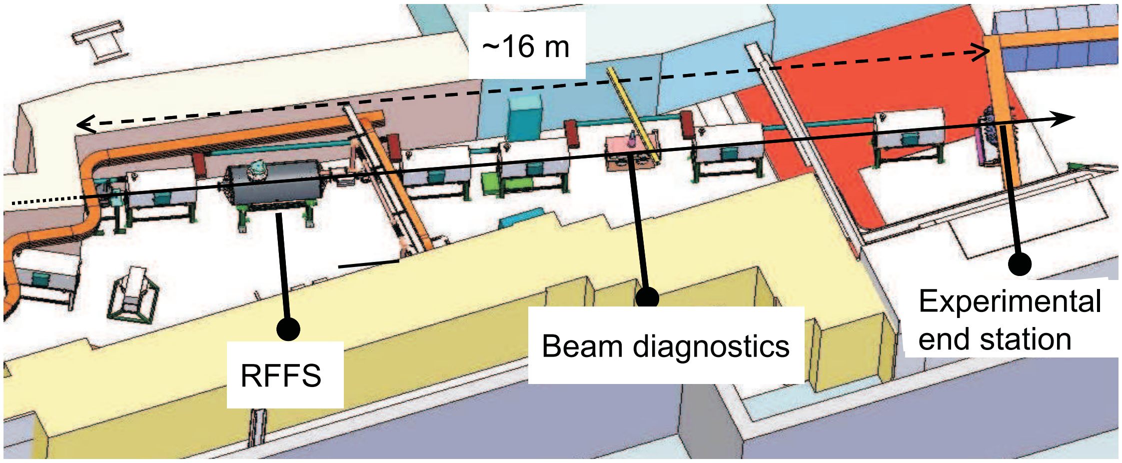

Figure 3.6. Overhead view of NSCL S2 vault showing a section of the beam line containing the RFFS, beam diagnostics port, and the experimental endstation.

can be placed at a trough, peak, or node of the sinusoid as desired. Placing the fragment of interest at the peak of the sinusoid accomplished two objectives. First, the location of the key contaminants ^{77}Kr and ^{78}Ru were then at the trough of the sinusoid and easily removed using slits. The vertical slits were narrowed to select out a specific deflection region that includes the fragment of interest and to eliminate key contaminants. Second, the slit position settings blocked fragments that occurred at the node of the sinusoid, i.e., fragments that were not deflected by the RFFS. Consequently, if the RFFS were to shut off unexpectedly the intense secondary beam would be blocked by the slits rather than be delivered to the experimental end station. Taking the full intensity of the beam into the end station would likely damage the detectors. Two beam steerers are located downstream of the RFFS diagnostic box and upstream of the experimental endstation to recenter the fragments onto the optical axis of the experimental endstation. The relative location of the RFFS, beam diagnostics port, beam steerers, and experimental end station within the S2 vault is shown schematically in Figure 3.6.

The separation capability of the RFFS is quite powerful as demonstrated by the

Table 3.2. Isotope specific and total beam rejection rates observed in this work. The rejection factor is reported as the ratio of RFFS$_{off}$/RFFS$_{on}$ for individual fragment yields. Rejection factors larger than 1 indicate a reduced transmission with the RFFS on. Rates for specific isotopes are given in particles per second per particle nanoAmperes of beam, normalized to the measured rate of ^{84}Mo. The beam intensity was attenuated when the RFFS was off (V = 0 kV) to preserve Si detector longevity. Comparative spectra representing data collected with the RFFS off and on are shown in Figures 3.7A and 3.7B, respectively.

	Normalized Rates*		
Isotope	**V = 0 kV slit = 50 mm**	**V = 47 kV slit = 10 mm**	**Rejection Factor**
^{84}Mo	1	1	1
^{83}Nb	15	16	1
^{82}Zr	80	40	2
^{81}Zr	20	10	2
^{80}Y	130	200	0.6
^{79}Sr	4000	85	47
^{78}Rb	18700	0.4	46700
^{77}Kr	13500	0.3	45000
^{76}Br	1150	15	77
^{74}Se	1980	5	400
^{73}As	700	630	1.1
Sum**	83	0.5	180
Primary Beam Intensity	0.8 pnA	10 pnA	

* Rates normalized to ^{84}Mo, 5x10^{-4} pps/pnA

** Absolute rate in pps/pnA

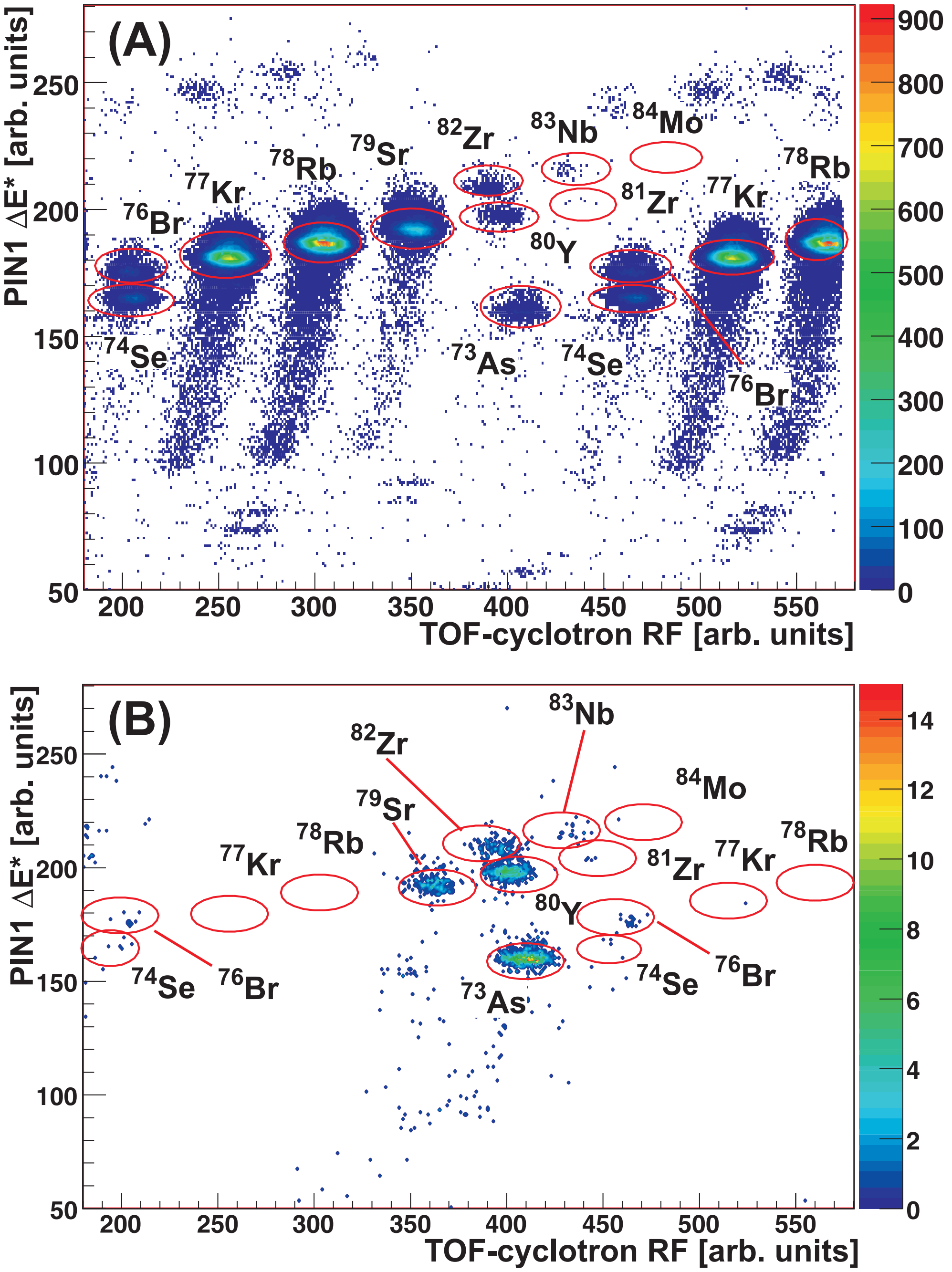

Figure 3.7. Correlated values of the PIN1 ΔE* versus the cyclotron RF triggered TOF for RFFS settings of (A) 0 kV with a 50 mm slit gap (fully open) and (B) 47 kV with a 10 mm slit gap (set production width). The positions of various isotopic components in the beam are indicated by ovals. The spectra are normalized to ∼470 counts of ^{80}Y for visual comparison. Further details can be found in Table 3.2.

values listed in Table 3.2 for the overall and isotope specific rejection factors observed during the production and isolation of ^{84}Mo. The importance of both the selective rejection by the device and the overall rejection rate of unwanted fragments is evident. Selective rejection for the copious contaminants ^{78}Rb and ^{77}Kr was of order 4.5x10^{4}, while the fragment of interest ^{84}Mo was not rejected at all by the RFFS. The overall rejection factor was 180. Fragment rates listed in Table 3.2 for a RFFS voltage of 47 kV$_{pp}$ were observed at the BCS endstation during the ^{84}Mo production runs. The representative spectra in Figure 3.7 of PIN1 ΔE* vs. TOF (ΔE* represents a relative ΔE calibration, as discussed in Sec. 3.2.1 under BCS Calibration) taken at the experimental endstation with the RFFS off and on demonstrate the removal of the chief contaminants ^{78}Rb and ^{77}Kr without the rate of ^{84}Mo being negatively affected.

3.2 Experimental Endstation

The selectively filtered beam was delivered to an experimental endstation located downstream of the RFFS in the NSCL S2 vault. The principle detector system was the NSCL β Counting System (BCS) [3]. The NSCL BCS is a Si detector telescope designed for the correlation of β decays with continuously implanted parent nuclei to extract lifetimes. This device has been augmented with additional Si and Ge detectors for β calorimetry and can be combined with additional systems for either neutron or γ-ray detection. For the experiment described here, the BCS was surrounded by 16 detectors from the NSCL Segmented Germanium Array (SeGA) [4] to detect γ rays emitted from nuclear excited states. The system is described in detail below.

3.2.1 β Counting Station

The BCS is a powerful detector system applied at NSCL to perform event-by-event correlations of fragment implantations with their subsequent β-decays. The system employed a Micron Semiconductor Double Sided Si Detector (DSSD) of dimension 995 μm × 4 cm × 4 cm segmented into 40 1-mm strips in both the x and y dimensions. This segmentation provided 1600 individual 1 mm × 1 mm pixels and enabled unique implantation analysis in each pixel. The DSSD was used to detect the energy and position of implantations and the energy loss and position of fast electrons emitted in β decay.

The successful correlation of implanted species with their β decays depends upon the rate and makeup of the beam cocktail. Following an implantation, a given pixel was monitored for fixed time determined by the half-life of the isotope in question. Should the overall implantation rate be too high, that pixel could receive another implantation prior to a β decay event occurring for the first implantation during the fixed correlation time. This convolutes the correlation process and introduces uncertainty into the analysis process. Both the A1900 and the RFFS were used to reduce the overall implantation rate to acceptable levels.

The makeup of the telescope is shown in figure 3.8. Three PIN detectors (PIN1-3), with PIN1 furthest upstream, served as active degraders upstream of the DSSD. The PIN detectors had thicknesses of 309, 488, and 503 μm. The active degrader thicknesses were selected such that fragments were stopped in the front 1/3 of the DSSD. Implanting fragments in the front 1/3 of the DSSD increased the probability of detecting the small ΔE signal of a β particle emitted in the downstream direction in the DSSD. PIN1 was used for the ΔE and TOF start signal that made up the particle identification (PID).

Six 5 cm × 5 cm Single-Sided Si Detectors (SSSD1-6), with SSSD1 furthest upstream, were mounted immediately downstream of the DSSD. Their thicknesses, proceeding in order from SSSD1, were: 975, 981, 977, 989, 988, and 985 μm, respectively. Each of the SSSDs was segmented into sixteen strips on one face. The SSSDs were arranged so that successive detector segmentation alternated in the x and y directions, beginning with SSSD1 strips parallel to x. Higher than normal noise levels observed in SSSD6 rendered this detector unusable during the experiment. The detector was left in the BCS chamber, but was disconnected from the analog electronics hardware. A Ge detector was placed at the end of the detector stack to provide a veto for light particles traversing the BCS. However, instability in the DSSD leakage current was observed during the cool down of the Ge detector to $-140\,^{\circ}$C. Consequently, the Ge detector was left in the BCS telescope uncooled and unbiased.

BCS Electronics

The DSSD was used to detect β and implantation events over a wide energy range. β particles that traverse the full thickness of the DSSD deposit energy of order 200 keV, whereas implanted fragments deposit GeV's of energy. This large dynamic range of signals from the DSSD were processed with MultiChannel Systems (MCS) preamplifier modules. These modules were designated with inverting or non-inverting outputs so that signals originating in the front and back of the DSSD are produced with the same final polarity. Both high gain (2 V/pC) and low gain (0.1 V/pC) analog outputs were available, with impedance of 50Ω. The low gain signals were sent directly to analog-to-digital converters (ADCs) with no additional shaping. The high-gain signals required additional processing to accurately separate the small ΔE signal from noise and also to define the trigger logic for the experiment. These signals were sent to Pico Systems shaper/discriminator modules in CAMAC, with software adjustable gains and thresholds. The Pico Systems shapers provided separate energy and time signals for each channel, and a fast 16 channel OR output signal for logical signal discrimination, as depicted in Figure 3.9. The analog energy signals were

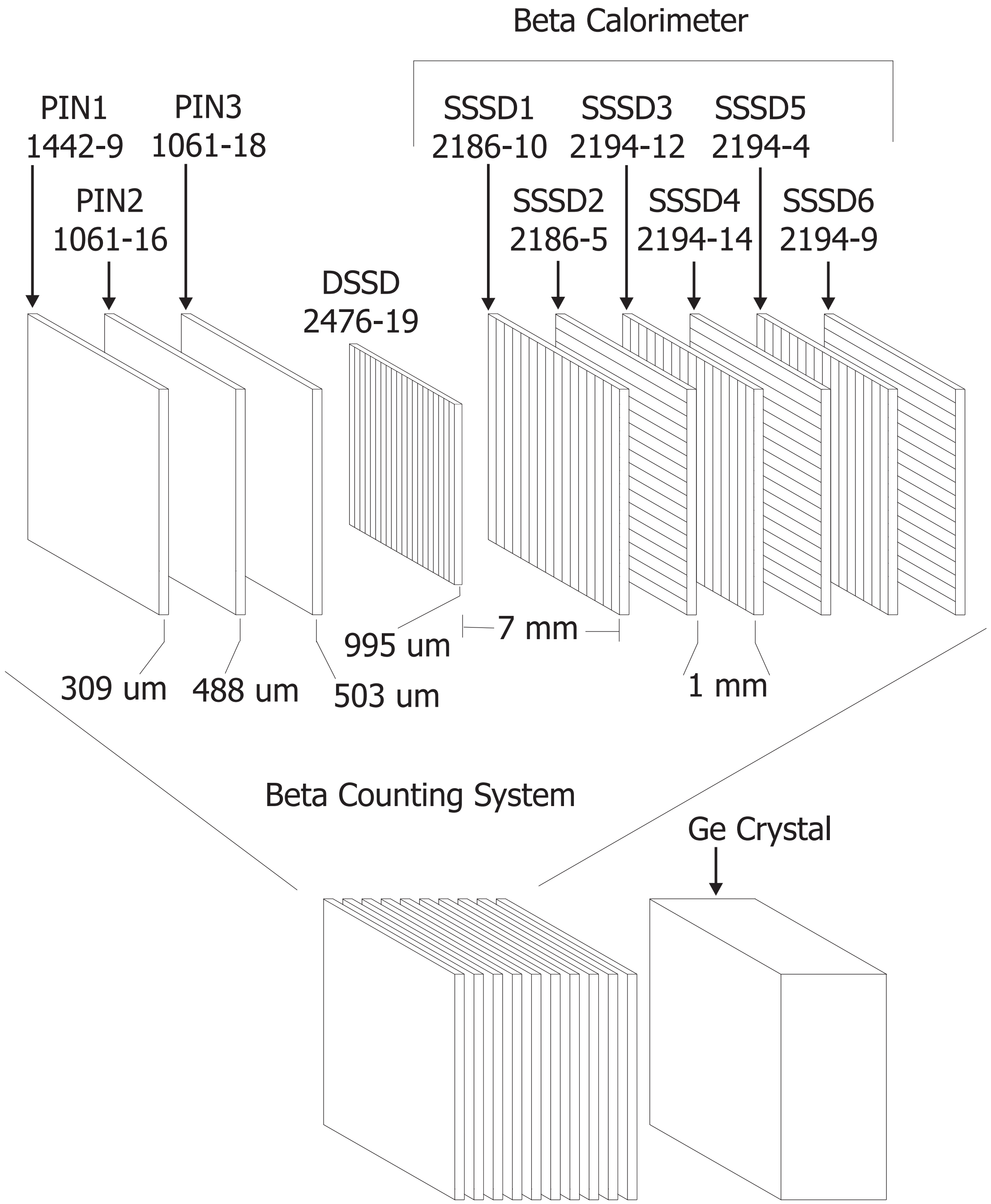

Figure 3.8. Schematic drawing of the detectors comprising the BCS. Drawing is not to scale. The thicknesses of detectors that served as beam degraders are given. Labels assigned to each detector will be used throughout this dissertation. Figure modified from Ref. [41].

further processed by VME ADCs. The time signals were sent to VME scalar modules for rate monitoring, and also to a coincidence register (see Table 3.3). The coincidence register provided a boolean signal to the readout software that determined whether or not the energy signals in a particular ADC were processed. The bit assignment of each ADC and the corresponding detector signals are listed in Table 3.3. Each ADC received 32 energy signals, so ADC1 therefore handled both the 16 high-gain and 16 low-gain energy signals from channels 1-16 of the front DSSD strips. This setup allows strip-specific monitoring of event rates and energies, but the data collection software recorded the data from an entire ADC if any of the 16 channels registered an event.

The SSSD electronic schematic is shown in Figure 3.10. Each SSSD was connected directly to a MCS preamplifier, with the output monitored only from the preamplifier high gain. The fast output from the SSSD Pico Systems shaper/discriminator module was supplied to a coincidence register. The energy signals from two SSSDs were processed by a single VME ADC, as detailed in Table 3.3, so that an energy signal in any of the 16 strips from either SSSD1 or SSSD2 would trigger a readout of all the energy signals monitored by the ADC for SSSD1 and SSSD2. Scaler signals were not monitored for the SSSDs.

The schematic diagram for the PIN detector electronics is shown in Figure 3.11. Each PIN detector signal was connected directly to a Tennelec preamplifier and shaping amplifier. The energy signals from the shaping amplifier were then sent to an ADC for recording. The PIN1 and PIN2 fast output signals were sent through a Tennelec constant fraction discriminator (CFD) before further monitoring. The PIN1 CFD output was sent to the coincidence register with a bit assignment that governed readout from an ADC that processed the energy signal for PINs 1-3. The PIN1 and PIN2 CFD outputs were sent to a scaler module for rate monitoring. A fragment TOF signal was generated for both PIN1 and PIN2 from the difference in time between a

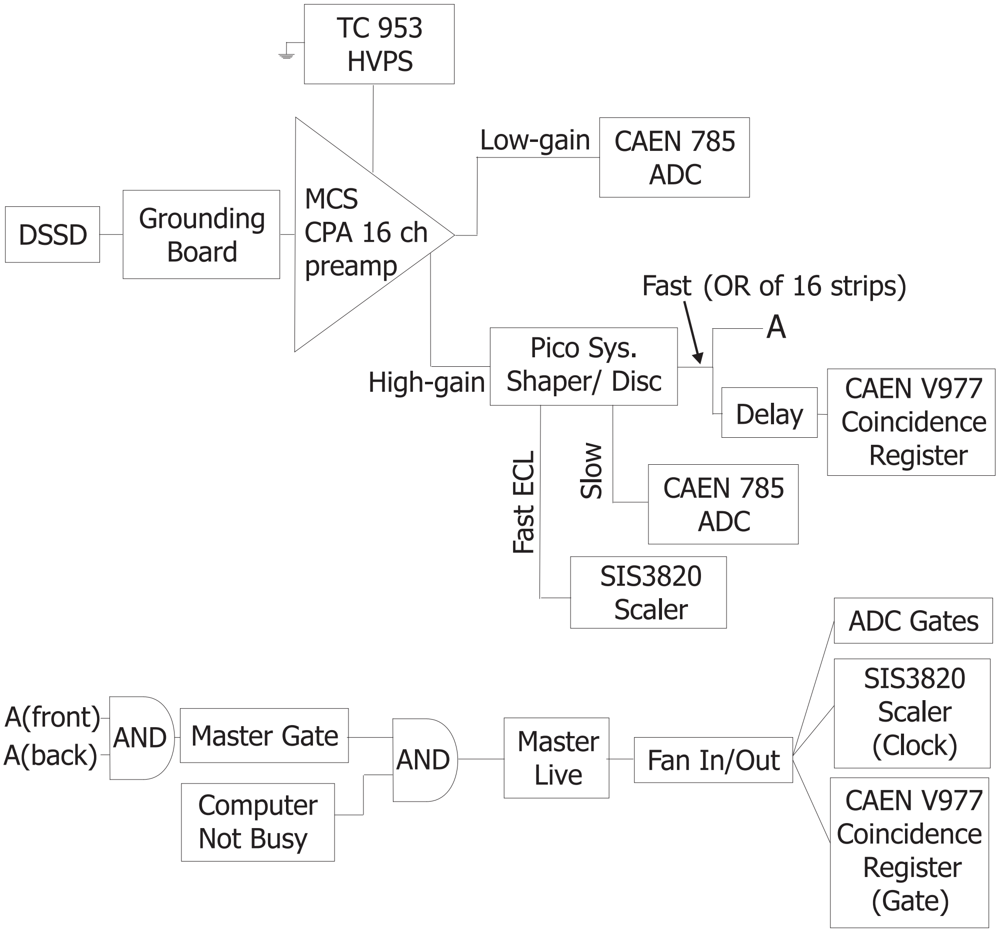

Figure 3.9. DSSD electronics diagram. The DSSD grounding board took the 40 signals from the DSSD and provided individual ground for each signal. These signals were transfered to the MCS preamplifiers by 34-conductor ribbon cable. Figure modified from Ref. [41].

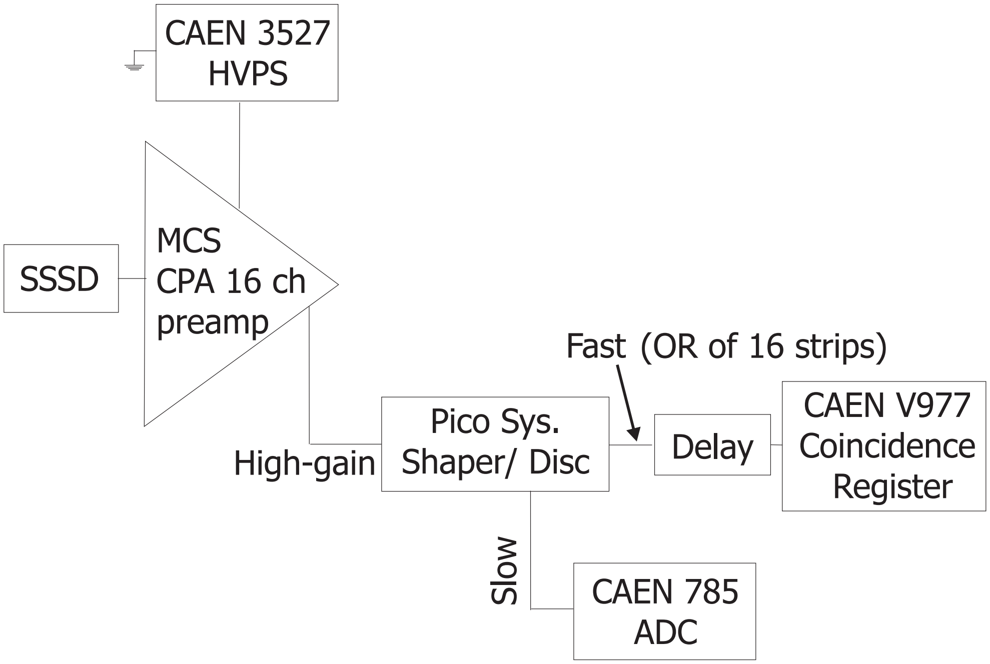

Figure 3.10. SSSD electronics diagram. SSSD signals were transfered to the MCS preamplifiers by a shielded 34-conductor ribbon cable. The ground for each conductor is connected to the MCS preamplifier ground. Figure modified from Ref. [41].

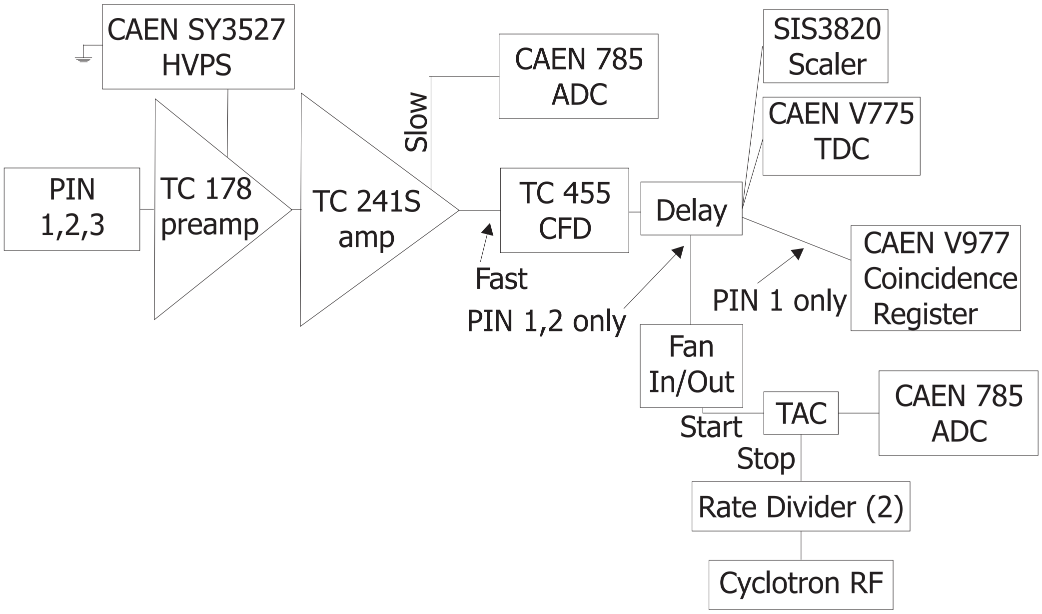

Figure 3.11. PIN detector electronics diagram. Figure modified from Ref. [41]

PIN start signal and a stop signal provided by factor 2 rate-divided K1200 cyclotron radiofrequency (RF).

A coincidence between the DSSD front and back signals was used to trigger the readout of all other detector systems during the experimental production runs. The Pico Systems fast OR signal for the DSSD front groups 1-16, 17-32, and 33-40 were logically OR'ed, with a similar logical OR made for the back channels. The front and back OR signals were then subject to a logical AND to create the master gate signal. This master gate made a logical AND with a computer-not-busy signal to provide the master live signal. Master live "opened" the data acquisition gate for ADC conversion, and processing the coincidence register information. The coincidence register was used to reduce the event size of data buffers by selective ADC readout. The coincidence register bit pattern is listed in Table 3.3.

High voltage was supplied to each BCS Si detector, with the exception of the DSSD, through a CAEN SY3527 High Voltage Power Supply (HVPS). Individual software controls for voltage ramp rate, leakage current, and maximum voltage were

Table 3.3. Channel assignments for CAEN V977 Coincidence Register

CAEN V977 Coincidence Register		
BIT	Detector	ADC
0	DSSD F01-16	1
1	DSSD F17-32	2
2	DSSD F33-40	3
3	DSSD B01-16	4
4	DSSD B17-32	5
5	DSSD B33-40	6
6	SSSD1	7
7	SSSD2	7
8	SSSD3	8
9	SSSD4	8
10	SSSD5	9
11	SSSD6	9
12	PIN 1	10
13	Ge	10
14	(empty)	-
15	(empty)	-

available for each detector connected to the CAEN HVPS. The resolution in leakage current for the CAEN HVPS was 200 nA. A Tennelec TC 953 HVPS, with leakage current resolution of 1 nA, was used for the DSSD.

Each trigger event was tagged with an absolute time stamp created by a 32 bit SIS3820 scaler/counter module operating at 50 MHz as a system clock. The 32-bit word was stored for each event as two separate 16-bit words, clock.fast and clock.slow, with the first 16 bits of the system clock signal assigned to clock.fast and the second 16 bits of the system clock signal assigned to clock.slow. The nanosecond time resolution from the scaler module was not required to achieve the desired precision of order 0.1 s sought for in this work. Therefore, the clock variables were mapped to a 24-bit variable according to the equation:

$$clock24bit = (clock.fast + 65536 * clock.slow)/2^8$$

resulting in a time resolution for all events of 5.12 μs, which more than satisfied the precision requirement.

BCS Calibration

Each SSSD and the DSSD was individually calibrated using a ^{90}Sr β source to adjust the signal hardware thresholds. The hardware (CFD) thresholds for each strip were also fine tuned during the experiment to suppress noise fluctuations. After the CFD thresholds were set, spectra were collected from a ^{228}Th α source for gain matching. Representative α spectra from the front and back strip 21 of the DSSD are presented in Figure 3.12. The ^{90}Sr spectra were collected on the gain-matched detectors, to establish the software low energy thresholds as indicated in Figure 3.13.

The program LISE++ [42] was used to calculate the energy losses of the isotopes: ^{73}As, ^{74}Se, ^{76}Br, ^{79}Sr, ^{80}Y, ^{81}Zr, ^{82}Zr, ^{83}Nb, and ^{84}Mo in the PIN detectors 1-3. The observed centroid positions in PINs 1-3 were then assigned to the calculated energies to provide the calibration. The relative Total Kinetic Energy (TKE*) of

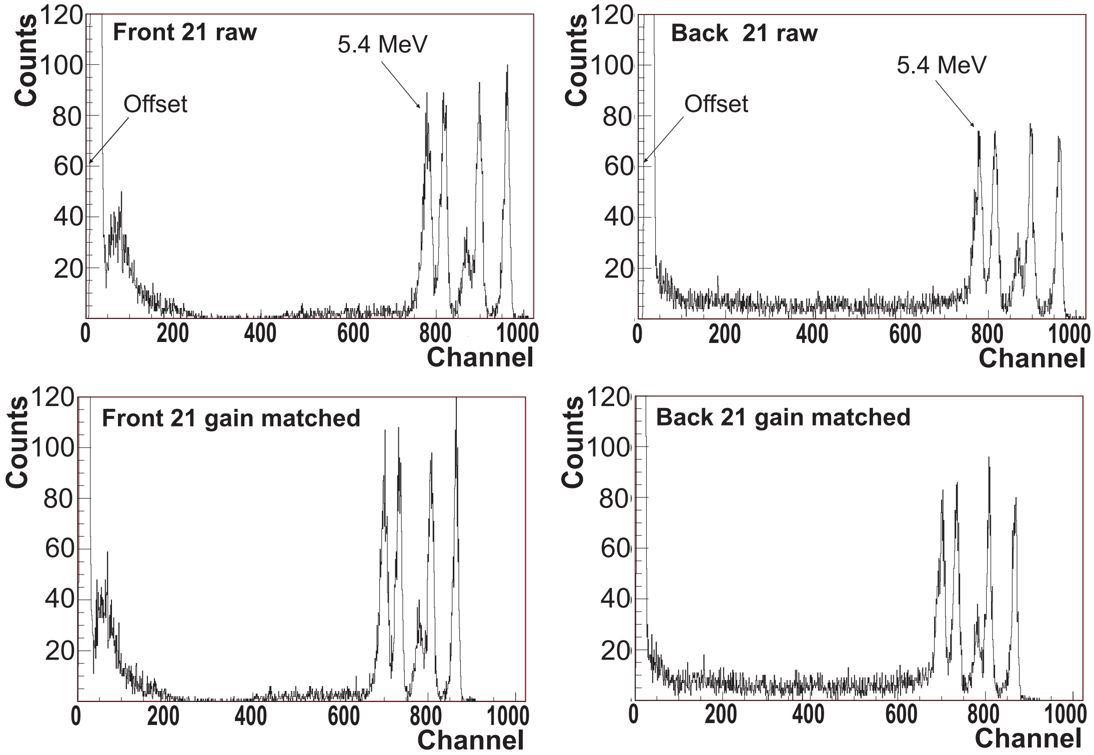

Figure 3.12. α decay spectra of ^{228}Th for front and back strip #21 of the DSSD. Upper spectra show the raw energy spectra, with arrows indicating the location of the 5.4 MeV α peak and the size of the spectral offset used to generate the gain-matched spectra.

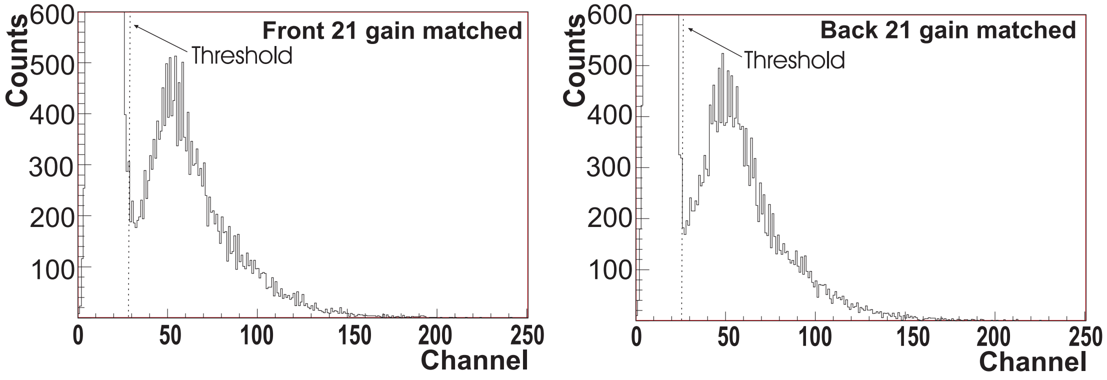

Figure 3.13. Gain-matched ^{90}Sr β-decay spectra for the front and back strip #21 of the DSSD. Dashed lines indicate the location of the low energy software threshold.

fragments was determined by adding the calibrated energy loss for each PIN detector (ΔE^*) and the (source calibrated) DSSD front-side energy loss (ΔE), so that the relative TKE* is given by

$$TKE^* = \Delta E^*_{PIN1} + \Delta E^*_{PIN2} + \Delta E^*_{PIN3} + \Delta E_{DSSD-front} \tag{3.3}$$

3.2.2 Segmented Germanium Array

The experimental endstation incorporated 16 detectors from SeGA [4]. Each detector is composed of a cylindrically-symmetric n-type coaxial germanium crystal with a 7 cm diameter and 8 cm length. The outer contacts of the crystals are electrically divided into eight 10 mm disks along the length of the Ge cylinder. Each disk is subdivided into four quarters for a total of 32 segments. This high segmentation increases the position resolution of γ rays in the detectors, and is useful for Doppler correction during in-beam studies [4]. The Ge detector segmentation was not utilized in the present work because β-decay studies are performed on stopped beams so only total energy information from the central contact of each crystal was necessary. The 16 detectors were mounted on a frame designed to closely pack the cylindrical Ge crystals in two concentric rings of eight detectors around the BCS chamber, as shown in Figure 3.14. Each SeGA detector was mounted with its cylindrical axis parallel to the beam axis. The DSSD was located in the plane that separated the upstream and downstream Ge detector rings, thereby maximizing the overall detection efficiency of γ rays emitted from nuclei implanted in the DSSD. A schematic electronics diagram for each Ge detector is shown in Figure 3.15. Data were collected for all Ge ADCs for events that produced a master live trigger.

Ge Calibration

The Ge detectors were energy-calibrated three times for this experiment. Two sources, ^{56}Co and a Standard Reference Material (SRM) containing ^{125}Sb, ^{152}Eu, ^{154}Eu,

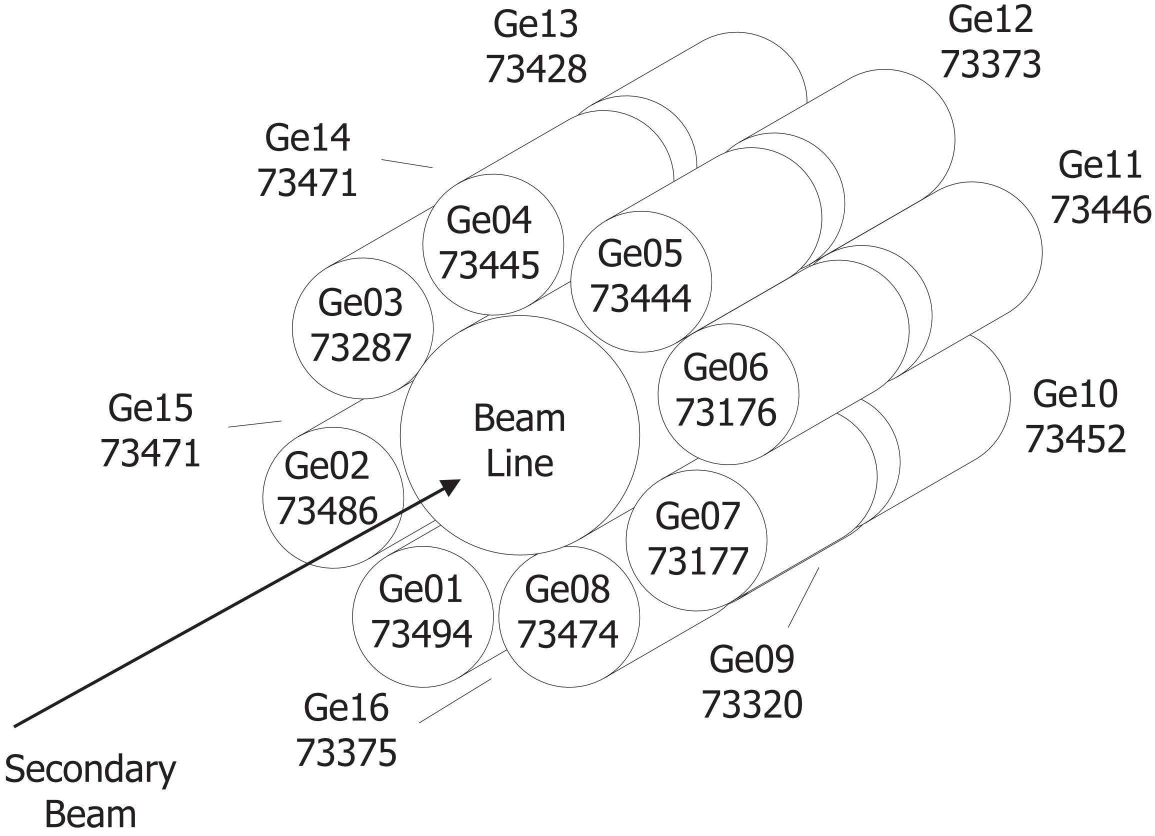

Figure 3.14. Geometric arrangement of the 16 detectors from SeGA around the BCS. The BCS was centered to the two rings of eight detectors such that one ring lay upstream and the other downstream of the DSSD. Serial numbers indicate specific detectors that were used in each position. Figure modified from [41].

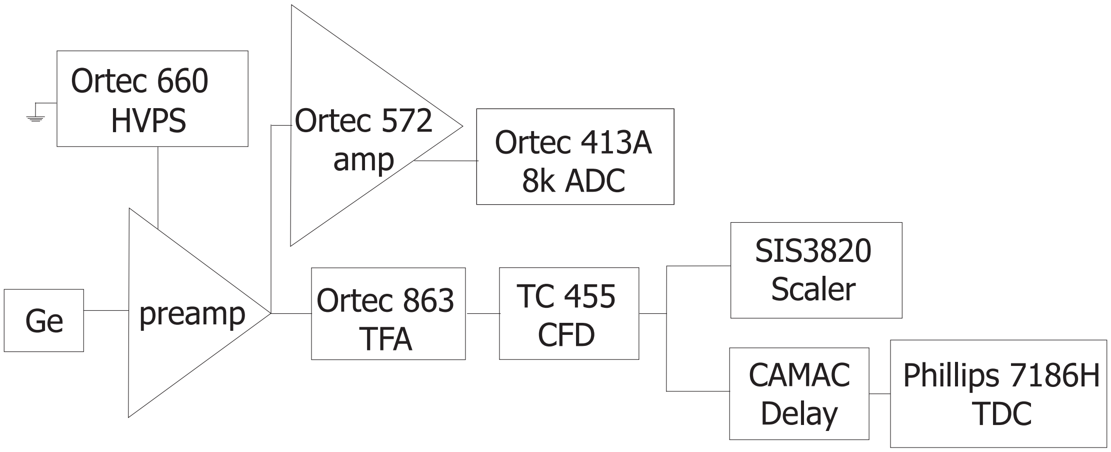

Figure 3.15. Schematic diagram of the Ge detector electronic setup. Figure modified from Ref. [41].

and ^{155}Eu, were used for calibrations [43]. The first calibration was done prior to the start of the experiment and was used for online analysis and was also applied to most of the production runs during offline analysis. The K1200 stripping foils were fully consumed three days prior to the scheduled end of the experiment, which forced a temporary interruption of the data collection while the K1200 vacuum was vented and a new set of stripper foils was installed. The replacement of stripper foils could have led to a premature end to the experiment. The second Ge calibration was performed at this point in case data collection was not resumed. An additional 35 hours of data collection were after the new set of stripper foils were installed and the cyclotron became operational in under 24 hours. The third Ge energy calibration was performed at the scheduled end of the experiment, and supplied the calibration for the majority of the data collected after the mid-experiment stripper foil installation. The second Ge calibration was used as a check on the first and third calibrations only, and was not applied to the data for γ-energy calibration.

Each calibration used the well known γ-ray energies from the ^{56}Co and SRM sources using the energies indicated in Table 3.4. The sources were placed on the beamline, one directly before and the other directly after the position of the germanium detectors during energy calibration runs, with the source locations being exchanged halfway through the each calibration run. Data readout was triggered by an OR of all 16 Ge detectors. The calibration spectra were evaluated using the Oak Ridge Display Analysis and Manipulation Module (DAMM) [48]. A third-order polynomial equation describing the least-squares fit of the peak channel positions observed in the spectra as a function of the known γ-ray transition energy was used to generate the calibrated spectra for each detector.

Residuals for the first calibration are shown for each detector in Figure 3.16, and for the sum of all 16 detectors in 3.17. The third calibration residuals follow in Figures 3.18 and 3.19 for the individual and the summed spectra, respectively. The residuals were determined by measuring the difference between calibrated and actual energies. The accuracy of the energy calibration for each detector was improved by minimizing the energy deviation by applying a constant offset. The systematic error used in this work was the standard deviation (1σ) of the offset-improved residual values (0.156 keV). The total error for γ-ray energies reported in this work was determined by the error in the centroid position resulting from the Gaussian peak fit given by DAMM, summed in quadrature with the systematic error. In addition, small (1% or less) adjustments were applied throughout the dataset to compensate for electronic gain shifts. Such shifts were observed by monitoring the locations of the 511 keV positron annihilation peak and the 1173 and 1333 keV background peaks from ^{60}Co, which was stored in a wall safe several meters from the experimental endstation. Four small adjustments were required for the detector located at position 2, while positions 12 and 16 required one gain adjustment each in order to offset the observed gain shifts.

Absolute peak detection efficiencies were determined for each Ge detector with the SRM γ-ray source. The transitions used in the calibrations are indicated in Table 3.4. The SRM source was placed at the DSSD position with the beam line

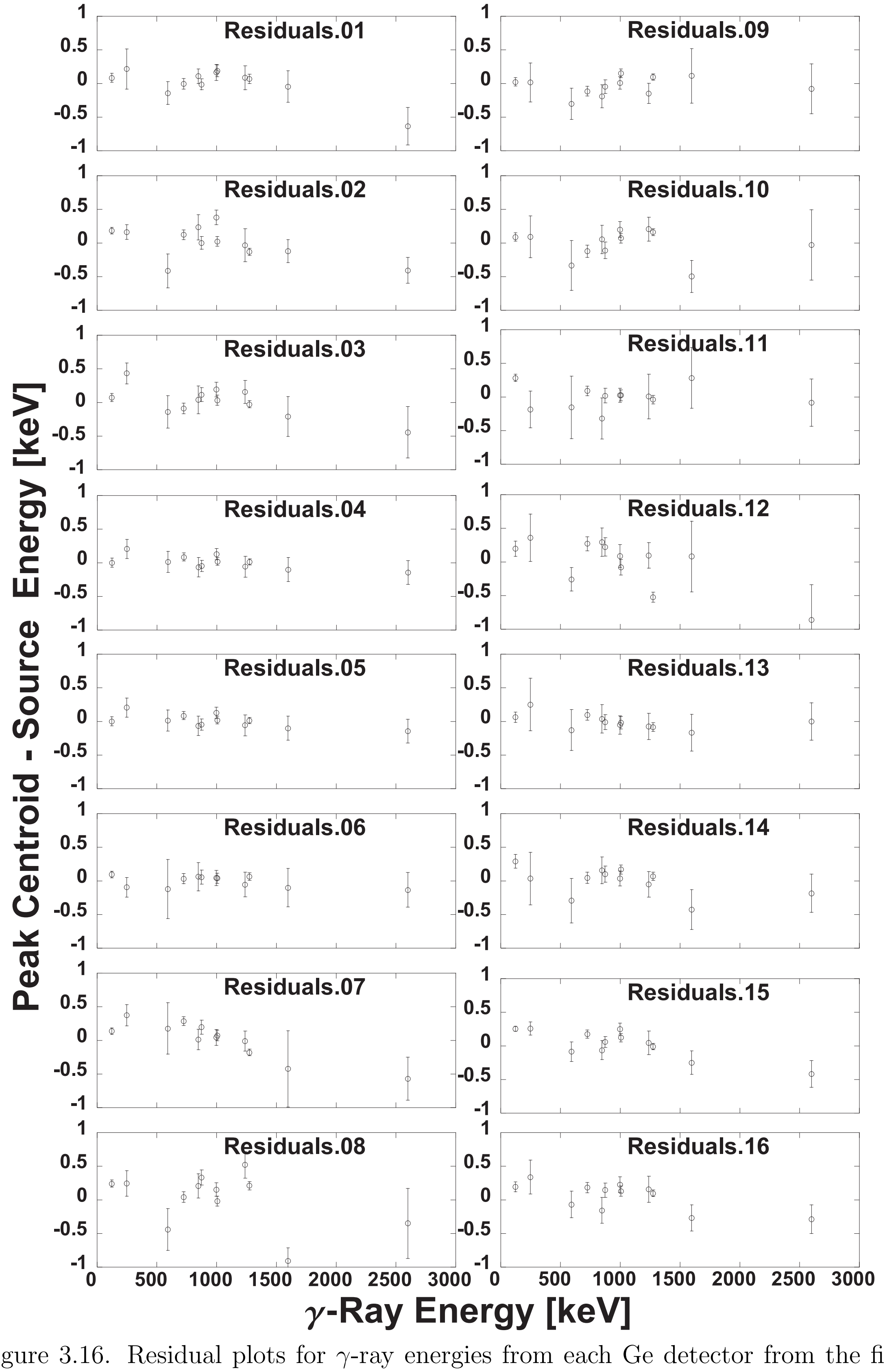

Figure 3.16. Residual plots for γ-ray energies from each Ge detector from the first experimental calibration. Labels correspond to position number shown in Figure 3.14

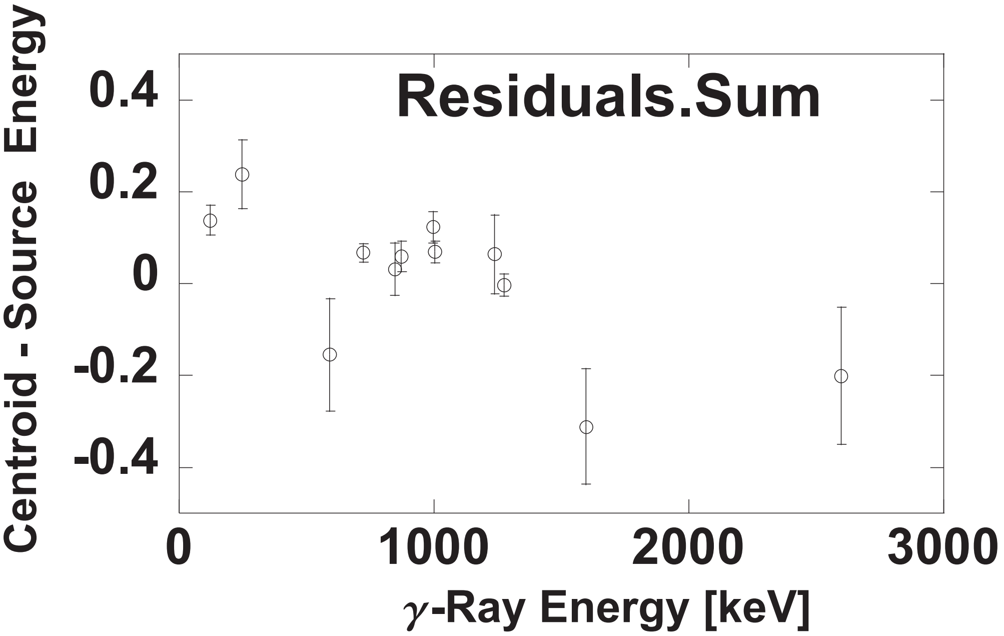

Figure 3.17. Residual plot for γ-ray energies collected during the first calibration from the γ-ray spectrum taken as a sum of all 16 SeGA detectors.

at atmospheric pressure. A γ-ray spectrum was collected simultaneously using a PC-based multichannel analyzer (PCMCA) detector and the NSCL data acquisition system. The PCMCA collection used a preset live collection time of 3600 s so that the true collection time was identical for each detector, while the NSCL data acquisition relies on post-run corrections to the collection time using the recorded live time. The relative efficiency at high energies was deduced with a ^{56}Co source placed again at the DSSD position for a 7200 s collection time. This relative measurement was made for all 16 Ge detectors simultaneously with the NSCL data acquisition system only. The observed emission rate was normalized to the known activity of each isotope in the calibration sources. A log-log plot of efficiency versus energy is shown in Figure 3.20. The energy efficiency measurements were fit with a fifth-order polynomial in the energy range of 43-3273 keV. The calculated peak efficiency of the entire array was determined to be 6.6% for a 1-MeV γ ray.

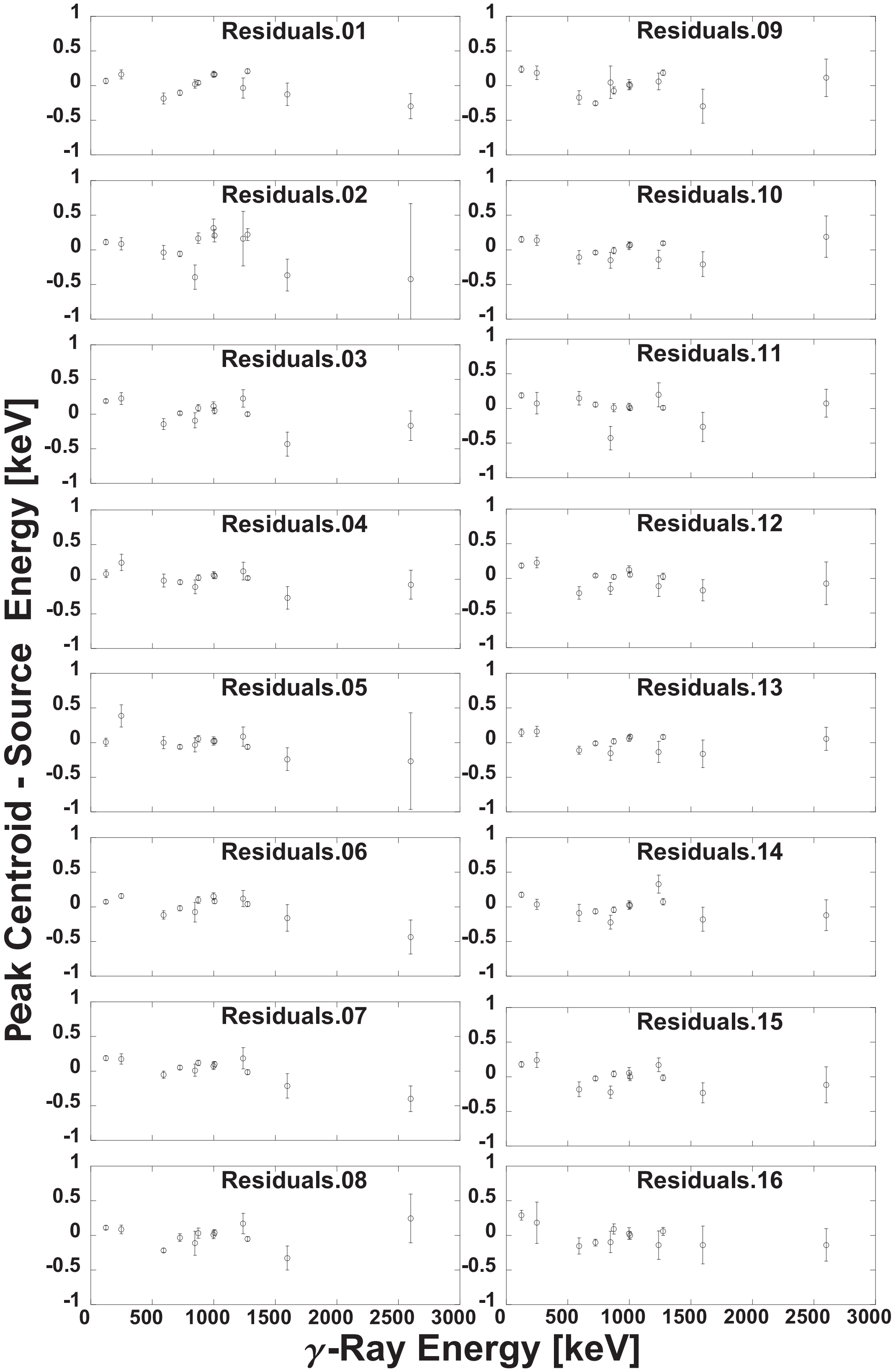

Figure 3.18. Residual plots for γ-ray energies from each Ge detector from the third experimental calibration. Labels correspond to position number shown in Figure 3.14

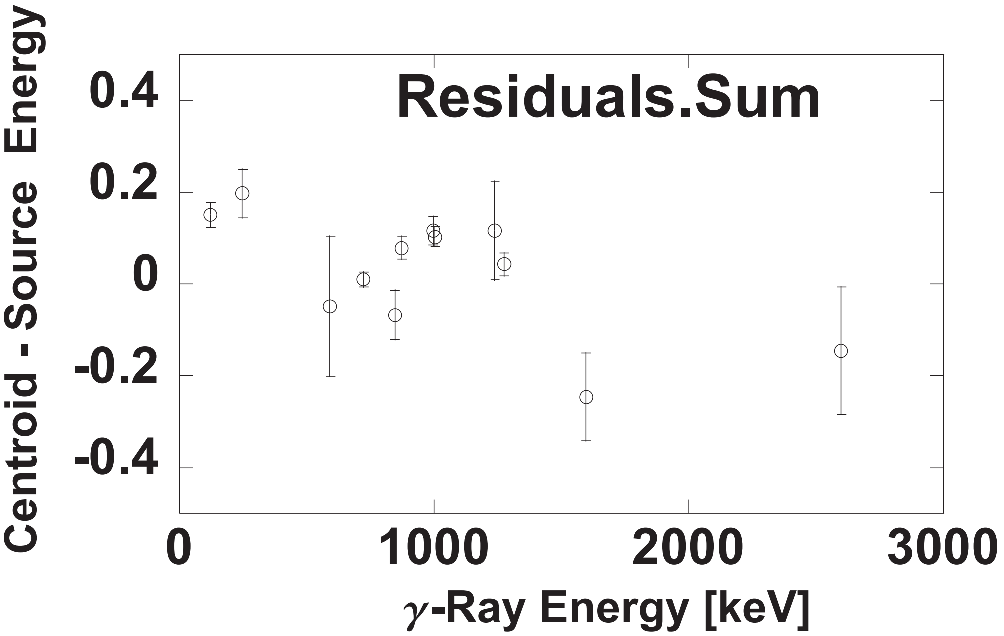

Figure 3.19. Residual plot for γ-ray energies collected during the third calibration from the γ-ray spectrum taken as a sum of the gain-matched energy signals from all 16 SeGA detectors.

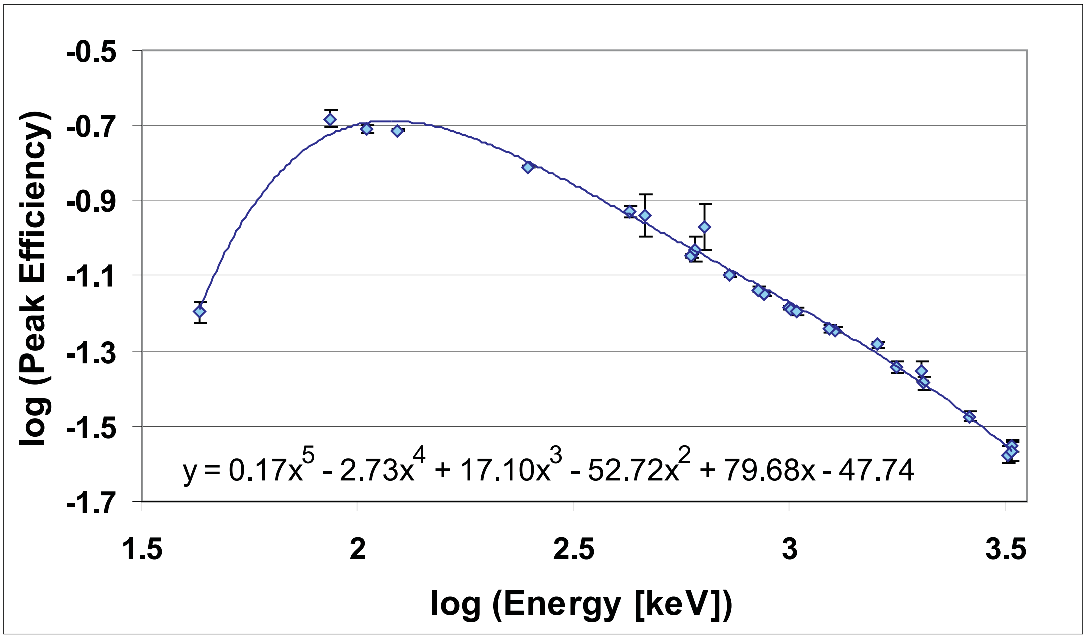

Figure 3.20. The log(efficiency) versus log(energy) showing the absolute efficiency of the 16 detectors used from SeGA during this study. Measured efficiencies for energies up to to 3273 keV were fit with the fifth order polynomial shown in the figure.

Table 3.4. γ-ray energies used to calibrate the Ge detectors in this work [43, 44, 45, 46, 47]. The use of a particular energy peak in either the energy or efficiency calibration is indicated by a $\surd$ in the appropriate column.

	.	Calibration	
Source	Energy (keV)	Energy	Efficiency
SRM-^{153}Gd	42.8		$\surd$
SRM-^{155}Eu	86.547(1)		$\surd$
SRM-^{155}Eu	105.308(1)		$\surd$
SRM-^{154}Eu	123.071(1)	$\surd$	$\surd$
SRM-^{154}Eu	247.929(1)	$\surd$	$\surd$
SRM-^{125}Sb	427.874(4)		$\surd$
SRM-^{125}Sb	463.365(4)		$\surd$
SRM-^{154}Eu	591.755(3)	$\surd$	$\surd$
SRM-^{125}Sb	600.597(2)		$\surd$
SRM-^{125}Sb	635.950(3)		$\surd$
SRM-^{154}Eu	723.301(3)	$\surd$	$\surd$
^{56}Co	846.7638(19)	$\surd$	$\surd$
SRM-^{154}Eu	873.180(7)	$\surd$	$\surd$
SRM-^{154}Eu	996.262(5)	$\surd$	$\surd$
SRM-^{154}Eu	1004.725(6)	$\surd$	$\surd$
^{56}Co	1037.8333(24)		$\surd$
^{56}Co	1238.2736(22)	$\surd$	$\surd$
SRM-^{154}Eu	1274.429(7)	$\surd$	$\surd$
SRM-^{154}Eu	1596.487(17)	$\surd$	$\surd$
^{56}Co	1771.327(3)	$\surd$	$\surd$
^{56}Co	2015.176(5)		$\surd$
^{56}Co	2034.752(5)		$\surd$
^{56}Co	2598.438(4)	$\surd$	$\surd$
^{56}Co	3201.930(11)		$\surd$
^{56}Co	3253.402(5)		$\surd$
^{56}Co	3272.978(6)		$\surd$

CHAPTER 4

Particle Identification

4.1 μs Isomers

The fragments arriving at the BCS were distinguished according to their location on a plot of ΔE^* vs. TOF. The ΔE^* measurement was deduced from PIN1. TOF information was determined from the time difference between a start signal provided by PIN1 and a stop signal given by the K1200 cyclotron RF downscaled by a factor 2. The PID was confirmed by the unambiguous identification of ^{73}As through its characteristic isomeric γ-ray decay. ^{73}As has a known isomeric state at 427.76 keV [49], which decays via a 2-γ cascade with energies 67.03 and 360.80 keV. The ^{73}As isomeric state has a half-life 5.7(2) μs, which is long enough to survive the $\sim$600 ns flight time from the production target to the experimental endstation. Fragments that were coincident with the observed 360.80 keV γ ray, shown in the spectrum in Figure 4.1, were therefore attributed to ^{73}As. The opposite selection of γ rays in coincidence with the fragments in the PID spectrum in Figure 4.1 is shown in Figure 4.2, where both transitions in the cascade from the 427.76 keV isomeric state are clearly present. The determination of the locations of specific isotopes was then based on their position on the ΔE^* vs. TOF plot relative to ^{73}As.

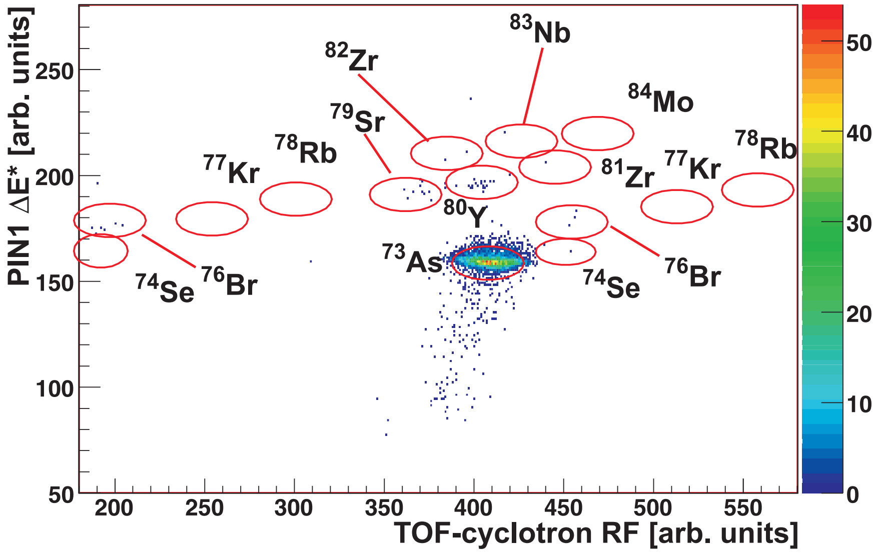

Figure 4.1. The distribution of DSSD implantation events, given as PIN1 ΔE* vs. TOF, observed in coincidence with a prompt 361 keV γ ray.

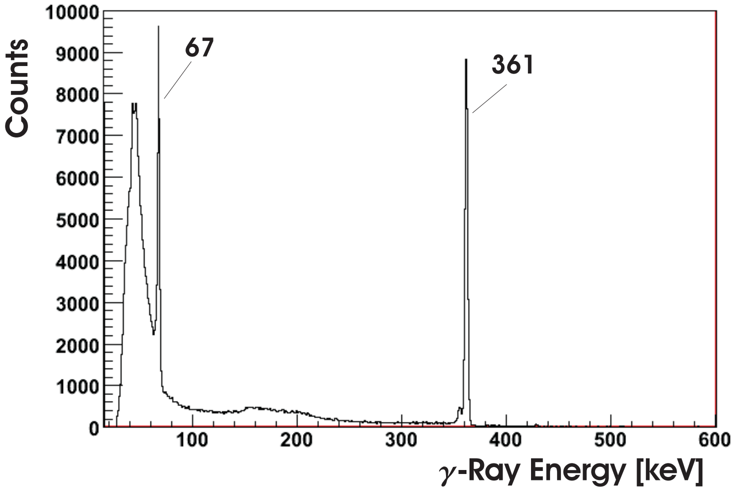

Figure 4.2. γ-ray spectrum of events in prompt coincidence with ^{73}As fragment implantations into the DSSD. The known 67 and 361 keV transitions which depopulate the 428 keV ^{73}As isomeric state, via cascade, are clearly present in the data.

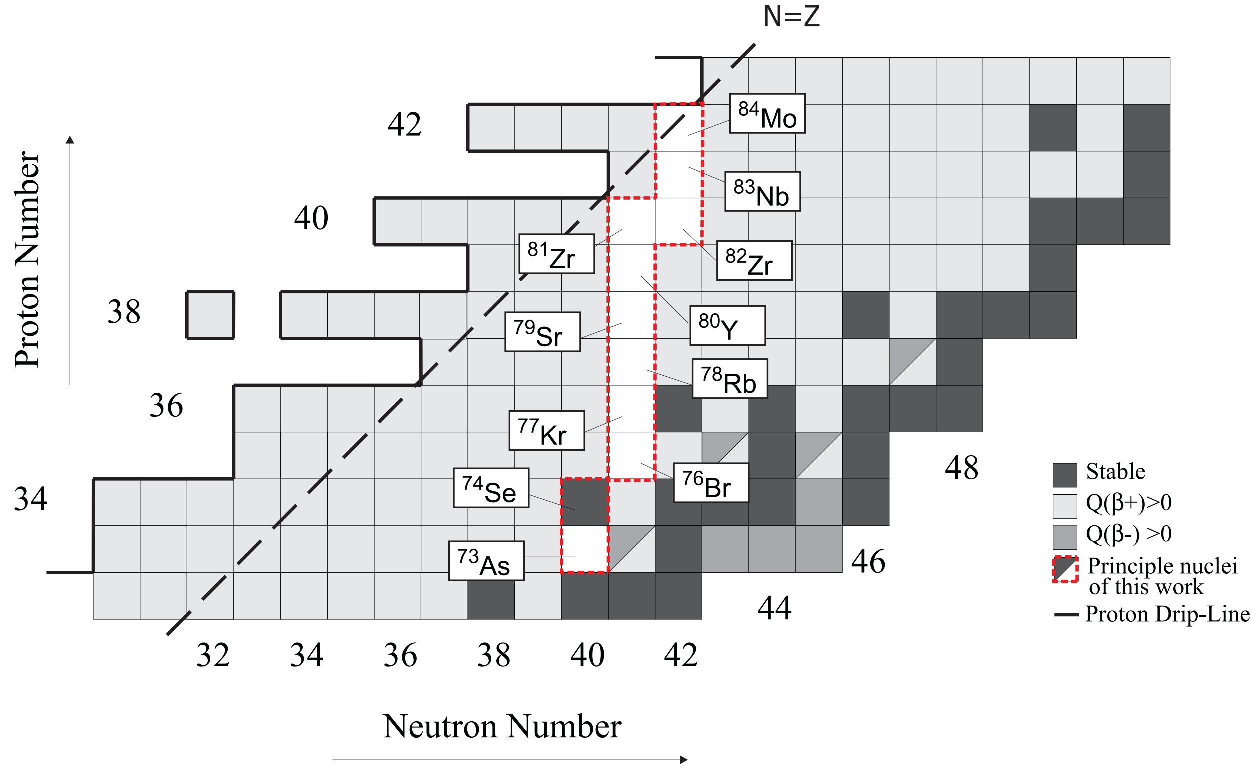

Figure 4.3. Section of the chart of the nuclides in neutron-deficient region near A $\approx 65 - 90$. All highlighted nuclei are β^+emitters except the stable ^{74}Se. The strong contaminants ^{78}Rb and ^{77}Kr were largely removed using the RFFS, with smaller fractions of ^{79}Sr and ^{76}Br also being removed.

The principle nuclei sent to the experimental endstation were: ^{73}As, ^{74}Se, ^{76}Br, ^{77}Kr, ^{78}Rb, ^{79}Sr, ^{80}Y, ^{81}Zr, ^{82}Zr, ^{83}Nb, and ^{84}Mo. A partial chart of the nuclides provided in Figure 4.3 highlights the location of these principle nuclei relative to stability. The bulk of the beam contaminants from the initial fragmentation process were removed through a combined application of the NSCL A1900 [39] and RFFS [5]. The RFFS significantly reduced contamination in the beam due to ^{77}Kr and ^{78}Rb, as was demonstrated in Sec. 3.1.3.

A PID plot obtained with the RFFS on, given as PIN1 ΔE* vs. TOF, is shown in Figure 4.4. Individual isotopes are clustered together in “blobs” with a TOF width related to the 1% distribution in momentum passed through the A1900.

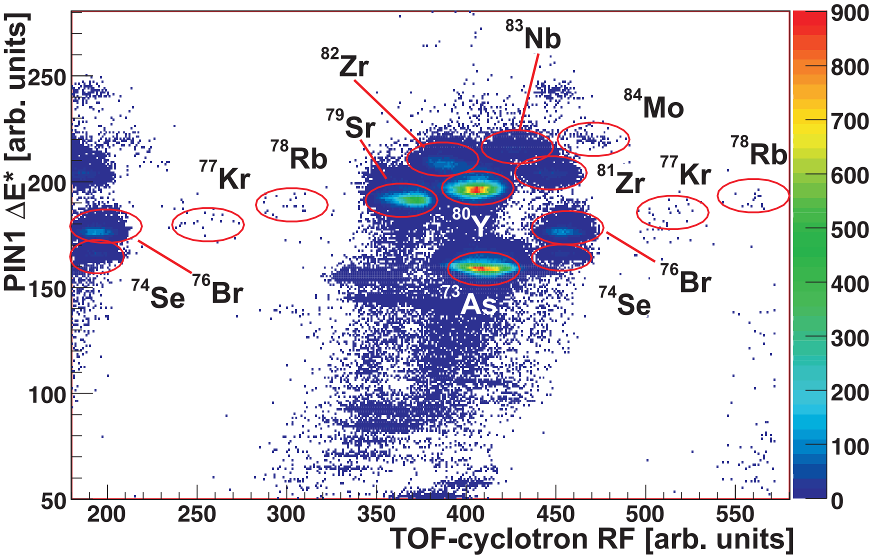

Figure 4.4. PID plot, given as PIN1 ΔE* vs. TOF, with the RFFS on. This plot contains all of the data collected for determining the ^{84}Mo half-life. In contrast to Figure 3.7, there are 1054202 ^{80}Y implantation events in this plot. The repeating pattern, separated by ∼250 ns, in TOF arises due to the downscale of the cyclotron RF signal by a factor 2.

4.2 Charge-state Identification

The ^{124}Xe primary beam was accelerated in the K1200 cyclotron in the 48^+ charge state. Primary beam interactions in the target and fragment interactions in the A1900 intermediate-image wedge can result in either the pickup or loss of orbital electrons. The presence of one (hydrogen-like), two (helium-like), or more (lithium-like and so forth) orbital electrons attached to beam fragments allows some of these fragments to have a p/q [see Eq. (3.1)] within the A1900 acceptance of ^{84}Mo^{42+} and contribute to beam contamination.

Beam contamination from unwanted fragment charge states can be identified by the total energy of the ions by summing the ΔE^* signals in PIN detectors 1-3 and energy signals in the DSSD. Fragments with one electron, in relation to fully stripped ions with similar p/q, experience an appreciably higher energy loss [see Equation (3.2)] in the PIN detectors upstream of the DSSD. The fragments with orbital electrons will have a lower momentum than the fully stripped ions with the same p/q. Consequently, the energy loss increased due to both a higher amount of energy being deposited per unit depth and a relatively lower momentum.

The cumulative energy loss of fragments through the Si detectors in the BCS eventually brings each fragment to rest. The thickness of Si that a fragment passes through before coming to rest is the implantation depth of that fragment in the BCS. Recall that the PIN detector thicknesses were selected to ensure that fully-stripped ions are stopped in the most upstream 1/3 of the DSSD. The increased energy loss of fragments that contained orbital electrons prior to reaching the BCS (charge-state contaminants) resulted in many of them not reaching the DSSD. The majority of the charge-state contaminants deposited the bulk of their energy in either PIN2 or PIN3, though some of the more energetic one electron charge-state contaminants that reached the DSSD experienced an energy loss similar to some fully-stripped ions in the DSSD. Even the most energetic fragments with two or more orbital electrons

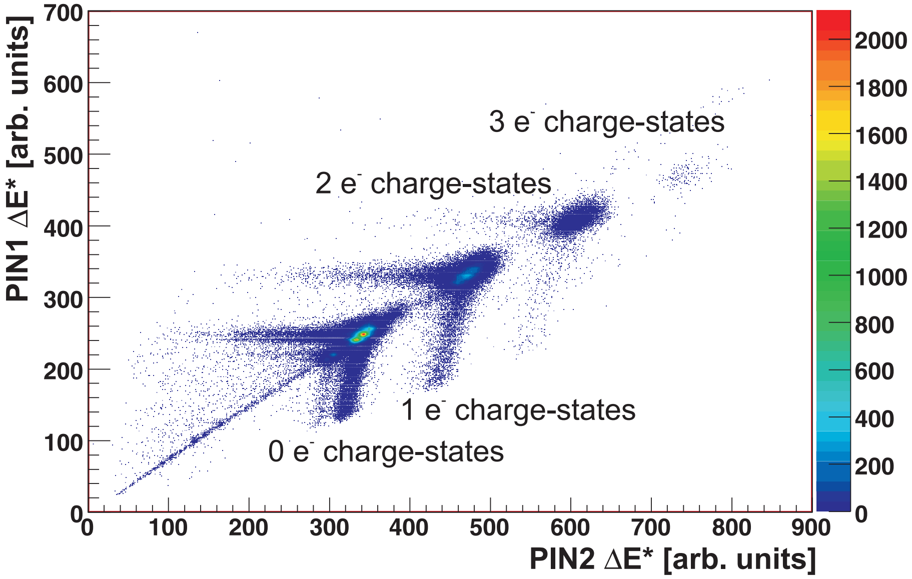

Figure 4.5. Distribution of PIN1 ΔE* vs. PIN2 ΔE* signals obtained with the RFFS off. Groupings are labeled according to the number of orbital electrons associated with the ions.

deposited only trace amounts of energy in the DSSD. Fragments that did not reach the DSSD could not be correlated to their subsequent β decays.

The distributions of PIN1 ΔE* vs. PIN2 ΔE* and PIN2 ΔE* vs. PIN3 ΔE* for runs with the RFFS turned off are shown in Figures 4.5 and 4.6. Separation between charge-state groups was observed along the diagonal of the PIN1 ΔE* vs. PIN2 ΔE* plot. This separation between different charge-states along a diagonal was not seen with PIN3 (see Figure 4.6), as a result of charge-state-contaminant fragments coming to rest in PIN3.

Events that deposited more than 3 GeV of energy in the DSSD led to an overflow of the electronic channel, and were not resolved in TKE*. The front side of the DSSD was used for energy information due to the slightly better signal-to-noise ratio it provided relative to the back side of the DSSD. The TKE* resolution remained poorer than that observed in TOF due to the fragments being scattered through

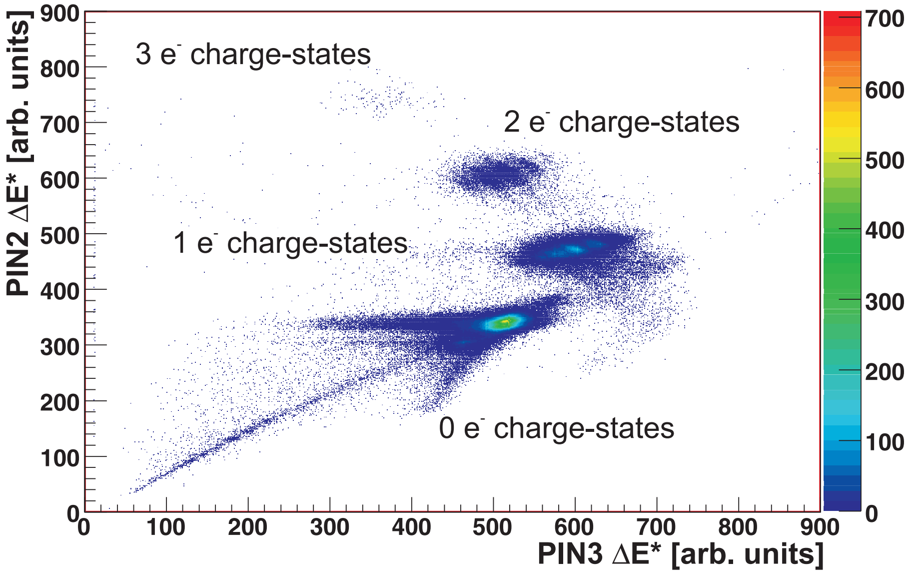

Figure 4.6. Same as Figure 4.5, but for energy loss signals in PIN2 and PIN3 of the BCS.

interactions in the BCS Si detectors. In addition, the TKE* for all charge-states was similar enough that it could not be used as a principle means of isolating fully stripped ions. Figure 4.7 is a plot of PIN1 ΔE* vs. TKE* with the RFFS off, in which the similarity of the TKE* between the different charge-state species can be seen. ^{84}Mo was the heaviest fragment and has the highest number of protons of all the isotopes sent to the BCS; consequently it experienced the highest energy loss in each PIN and the DSSD relative to other fully-stripped fragments. A fraction of the smallest PIN1 and PIN2 energy loss signals for charge-state contaminants with 1 orbital electron "bled" into the highest PIN1 and PIN2 energy loss signals from fully-stripped fragments, including ^{84}Mo. This overlap of the 0 and 1 electron charge state PIN1 ΔE* signals prevented their isolation based on either PIN1 ΔE* or TKE*. However, because fully stripped ions deposited the bulk of their energy in the DSSD they could be easily distinguished from charge-state contaminants that did not reach or only deposited small amounts of energy in the DSSD. In Figure 4.8 is shown a

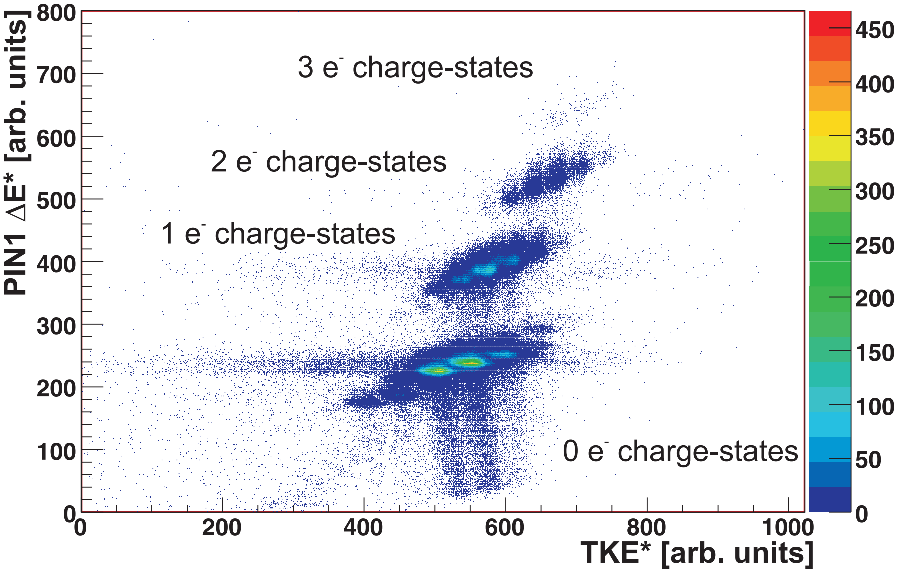

Figure 4.7. Distribution of PIN1 ΔE* vs. TKE* signals obtained with the RFFS off

plot of the PIN1 ΔE* vs. DSSD ΔE, where the “bleed” of 1 electron charge-state contaminants into fully stripped fragments was not as prevalent as in the PIN1 ΔE* vs. TKE* plot shown in Figure 4.7. Fully-stripped ions were isolated by a gated selection of the 0 electron charge states shown in Figure 4.8. A cleaned PIN1 ΔE* vs. TKE* spectrum generated from these 0 electron events is shown in Figure 4.9.

Identification of the implanted ions collected during the runs with the RFFS off provided the basis to identify implantations observed with the RFFS on. Although the energy losses and TOF of the ions should be the same except for the relative yields, the RFFS cut of the yield of ^{77}Kr and ^{78}Rb fragments prevented the stepwise identification of fragments along the line of isotopes described by the relation of $N = Z + 6$. However, the location of fragments observed in the spectrum shown in Figure 3.7A did not change when the RFFS was turned on. Consequently, a similar approach to that described above was employed to isolate fully-stripped ions produced with the RFFS on, starting with the locations of specific fragments as shown in Figure 4.4. The distribution of the values of PIN1 ΔE* vs. TKE*, subjected to the similar

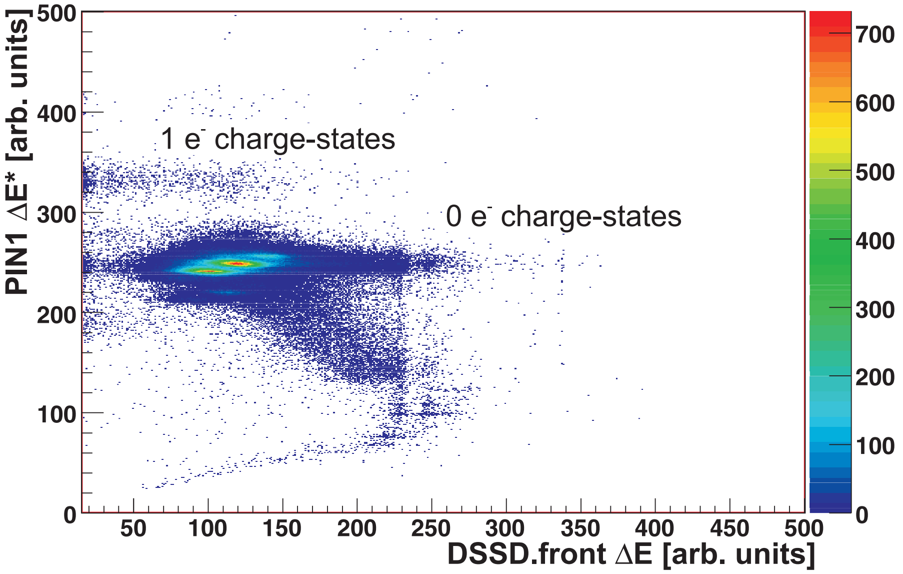

Figure 4.8. Distribution of PIN1 ΔE* vs. DSSD.front ΔE signals obtained with the RFFS off.

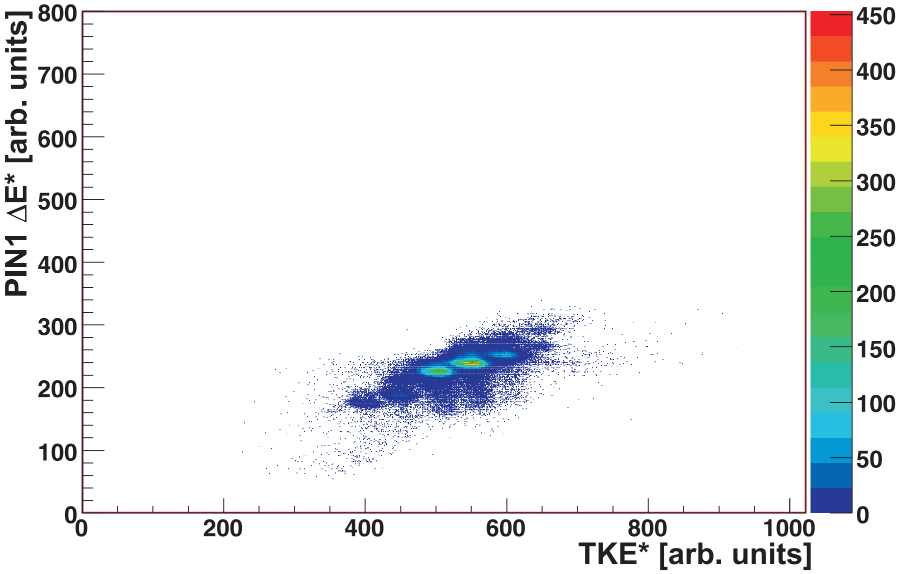

Figure 4.9. Distribution of PIN1 ΔE* vs. TKE* signals obtained with the RFFS off for 0 electron events isolated from the spectrum in Figure 4.8.

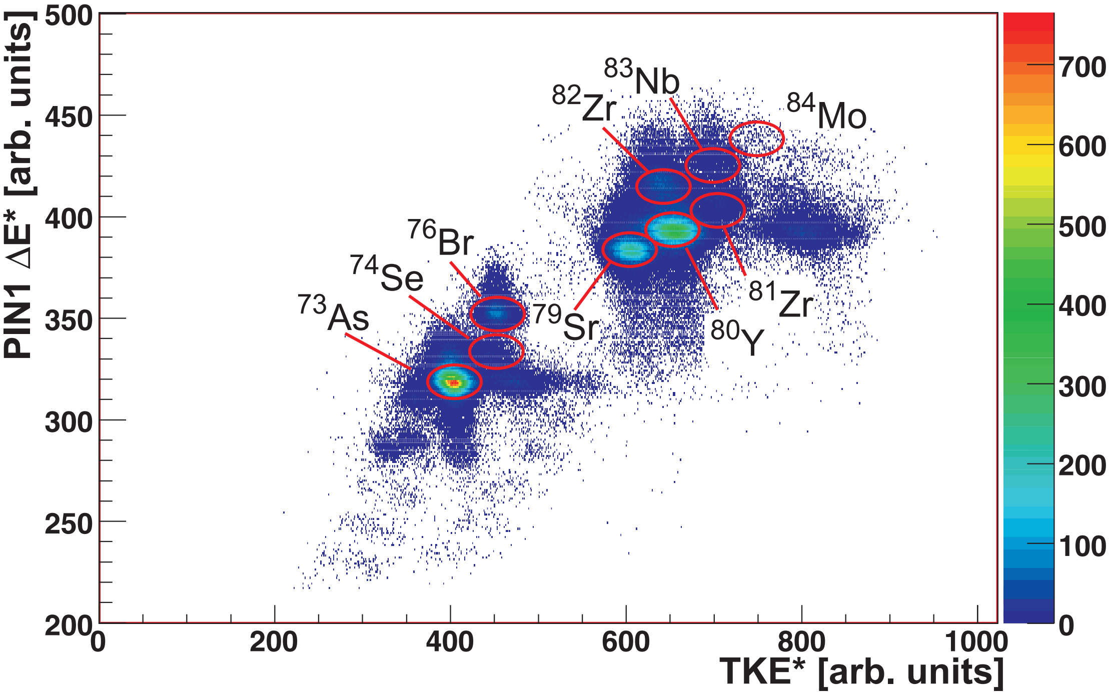

Figure 4.10. Similar to Figure 4.9, except for ^{84}Mo production runs with the RFFS on, with an expanded vertical scale.

filtering as the spectrum in Figure 4.9, is shown in Figure 4.10 for the ^{84}Mo production runs with the RFFS on. The cleaned PIN1 ΔE* vs. TKE* spectrum resolved charge state contaminants that were not seen in either PIN1 ΔE* vs. TOF (see Figure 4.4) or PIN1 ΔE* vs. DSSD ΔE (see Figure 4.8). Therefore, final event selection included events from this cleaned TKE* plot AND'ed with fragments identified in PIN1 ΔE* vs. TOF.

CHAPTER 5

Experimental Results

Each of the nuclei produced and identified during this study was studied previously and the half-life was measured. The previously reported values are shown in Table 5.1. Half-life values below 10 s (^{84}Mo, ^{83}Nb, ^{81}Zr) are well suited to be measured by the above described setup and experimental conditions. This chapter centers on the analysis of ^{84}Mo; extracting the half-life of this nuclide was the principle aim of this work. A summary of the analysis of ^{83}Nb and ^{81}Zr, relevant to determining the β-detection efficiency (ε_{β}), is included in Appendix A. The energy spectrum for γ events that occurred in coincidence with ^{84}Mo β decay is presented. It was hoped that β decay from the 0^{+} ground state of ^{84}Mo would populate excited states in the ^{84}Nb daughter that would γ decay to the ground state. The β-delayed γ rays from ^{84}Mo could then be used to isolate coincident ^{84}Mo parent β decays from other decay generation and background β-decay events, providing a decay curve with reduced background. Unfortunately, no such γ rays were identified in this work. The implications on the spin assignment of the ^{84}Nb ground state based on the absence of delayed γ rays in the ^{84}Mo β-delayed γ-ray spectrum are discussed.

Three separate fitting methods were applied to the observed decay data to obtain a new half-life value for the ^{84}Mo ground state. The first was a least-squares linear

Table 5.1. Previously reported half-lives of the principle nuclei produced during this study.

Nucleus	β-Decay $T_{1/2}$
^{84}Mo	$3.7^{+1.0}_{-0.8}$ s [50]
^{83}Nb	4.1(3) s [51]
^{82}Zr	32(5) s [52]
^{81}Zr	5.3(5) s [53]
^{80}Y	30.1(5) s [54]
^{79}Sr	2.25(1) m [55]
^{76}Br	16.1(2) h [56]
^{74}Se	Stable (0.89% Abundant)
^{73}As	80.30(6) d [57]

regression method (Gaussian fit), the second approach involved the maximization of a Poisson distribution log-likelihood method (Poisson fit), and the third employed a custom probability density function (Maximum Likelihood fit) built to describe the decay of a radioactive nucleus of up to three generations.

A Gaussian distribution fit requires the data to be grouped in time-bins large enough that the histogram of the number of decay events as a function of time do not have bins with zero counts, which may cause the method to fail. Decay curves will always have an exponentially distributed error. An exponential error distribution violates the normal distribution expected for a least-squares analysis, though the exponential distribution (for a single order exponential) converges to the standard normal table at ∼60 counts/bin [58].

The second decay-event curve analysis procedure based on the maximization of a Poisson probability log-likelihood function and is, in principle, the same as the Gaussian fit procedure except for the error minimization. The χ^2_P minimization determined for the maximization of a Poisson distribution does not fail with zeroes present in the data set, yielding fit parameters that are independent of the number of counts in a bin [59]. A Poisson distribution strictly holds for nuclear decay processes that are characterized by a constant mean value observed over a collection time that is short compared to the half-life of the source [60]. The time window of five half-lives used to search for fragment-β correlations violated the condition of a correlation time that is short with respect to the half-life of the parent source. In addition, both the Gaussian and Poisson approaches require each event to be independent, which is not true of daughter and granddaughter (and so forth) decays in a radioactive chain. Over a correlation time of five parent half-lives, the contribution of daughter and granddaughter decay events to the total number of observed decay events can be significant, depending on the relative half-lives. This is especially true if the daughter and/or granddaughter half-lives are of the same order as the parent decay. In light of these shortcomings, a third, more rigorous approach for determining the β-decay half-life was employed.

The third approach was based on the maximization of a custom log-likelihood function. This Maximum Likelihood (MLH) fitting algorithm has been applied in previous work to determine β-decay half-lives from very few decay events [61, 62]. The likelihood functions used here were logical combinations of mathematical representations of the probabilities of observing one, two, or three decay events within an observation time equal to a window that is ten times the half-life of the nucleus of interest. The method assumes that the decay half-lives of the daughter and granddaughter generations are long enough that zero probability exists for a fourth generation decay event to occur within the allotted correlation time. The probability functions are based on the Bateman equations for the parent, daughter, and granddaughter decay events and a Poisson probability distribution for background events, and provide a correct mathematical model for the probability of observing up to three decay events.

Table 5.2. Table showing the yield of each isotope isolated during this study.

Nucleus	Implantations
^{84}Mo	1037
^{83}Nb	20121
^{82}Zr	56602
^{81}Zr	37246
^{80}Y	1054202
^{79}Sr	181544
^{76}Br	192441
^{74}Se	98164
^{73}As	511185

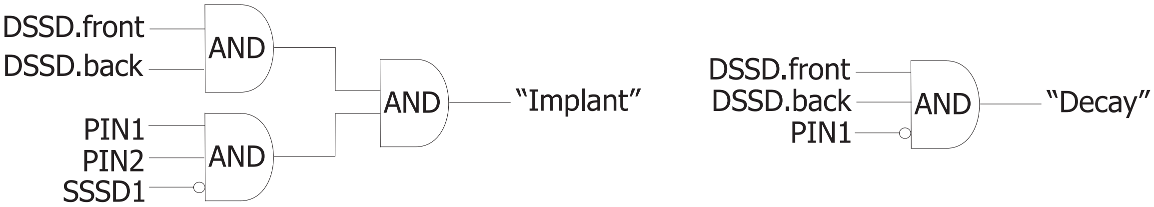

Figure 5.1. DSSD logical conditions set in software to determine the assignment of trigger events as implantations or decays.

5.1 Fragment-β Correlation

To correlate the implantation of an ion and its subsequent decay, each event has to be categorized as a decay or an implantation event. Logical conditions, shown in Figure 5.1, were established in software and used to assign trigger events as either implantations or decays. Implantations were identified by events that produced a signal above threshold in PIN1 and PIN2 and the front and back sides of the DSSD, with an additional condition that no signal was observed in the most upstream SSSD (SSSD1) i.e., fragments that stopped in the DSSD. Decays were identified by events that produced a signal above threshold in the front and back sides of the DSSD AND'ed with a requirement of no signal in PIN1.

In most cases, the event position can be determined by the strip with the largest energy signal. At times, the energy deposited by an event is nearly equal in adjacent strips on either the front or back side of the detector, which can result in an implantation or decay receiving the wrong position assignment to a pixel adjacent to where the event actually occurred. For this reason, the search algorithm for geometrically pairing implantation and decay events was expanded to consider events in nearby pixels. Software analysis algorithms were used to pair implantations to decay events that occurred within fixed correlation time in the same-pixel and nearest-neighbor pixels. This five-pixel search geometry (see Figure 5.2) was applied for implantation and subsequent decay events that occurred within a correlation time equal to five times the half-life of the nucleus under study; the resulting decay curves were fitted by the Gaussian and Poisson distribution error minimization methods. The five-pixel search geometry was then extended to determine fragment correlations with up to three subsequent decay events that occurred within a ten half-life correlation time after an implantation; the resulting decay chain data were fitted by the custom MLH algorithm.

The maximum possible correlation time was limited by the average time between successive implantations in a single pixel. Since the five-pixel search geometries assigned decay events to the immediately preceding implantation in the search area, a fragment implantation has some probability to be correlated to a decay from any of the previously implanted fragments within the search geometry. The likelihood for a false correlation therefore increases if a fragment implantation occurs within both the search geometry and correlation time of a short-lived (^{84}Mo, ^{83}Nb, ^{81}Zr) previous implantation. The low overall implantation rate of 10 Hz distributed over roughly 3/4 the face of the DSSD corresponded to an average time between successive implantations in a single pixel of $\sim$120 s. A correlation time of ten times the half-life of ^{84}Mo, taking the previously measured literature value as an upper limit, would be 47 s at

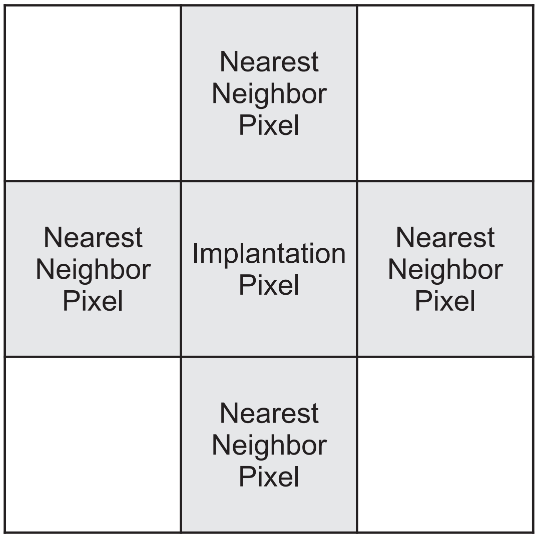

Figure 5.2. Schematic representation of the five-pixel correlation geometry used for correlating implantation and decay events in this work. Center pixel marked "Implantation Pixel" indicates the location of the fragment implantation. Grayed out boxes represent pixels that were searched for decay events within a fixed correlation time to pair to the implantation.

most, well within the 120 s limit. A correlation time that is well below the average time between implantations in a single pixel does not guarantee that each decay will be correlated to the proper fragment. For example, as the 120-s time between implantations represents an average, half of ^{84}Mo implantations will occur within less than 120 s of another implantation in the same pixel. In the event that an implantation occurred in the same pixel after a ^{84}Mo implantation but before a decay event in the five-pixel search geometry, the decay event was linked to the second implantation. Therefore, if the ordering of the ^{84}Mo and the second implantations were reversed, the ^{84}Mo implantation was linked to the decay. The improper linking of a decay and implantation will result in a false correlation. It is not possible to distinguish between decays from recent and previous implantations through methods of geometric and time correlation. Consequently, each fit performed in this analysis contained a component of background to approximate the contribution of false correlations to the total number of β events correlated to a particular isotope.

5.2 Maximum Likelihood Method

The full development and formal description of the MLH method have been described previously [30, 63], only a brief summary will be provided here. This description, as explained in the introduction to Chap. 5, demonstrates the logical and mathematical correctness of the MLH method for describing the probabilities for observing up to three decay generations of a parent nucleus within a fixed correlation time.

β-Detection Efficiency

The implantation of radioactive fragments into the front 1/3 of the DSSD optimized the path length through the detector for β particles emitted in the downstream direction. The probability for detecting a given decay event is a necessary parameter for a probability density function that describes the observed decay sequence in a radioactive chain. ε_β is defined as $\varepsilon_\beta \equiv (N_\beta/N_I)$, where N_β is the number of observed β events from a parent nucleus and N_I is the number of observed parent implantations. N_I was determined directly from the number of fragments identified for each isotope from the particle identification plot. The N_I for each isotope are listed in Table 5.2. N_β was determined for ^{84}Mo, ^{83}Nb, and ^{81}Zr from the fitted decay curve data as described in detail in Appendix A. The value $\varepsilon_\beta = 0.34(2)$ was deduced from a weighted average of the values of ε_β for ^{84}Mo, ^{83}Nb, and ^{81}Zr, as given in detail in Table A.1.

Data Input Format

The text input file for the MLH fit contained a user defined header that immediately preceded the decay-chain data. The input parameters are specified in Table 5.3. Each

Table 5.3. Table of input parameters and data provided to MLH fit program. The first five lines of input are reserved for a user-defined header. Decay-times immediately follow, input as four-element arrays. All time values are entered in units of seconds. Probabilities are entered as decimal fractions. The symbols are defined as follows: t_c - correlation time; β_D - β-decay daughter; β_{GD} - β-decay granddaughter; P_D - proton-decay daughter; P_{GD} - proton-decay granddaughter; β_D-P_D - proton-decay daughter of β-decay daughter; $t_{\beta i}$ - time of ith observed βevent; r_b - background rate.

T_{corr}			
$\mathrm{T}_{1/2}$ [Parent] (guess)	$\mathrm{T}_{1/2}$ [β_D]	$\mathrm{T}_{1/2}$ [β_{GD}]	
P_n [Parent]	P_n [β_D]	P_n [P_D]	
$\mathrm{T}_{1/2}$ [P_D]	$\mathrm{T}_{1/2}$ [P_{GD}]	$\mathrm{T}_{1/2}$ [β_D-P_D]	
ε_β [Parent]	ε_β [β_D]	ε_β [β_{GD}]	
$t_{\beta 1}$	$t_{\beta 2}$	$t_{\beta 3}$	r_b
$\vdots$	$\vdots$	$\vdots$	$\vdots$

fragment implantation was correlated with up to three decay events that occurred within a five-pixel search geometry during a correlation time approximately ten times the half-life of the nucleus of interest. The decay-chain data were stored as separate four-element arrays for each decay sequence that contained entries for the times of the first, second, and third observed decays and the background rate in the pixel where the decay chain was observed.

Background Treatment

The implantation density distribution of the secondary beam over the face of the DSSD was not uniform. The non-uniformity of the distribution was exacerbated by the position-TOF correlation created by the RFFS. In fact, the TOF dependent vertical deflection experienced by beam fragments resulted in each receiving a unique placement on the DSSD detector face. Consequently, a particular isotope was concentrated in a region of only roughly 1/3 the area of the DSSD. The histograms in Figure 5.3 depict the DSSD implantation profiles for ^{84}Mo and for all isotopes. A similar set of histograms for the principle beam contaminants ^{80}Y and ^{79}Sr are shown in Figures 5.4A and B, respectively. The unique placement of each isotope on the DSSD face resulted in a unique background environment in each pixel. Some isotopes were implanted in a similar region of the DSSD as ^{84}Mo; other isotopes were not, and thus did not significantly contribute background to ^{84}Mo analysis. Therefore approximating the background rate by an average value for the entire face of the DSSD would not be an appropriate representation of the background.

Ideally, a history of the implantations in each DSSD pixel would be extracted from the data. A background rate in a particular pixel for a given time period could then be determined from summing the background contribution of each isotope implanted in that pixel. The background contribution at a particular time from each isotope can be calculated based on the decay constant and the implantation time of the isotope; this method was employed in a recent work measuring the β-decay half-life of ^{100}Sn with very few implantations [62]. The statistics gathered for ^{84}Mo were 100 times what was collected for ^{100}Sn, and the observed background rate in this experiment was low enough that the probability to observe a background event during the correlation time was ∼2%. Therefore, it was considered sufficient in this work to approximate the background with a moving boxcar method that measured the observed background rate per pixel for the run during which a decay chain was observed. The length of each single run was approximately one hour. The applied background rate for each MLH decay chain was interpolated from the background measurement in the relevant pixel during the overlapping one-hour period. Decay events were considered non-correlated (background) if either they did not fall within the correlation-time window, or if they were the fourth or higher decay event to occur during the correlation window. Background events are assured to occur independently of the decay-chain events; the probability for observing a number (n) of background events within a correlation time

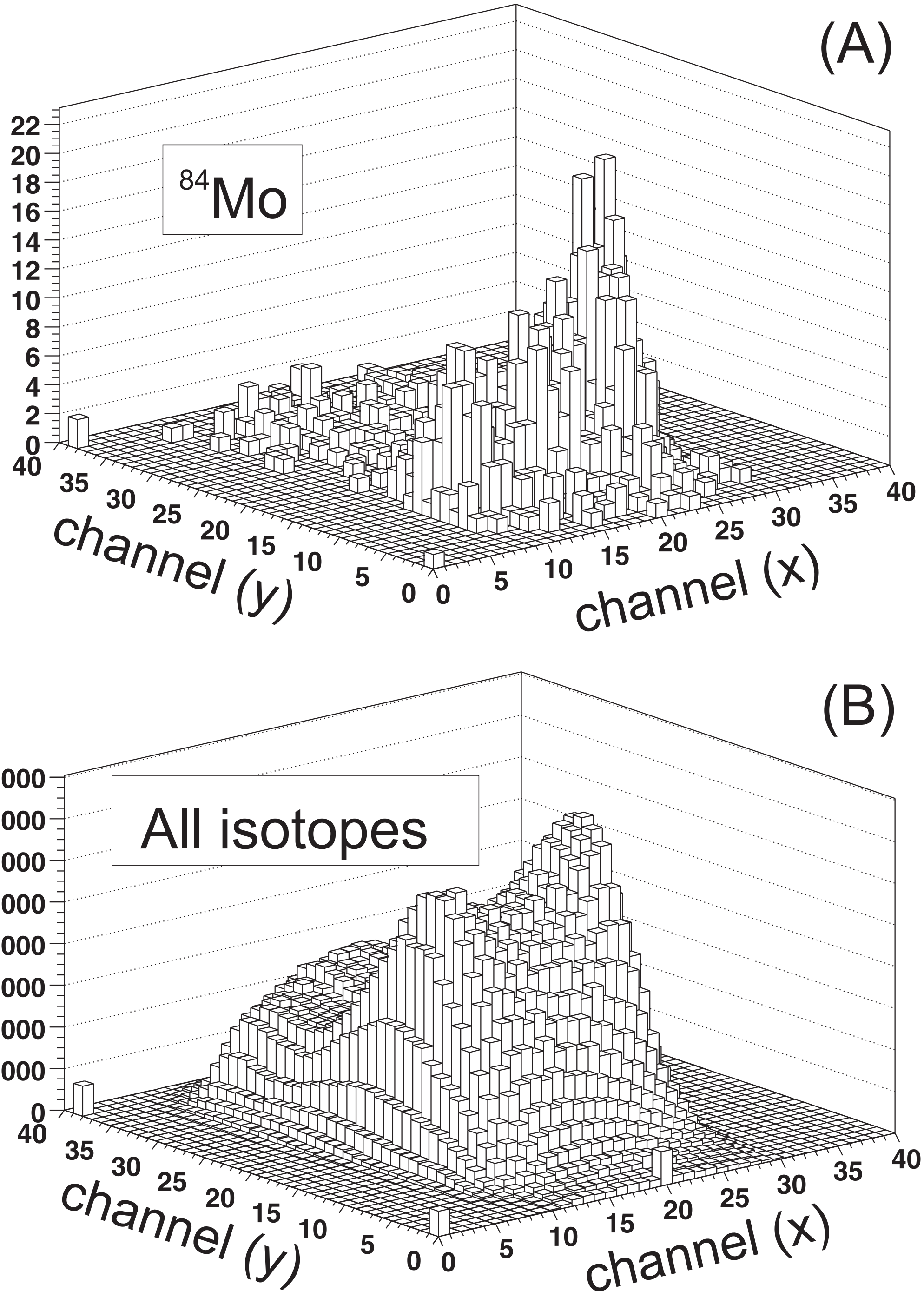

Figure 5.3. Implantation profiles over the face of the DSSD. (A) The implantation profile specific to ^{84}Mo. (B) The same for all fragments. A background rate was measured in each pixel to accurately account for the unique environment at each pixel position.

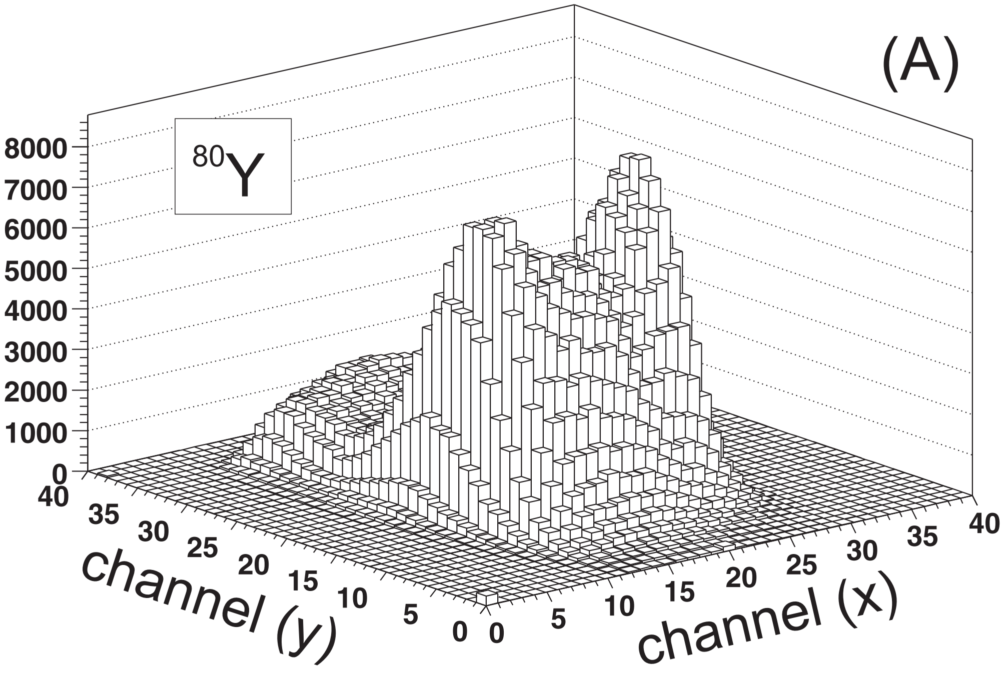

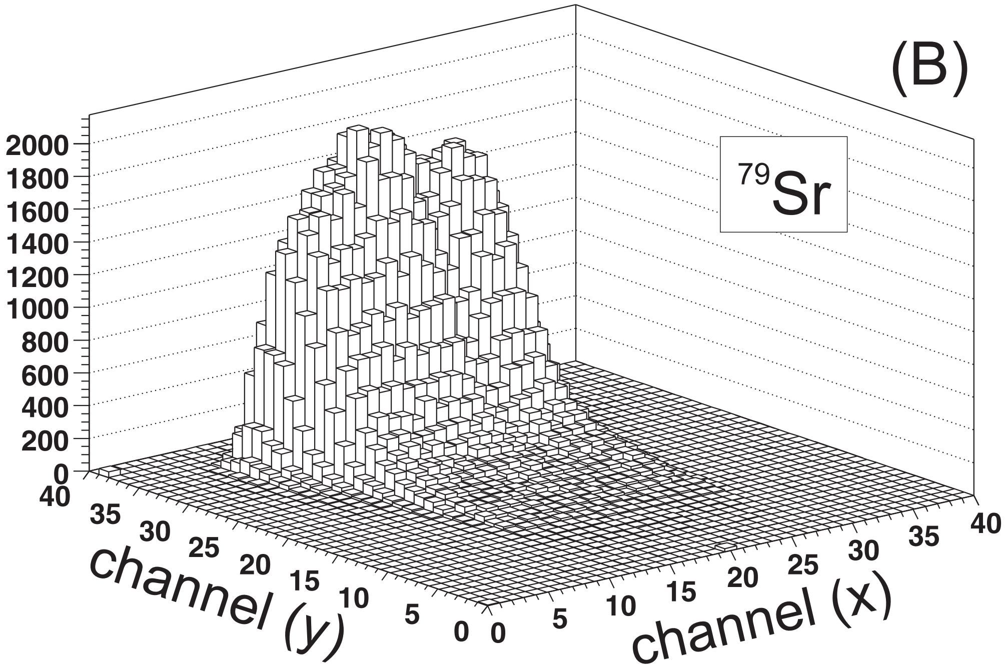

Figure 5.4. Similar to Figure 5.3. (A) The implantation profile specific to ^{80}Y. (B) The same is shown for ^{79}Sr in the image below. The high production rates and relatively short half-lives of these species made them the principle sources of decay-event background.

(t_c) for a measured background rate (r_b) was described by a Poisson probability

$$B_n = \frac{(r_b t_c)^n e^{-r_b t_c}}{n!}, \tag{5.1}$$

where B_n indicates the probability of observing n background events within t_c. B_0 is the probability of observing zero background events within t_c, B_1 is the probability of observing one background event within t_c, etc.

Probability Density Functions

The DSSD ΔE signal from the β decay of implanted nuclei does not provide an unique energy signature for identification. The fact that $\varepsilon_\beta < 100\%$ allows events other than the parent β decay to be detected as the first event after an implantation. The decay times of β-decay events along the decay chain are not independent, so the likelihood function must account for this dependency. The decay constants of the parent, daughter, and granddaughter nuclei are defined here as λ_1, λ_2, and λ_3, respectively. The probability density function, $f_i(\lambda_1, \lambda_2, \ldots, \lambda_i, t)$, for a radioactive decay at time t from a single parent nucleus for the parent, daughter, and granddaughter species are described by a form of the Bateman equations given by Equations (2.12), (2.13), and (2.14) with $n_1(0) = 1$ and satisfy the relation

$$\int_0^\infty f_i(\lambda_1, \lambda_2, \ldots, \lambda_i, t)\mathrm{d}t = 1. \tag{5.2}$$

The integration time is limited by the average implantation rate into each pixel, therefore, the integration in this analysis was carried out over a value of t_c. The probability that a decay will occur within t_c is therefore not unity, so a normalization constant is required to properly implement the probability density function into the fitting algorithm. The probability for occurrence is distinct from the probability for detection, which factors in ε_β and the rate of background decays. The integrated form of the probability for occurrence of the first three members of a decay chain are:

$$F_1(\lambda_1, t_c) = 1 - e^{-\lambda_1 t_c} \tag{5.3}$$

$$F_2(\lambda_1, \lambda_2, t_c) = 1 - \frac{\lambda_2 \lambda_1}{\lambda_2 - \lambda_1}\left[\frac{1}{\lambda_1} e^{-\lambda_1 t_c} - \frac{1}{\lambda_2} e^{-\lambda_2 t_c}\right] \tag{5.4}$$

$$\begin{aligned} F_3(\lambda_3, \lambda_2, \lambda_1, t_c) = 1 - \lambda_3 \lambda_2 \lambda_1 \Bigg[& \frac{e^{-\lambda_1 t_c}}{\lambda_1(\lambda_2 - \lambda_1)(\lambda_3 - \lambda_1)} + \\ & \frac{e^{-\lambda_2 t_c}}{\lambda_2(\lambda_1 - \lambda_2)(\lambda_3 - \lambda_2)} + \frac{e^{-\lambda_3 t_c}}{\lambda_3(\lambda_1 - \lambda_3)(\lambda_2 - \lambda_3)}\Bigg]. \end{aligned} \tag{5.5}$$

The total likelihood function considers circumstances where 0, 1, 2, or 3 decay events are detected within t_c. Multiple scenarios exist that can result in the detection of each number of events. Since ε_β is not unity, the detection of one event can be attributed to observing a parent, daughter, granddaughter, or background decay. ε_β for parent, daughter, and granddaughter decays is uniquely displayed as $\varepsilon_{\beta 1}$, $\varepsilon_{\beta 2}$, and $\varepsilon_{\beta 3}$, respectively, to provide clarity in the following equations. However, $\varepsilon_{\beta 1} = \varepsilon_{\beta 2} = \varepsilon_{\beta 3}$ was assumed during the analysis. The notation $\overline{\varepsilon}_\beta$ represents the quantity $1 - \varepsilon_\beta$. The probability for each circumstance of zero to three detected decays is determined by logically combining (+ for OR, · for AND) the probabilities for observing a given decay chain or background event. The four scenarios describing one detected event used in this analysis are as follows:

(1) The decay of the parent was observed, the daughter and granddaughter decays did not happen or were not observed, and a background event did not occur:

$$P_{1p} = D_1 \varepsilon_{\beta 1} \cdot (\overline{D}_2 + D_2 \overline{\varepsilon}_{\beta 2} \overline{D}_3 + D_2 \overline{\varepsilon}_{\beta 2} D_3 \overline{\varepsilon}_{\beta 3}) \cdot B_0. \tag{5.6}$$

(2) The decay of the daughter was observed, the parent decay happened and was not observed, the granddaughter decay did not happen or was not observed, and a background event did not occur:

$$P_{1d} = D_1 \overline{\varepsilon}_{\beta 1} D_2 \varepsilon_{\beta 2} \cdot (\overline{D}_3 + D_3 \overline{\varepsilon}_{\beta 3}) \cdot B_0. \tag{5.7}$$

(3) The decay of the granddaughter was observed, the parent and daughter decays happened and were not observed, and a background event did not occur:

$$P_{1g} = D_1\overline{\varepsilon}_{\beta 1}D_2\overline{\varepsilon}_{\beta 2} \cdot D_3\varepsilon_{\beta 3} \cdot B_0. \tag{5.8}$$

(4) A background decay was observed, the parent and daughter and granddaughter decays did not happen or were not observed:

$$P_{1b} = (\overline{D}_1 + D_1\overline{\varepsilon}_{\beta 1}\overline{D}_2 + D_1\overline{\varepsilon}_{\beta 1}D_2\overline{\varepsilon}_{\beta 2}\overline{D}_3 + D_1\overline{\varepsilon}_{\beta 1}D_2\overline{\varepsilon}_{\beta 2}D\overline{\varepsilon}_{\beta 3}) \cdot B_1 \tag{5.9}$$

where D_i ($\overline{D}_i$) represents the probability that a decay of the *ith* generation happens (does not happen). The subscript of the function label denotes the number of observed decays and the decay-generation member or background to which the decay is assigned, where p is a parent decay, d a daughter decay, g a granddaughter decay, and b a background decay. Therefore P_{1p} indicates the probability for detecting one parent decay event. P_{1d}, P_{1g}, and P_{1b} similarly imply detection of a daughter, granddaughter, and background event, respectively.

A similar mathematical description can be written for the ten possible scenarios that describe observing two decay events, which must account for combinations of decays as well as the order in which they occurred. Consistent with the notation above, the scenarios are indicated by P_{2pd}, P_{2pg}, P_{2pb}, P_{2dg}, P_{2db}, P_{2gb}, P_{2bp}, P_{2bd}, P_{2bg}, and P_{2bb}. For example, P_{2pd} is the probability for detecting a parent decay followed by the detection of a daughter decay; this parent-daughter detection scheme considers that the granddaughter did not happen or was not observed and that a background event did not occur. The meaning of the other notations representing two event detection probability is similarly consistent with the ordering of the letters in the subscript. There are twenty possible detection scenarios for observing three decay events, which are: P_{3pdg}, P_{3pdb}, P_{3pgb}, P_{3pbd}, P_{3pbg}, P_{3pbb}, P_{3dgb}, P_{3dbg}, P_{3dbb}, P_{3gbb}, P_{3bpd}, P_{3bpg}, P_{3bpb}, P_{3bdg}, P_{3bdb}, P_{3bgb}, P_{3bbp}, P_{3bbd}, P_{3bbg}, P_{3bbb}.

Of course, only one scenario exists to describe the probability for observing no decay events (P_0).

The probability distribution functions for detection of one decay during t_c are a mathematical extension of the logical construction of observation probabilities. The probability density functions for observing one decay event at time t_1 within t_c are:

$$\begin{aligned}
p_{1p}(\lambda_1) &= C_1 \cdot f_1(\lambda_1, t_1) \cdot \varepsilon_{\beta 1} \cdot [\overline{F}_1(\lambda_2, t_c - t_1) + (\overline{F}_2(\lambda_2, \lambda_3, t_c - t_1) - \\
&\quad \overline{F}_1(\lambda_2, t_c - t_1)) \cdot \overline{\varepsilon}_{\beta 2} + F_2(\lambda_2, \lambda_3, t_c - t_1) \cdot \overline{\varepsilon}_{\beta 2}\overline{\varepsilon}_{\beta 3}] \cdot B_0 \qquad (5.10) \\
p_{1d}(\lambda_1) &= C_1 \cdot f_2(\lambda_1, \lambda_2, t_1) \cdot \overline{\varepsilon}_{\beta 1}\varepsilon_{\beta 2} \cdot [\overline{F}_1(\lambda_3, t_c - t_1) + \\
&\quad F_1(\lambda_3, t_c - t_1) \cdot \overline{\varepsilon}_{\beta 3}] \cdot B_0 \qquad (5.11) \\
p_{1g}(\lambda_1) &= C_1 \cdot f_3(\lambda_1, \lambda_2, \lambda_3, t_1) \cdot \overline{\varepsilon}_{\beta 1}\overline{\varepsilon}_{\beta 2}\varepsilon_{\beta 3} \cdot B_0 \qquad (5.12) \\
p_{1b}(\lambda_1) &= C_1 \cdot [\overline{F}_1(\lambda_1, t_c) + (\overline{F}_2(\lambda_1, \lambda_2, t_c) - \overline{F}_1(\lambda_1, t_c)) \cdot \\
&\quad \overline{\varepsilon}_{\beta 1} + (\overline{F}_3(\lambda_1, \lambda_2, \lambda_3, t_c) - \overline{F}_2(\lambda_1, \lambda_2, t_c)) \cdot \overline{\varepsilon}_{\beta 1}\overline{\varepsilon}_{\beta 2} + \\
&\quad F_3(\lambda_1, \lambda_2, \lambda_3, t_c) \cdot \overline{\varepsilon}_{\beta 1}\overline{\varepsilon}_{\beta 2}\overline{\varepsilon}_{\beta 3}] \cdot B_1 \cdot t_c^{-1}. \qquad (5.13)
\end{aligned}$$

The sum of the single decay probability density functions define the joint probability density function for one observed decay event:

$$p_1(\lambda_1) = p_{1p}(\lambda_1) + p_{1d}(\lambda_1) + p_{1g}(\lambda_1) + p_{1b}(\lambda_1), \qquad (5.14)$$

where the normalization constant C_1 fulfills the equation:

$$\int_0^{t_c} p_1(\lambda_1, t)\mathrm{d}t_1 = 1. \qquad (5.15)$$

The joint probability density functions $p_2(\lambda_1)$ and $p_3(\lambda_1)$ are similarly formed from the sum of all two- and three-decay scenario probability density functions.

Likelihood Function

The resulting likelihood function combines the one-, two-, and three-decay joint probability density functions:

$$\mathcal{L}_{123}(\lambda_1) = \prod_{i=1}^{N_{123}} [\delta(n_i - 1) \cdot p_1(\lambda_1) + \delta(n_i - 2) \cdot p_2(\lambda_1) + \delta(n_i - 3) \cdot p_3(\lambda_1)]. \quad (5.16)$$

$\delta(x)$ represents the delta function, where $\delta(x) = 1$ for $x = 0$, and $\delta(x) = 0$ for all other values of x. Equation (5.16) considers the combined set of N_{123} observed decay chains with one ($n_i = 1$), two ($n_i = 2$), or three ($n_i = 3$) decay events within t_c. The most probable value of λ_1 determined from Eq. (5.16) was then corrected for implantation events with no observed decays (N_0) within t_c using an iterative numerical method. The value of N_0 within t_c depends on $P_0(\lambda_1)$:

$$N_0 = \frac{P_0(\lambda_1)}{1 - P_0(\lambda_1)} \cdot N_{123} \quad (5.17)$$

A value of t_c more than five half-lives of the parent nucleus ensures that this correction applied for N_0 events is less than 5%. If the average rate of implantation into a single pixel is low enough, a t_c equal to ten half-lives should be used to make the N_0 correction less than 1%. A longer value of t_c potentially allows for contributions from decay generations beyond the granddaughter species, voiding the assumption of three decays used for the construction of the likelihood function.

5.3 ^{84}Mo

The decay curve for β events that occurred within 10 s in the same pixel or the four nearest-neighbor pixels of a ^{84}Mo implantation is shown in Figure 5.5. In total, 532 correlated decay events were observed. Each species along the decay chain of ^{84}Mo reaching to β stability, along with background events, are potential contributors to the overall decay curve. The Gaussian fit of the decay data shown in Figure 5.5

was based on a least-squares regression analysis that considered the contributions of parent, daughter, and granddaughter decays [described by equations (2.12), (2.13), and (2.14)] and a linear background component. The daughter and granddaughter half-lives were taken as fixed parameters, based on the previously determined half-lives of 9.5 s [54] and 25.9 min [64] for the daughter (^{84}Nb) and granddaughter (^{84}Zr), respectively. The data were histogrammed in 1 s time bins to ensure that no data points had zero counts. The difficulty with the Gaussian fit is illustrated in Table 5.4. Time binning of 1 s produced some data points that contained fewer than the value of 60 counts per time bin necessary to approximate a normal error distribution required for a "good" least-squares fit. An increase in the time bin size to 2.5 s was necessary to achieve ≥ 60 counts/time bin. However, such binning resulted in only one degree of freedom in the fit and an overestimation of the experimental error. The half-life and error determined using 1 s bins was 1.9(4) s. The contribution of daughter and granddaughter decays to the total number of observed decays were calculated based on this 1.9 s half-life. The integrated contribution of the granddaughter decay, as anticipated, was not significant (≤ 0.01 counts/10 s) as a result of its relatively long half-life.

A half-life of 2.0(4) s was deduced for ^{84}Mo from the Poisson fit of the decay curve, considering the decay of the parent and daughter and a linear background. The fit using Poisson probability distributions did not include the decay of the granddaughter, since its contribution was shown in the Gaussian fit to be small. The half-life of ^{84}Mo from the maximization of a Poisson distribution log-likelihood function provided the advantage of yielding the same result independent of the histogram bin size. Table 5.4 contains the half-lives deduced for ^{84}Mo based on the selected bin size. The robustness of the Poisson probability likelihood maximization fit to a change in bin size is clear, though an extreme reduction in the number of degrees of freedom results in an overestimate of the experimental error. The number of parent and

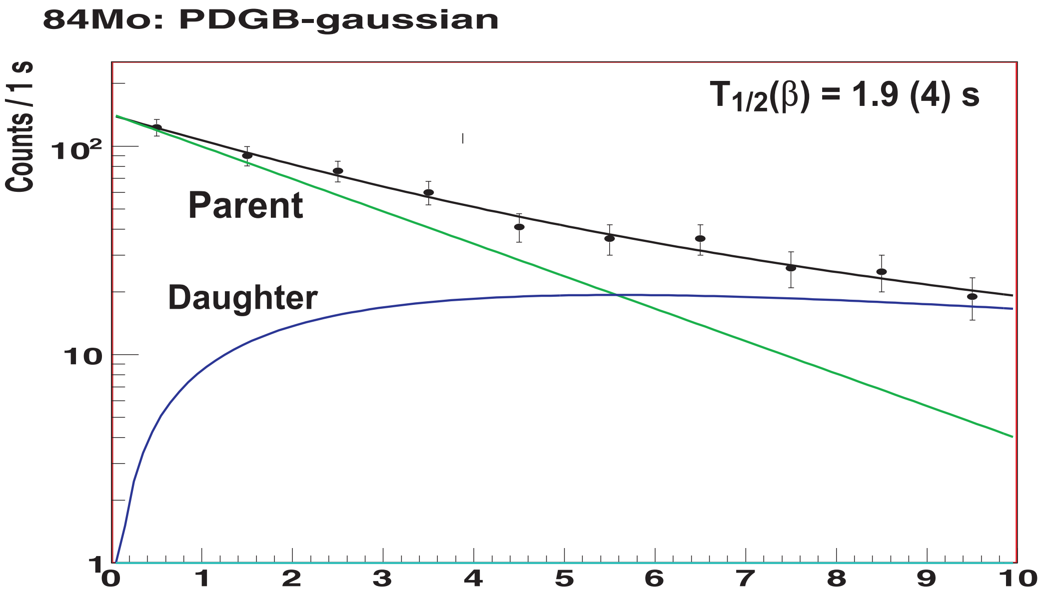

Figure 5.5. Decay curve for ^{84}Mo. The fit represents the results of a least-squares regression analysis. Data were fitted by the sum of the Bateman equations [Equations (2.12), (2.13), and (2.14)] corresponding to contributions from the parent, daughter, and granddaughter, and a constant background term. The daughter and granddaughter half-lives of 9.5 s and 1554 s, respectively, were taken as fixed parameters. Only the initial activity, parent decay constant, and background were free parameters in the fit. The fitted background rate of < 0.1 counts/s and the granddaughter component, which integrates to < 0.01 counts, lies below the horizontal axis.

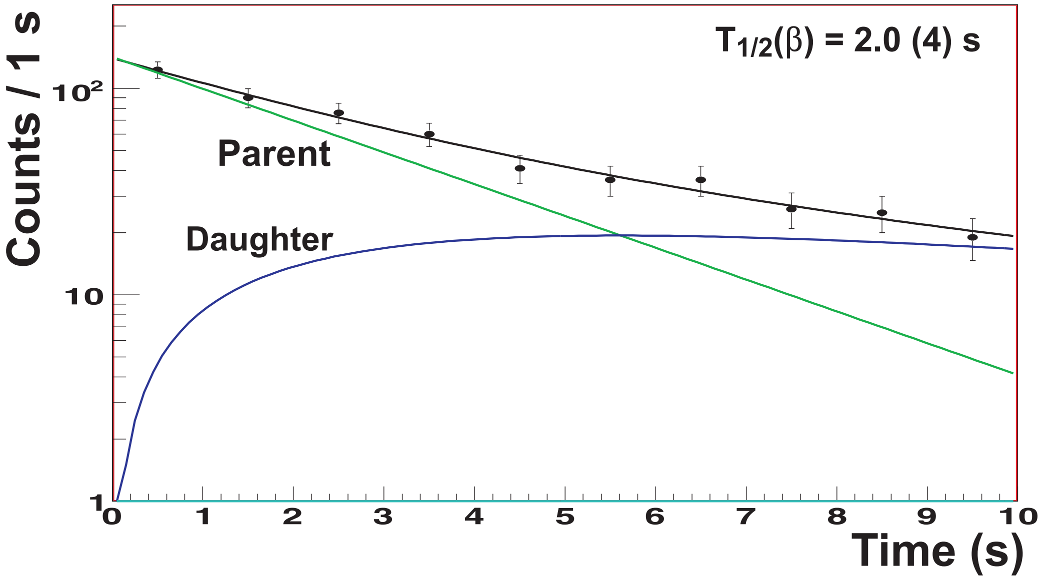

Figure 5.6. Decay curve for ^{84}Mo. The fit represents the results of the maximization of a Poisson distribution log likelihood function. Data were fit by the sum of the Bateman equations [Equations (2.12) and (2.13)] corresponding to contributions from the parent and daughter, and a constant background term. A daughter half-life of 9.5 s was taken as a fixed parameter. The initial activity, parent decay constant, and background were free parameters in the fit. The fitted background rate of < 0.1 counts/s lies below the horizontal axis.

daughter nuclei contributing to the decay curve were determined from the fit. Of the 532 decays correlated with ^{84}Mo implantations, 135(11) were attributed to the daughter. Therefore, ∼25% of the total data set cannot be considered independent. Accurate determination of the ^{84}Mo half-life required that these daughter events either be filtered from the data set by identifying a parent-decay-coincident γ-ray, or be properly accounted for by the probability distribution function used for maximum likelihood determination.

Table 5.4. Comparison of the half-lives deduced using Gaussian and Poisson probability distributions for ^{84}Mo based on bin size. The χ^2_P minimization using Poisson statistics can be robustly applied to data sets independent of bin size.

	Probability Distribution		Fraction of	No. of
s / bin	Gaussian	Poisson	Bins with 0 Counts	Bins
0.01	1.1(1.4)	2.0(4)	0.748	1000
0.02	1.8(1.5)	2.0(4)	0.578	500
0.05	1.3(3)	2.0(4)	0.15	200
0.1	1.6(3)	2.0(4)	0.06	100
0.2	2.0(4)	2.0(4)	0	50
0.5	2.1(4)	2.0(4)	0	20
1	1.9(4)	2.0(4)	0	10
2	1.9(4)	1.9(4)	0	5
2.5	2.0(5)	2.0(5)	0	4

5.3.1 Maximum Likelihood Analysis

The histograms representing the decays that occurred within 20 s in the same pixel of a ^{84}Mo implantation are shown in Figure 5.7 as a plot of log time. The data are marked to indicate decays observed as the first, second, or third decay events within t_c. The probability distribution functions determine the maximum likelihood for the assignment of decay-chain events as parent, daughter, granddaughter, or background events. In total, 640 correlated decay chains were observed. The header of input parameters entered into the MLH is detailed in Table 5.3. A half-life of 2.2(2) s was determined for ^{84}Mo using the MLH analysis. This value is consistent with the values deduced from the Poisson and Gaussian distributions. The improved precision is a reflection of the larger data set analyzed due to the 20 s t_c and the mathematical treatment of daughter and granddaughter decay times as dependent parameters.

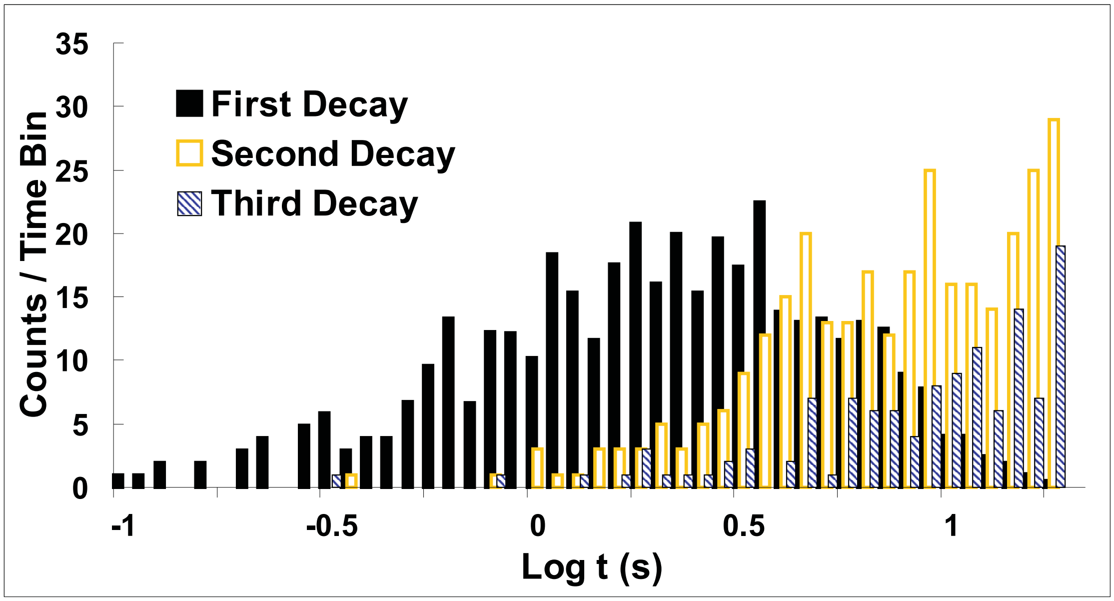

Figure 5.7. Histogram representing the natural log of the decay times relative to and correlated with ^{84}Mo implantations within a five-pixel geometry during a 20 s time window. The closed histogram represents the first detected correlated β decays, which represent a combination of parent, daughter, and background events since ε_β was not unity. The second decays, represented by the open histogram, principally are made up of daughter decays due to the low background rate. The third observed decays, represented by the thatched histogram, consist largely of background events since the half-life of the granddaughter was long.

5.3.2 β-Delayed γ's

As noted earlier, another way to isolate ^{84}Mo parent β decays would be to gate the decay curve on known γ-ray transitions in the ^{84}Nb daughter. Unfortunately, no information on β-delayed γ rays following ^{84}Mo was available. As part of the measurements reported here, the energy spectrum for γ events that occurred in coincidence with the ^{84}Mo β decay chain was recorded and is shown in the spectrum in Figure 5.8. The peak at 511 keV represents the energy of the photons produced during positron annihilation. The only obvious γ ray energy peak, with the exception of the 511-keV annihilation peak, is labeled at 386 keV (13 counts), and represents the decay of the 2_1^+ state in ^{80}Sr fed from ^{80}Y β decay. The β decay from ^{80}Y was the chief source of background in this ^{84}Mo analysis due to the full position overlap on the DSSD face of ^{80}Y and ^{84}Mo implantations (see Figures 5.3A and 5.4A); the rate of ^{80}Y implantations; and, the half-life of ^{80}Y, which is of order seconds. A fuller discussion of ^{80}Y background from β events is provided in Sec. 5.3.3.

Allowed β decays from the 0^+ ^{84}Mo ground state would populate 1^+ states in ^{84}Nb. Identifying ^{84}Nb γ-ray transitions from one or more 1^+ states fed from ^{84}Mo β decay would allow the isolation of parent decay events from daughter decay events. Previous work [65] identified high-spin excited states in ^{84}Nb populated through the ^{58}Ni(^{28}Si,pnγ) reaction, and reported a 3^+ assignment for the ^{84}Nb ground state. Such spin-parity assignments are consistent previous β-decay work [33, 66]. However, the tentative spin and parity assignments of the higher-lying states shown in Figure 5.9, as well as later ^{84}Nb β-decay studies [34] do not rule out the possibility of $J^\pi =$ 1^+ or 2^+ for the ^{84}Nb ground state. The states below 1 MeV established in Ref. [65] are shown in the level scheme in Figure 5.9. A more recent in-beam study of ^{84}Nb excited states confirmed the energies of the states identified in the spectrum in Figure 5.9, as well as identifying the transition to the ground state from the 48-keV level [67]. The ^{84}Nb levels at energies 48.0, 65.0, 205.0, and 217.5 keV are potential

$J^{\pi} = 1^{+}$ candidates, based on their direct decay transitions to the $J^{\pi} = 1^{+}$, 2^{+}, or 3^{+} ground state. However, the 338.0 keV (5^{-}) isomeric state directly feeds the 205.0 level, making a 1^{+} assignment unlikely. The (5^{-}) isomeric state also feeds both the 48.0 and 65.0 keV levels via a 2-γ cascades, reducing their likelihood of being 1^{+} states as well. The 217.5 keV level was the most obvious $J^{\pi} = 1^{+}$ candidate, as it is fed solely via a 4-γ cascade from the (8^{+}) state at 865.4 keV.

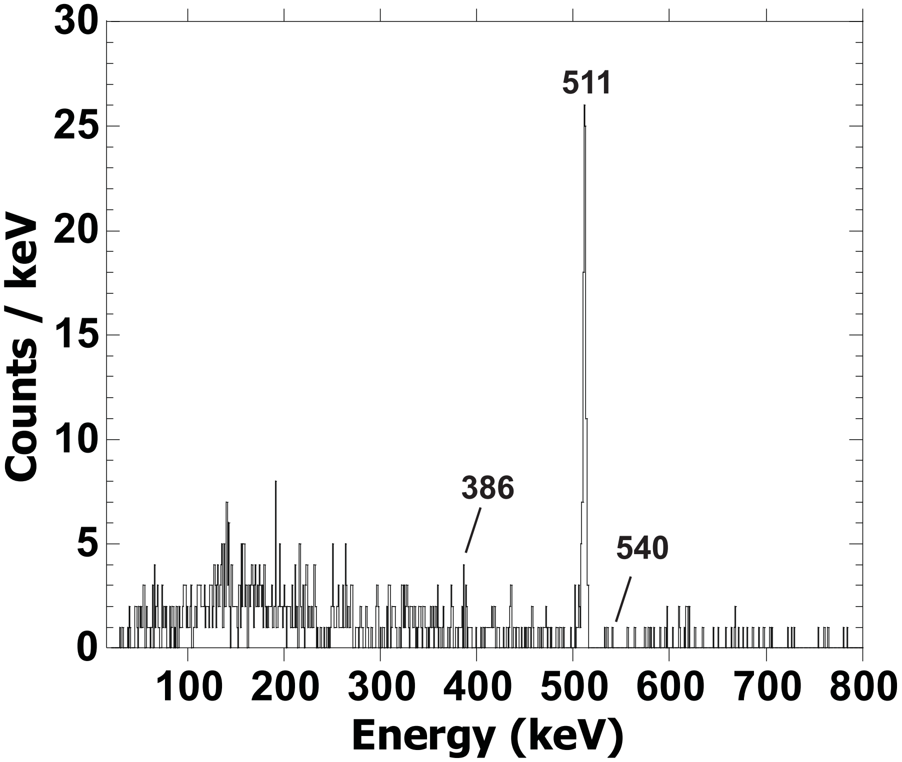

Figure 5.8. Spectrum of γ rays in the energy range 50-800 keV in coincidence with β-decay events occurring in the same and the four nearest-neighbor pixels within 10 s of a ^{84}Mo implantation. The transition with energy 386 keV represents the decay of the 2_1^{+} state in ^{80}Sr fed from ^{80}Y β-decay, the principle source of background decay events. Additional details are in the text.

Based on the assumption that 100% of the ^{84}Mo β-decay fed states in ^{84}Nb

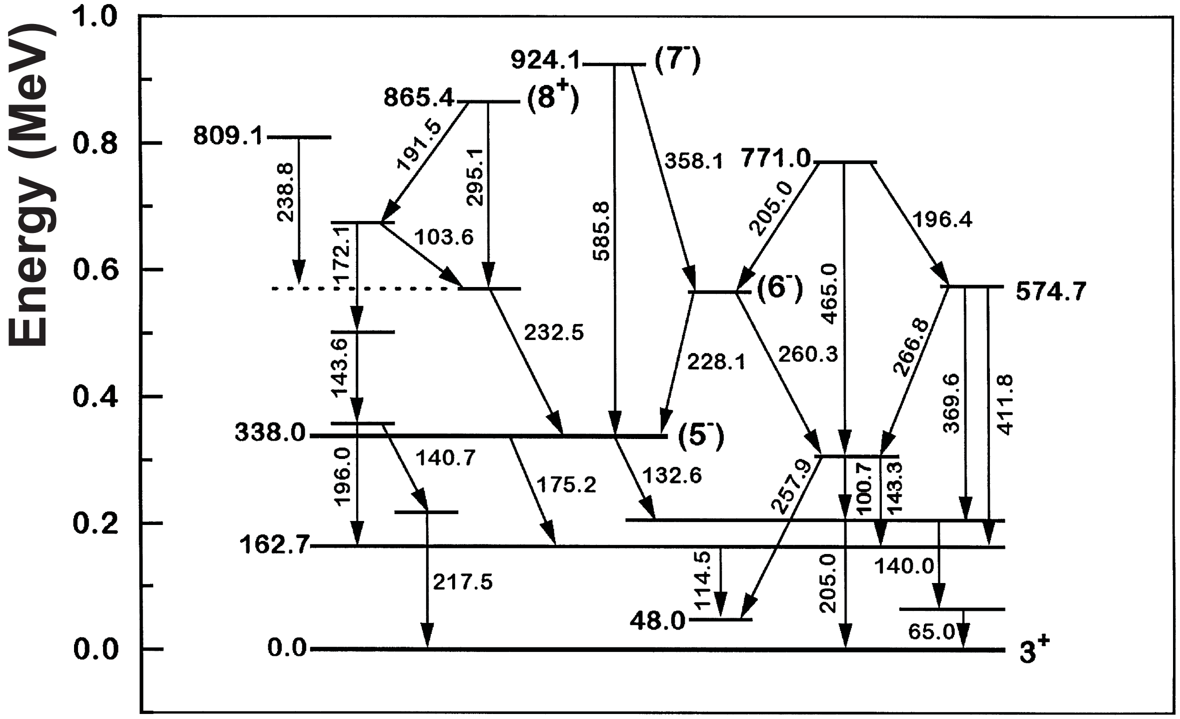

Figure 5.9. Level scheme below 1 MeV for ^{84}Nb established from the ^{58}Ni(^{28}Si,pnγ) reaction. Taken from Ref. [65].

cascade through a single state within the 60-400 keV energy range and knowing that the absolute efficiency for SeGA in this energy range was 12% or greater, more than 45 counts should have been observed, perhaps at 217 keV, in the delayed γ-ray spectrum depicted in Figure 5.8. For comparison, the 511-keV annihilation peak has 99 counts. The absence of γ rays from known excited states in ^{84}Nb prevented isolation of parent decays from daughter decays and background events using β-γ coincidence filtering of the ^{84}Mo decay curve. Absence of the ^{84}Nb delayed γ rays in the spectrum in Figure 5.8 also has implications on the ground-state spin of ^{84}Nb. Previous β-decay work would support spin and parity assignments to the ^{84}Nb ground state of 1^+, 2^+, or 3^+ [34]. Decay from the 0^+ ground state of ^{84}Mo directly to the ^{84}Nb ground state would suggest a 1^+ spin and parity assignment.

The tentative spin and parity assignment of 1^+ to the ^{84}Nb ground state is also supported by the absence of γ-ray transitions attributable to β-fed states in the ^{84}Mo granddaughter, ^{84}Zr. The study of excited ^{84}Zr states fed by β decay was reported in Ref. [34]. The projection of the β-gated γ-γ matrix for all $A = 84$ isobars produced via the ^{58}Ni(^{32}S,α2p)^{84}Zr reaction is shown in Figure 5.10.

The γ-ray transition at 540.0 keV in the spectrum in Figure 5.10 represents the known $2^+_1 \rightarrow 0^+$ transition in ^{84}Zr. The level scheme deduced from the γ rays observed in the spectrum in Figure 5.10 is shown in Figure 5.11. A ground state branching ratio of 0% was assumed. Based on this level scheme, greater than 88% of the ^{84}Nb $\rightarrow$ ^{84}Zr β decay will feed states that depopulate through the 540.0 keV state in ^{84}Zr. A total of 14(9) counts would therefore be expected at this energy in the spectrum in Figure 5.8, based on the number of ^{84}Mo correlated decays observed. Absence of observed γ-ray transitions attributable to β-decay feeding of ^{84}Zr excited states suggests direct feeding feeding to the ground state, a possibility acknowledged in Ref. [34].

The branching ratio into the ground state during ^{84}Nb $\rightarrow$ ^{84}Zr β decay also has

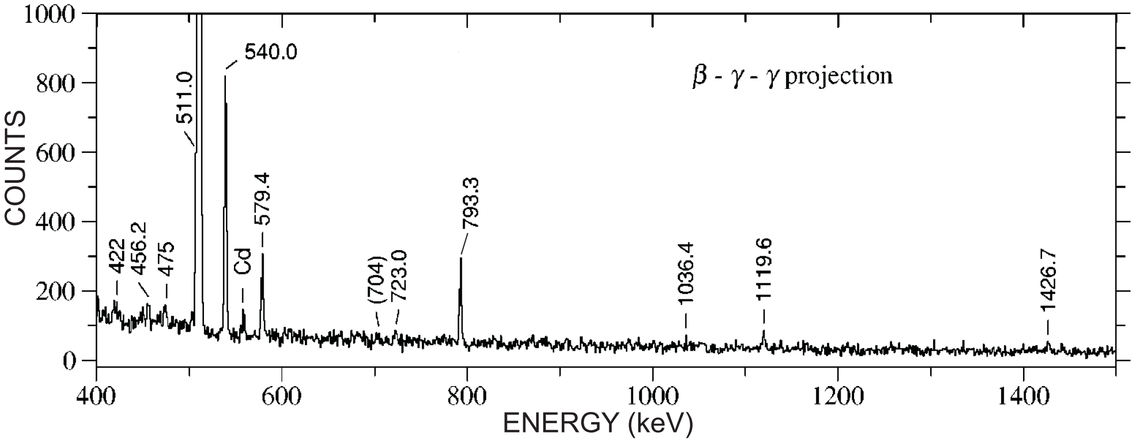

Figure 5.10. The projection of the β-gated γ-γ matrix for $A = 84$ from 400-1400 keV. The peak at 422 keV arises from levels fed in the β decay of $^{83}\mathrm{Y}^{m} \rightarrow {}^{83}\mathrm{Sr}$. The 475-keV peak similarly results from the $^{83}\mathrm{Zr} \rightarrow {}^{83}\mathrm{Y}$ β decay. The peak at 793.3 keV receives counts from levels fed in both the $^{84}\mathrm{Y}^{m} \rightarrow {}^{84}\mathrm{Sr}$ and $^{83}\mathrm{Zr} \rightarrow {}^{83}\mathrm{Y}$ β decays. The label Cd represents the 558.46 keV transition in $^{114}\mathrm{Cd}$ in the sheets of natural Cd placed around the Ge detectors to suppress Pb X-rays. All other energies were assigned to the $^{84}\mathrm{Nb} \rightarrow {}^{84}\mathrm{Zr}$ β decay, with the notable peak at 540.0 keV representing the known $2_1^+ \rightarrow 0^+$ transition in $^{84}\mathrm{Zr}$. Modified from Ref. [34].

implications on the spin assignment of the ^{84}Nb ground state. The logft values in Figure 5.11, which assumed no ground state feeding, were calculated based on branching ratios deduced from the relative intensities of the γ transitions assigned to the ^{84}Zr nucleus, and a half-life of 9.5 s. The calculated logft values for the 2_1^+ and 2_2^+ levels at 540.0 keV and 1119.5 keV, respectively, are less than six, indicating allowed transitions and supporting a positive-parity assignment for the ground state of ^{84}Nb. The logft value for the 4^+ state at 1263.0 keV contradicts possible ground state spins of 1^+ or 2^+, which led to the previous assignment of (3^+) [46, 65, 33, 66]. However, the spin 3^+ level at 1575.7 keV was preferentially fed relative to the 1263.0-keV level in the ^{84}Zr level scheme (see Figure 5.11) implying that the 1263.0-keV state may be populated through γ cascades from β-fed levels not observed in Ref. [34], and extending the possible ^{84}Nb ground state J^π assignment to 2^+ or 3^+.

The implications of direct ^{84}Zr ground state feeding in ^{84}Nb $\rightarrow$ ^{84}Zr β decay must also be considered, based on the absence of γ transitions at 540.0 keV in the spectrum in Figure 5.8. In this scenario, the branching ratios in the ^{84}Zr level scheme (see Figure 5.11) are overestimated and the corresponding logft values are underestimated due to direct feeding of the ^{84}Zr ground state. An increase in the logft values for transitions to the 2_1^+ and 2_2^+ states would classify them as forbidden. However, a positive parity for the ^{84}Nb ground state would still be supported, since direct β feeding to the ground state would suggest allowed decays. Allowed decay to the 0^+ ground state of ^{84}Zr further supports a (1^+) spin assignment for the ^{84}Nb ground state, and is consistent with the generally weak intensities of all the ^{84}Zr γ lines reported in Ref. [34].

To summarize, the absence of γ-ray transitions attributable to β fed states in either ^{84}Nb or ^{84}Zr therefore suggests a majority of the β decay sequence flows through the ground state pathway of ^{84}Mo ($J^\pi = 0^+$) $\rightarrow$ ^{84}Nb ($J^\pi = (1^+)$) $\rightarrow$ ^{84}Zr ($J^\pi = 0^+$).

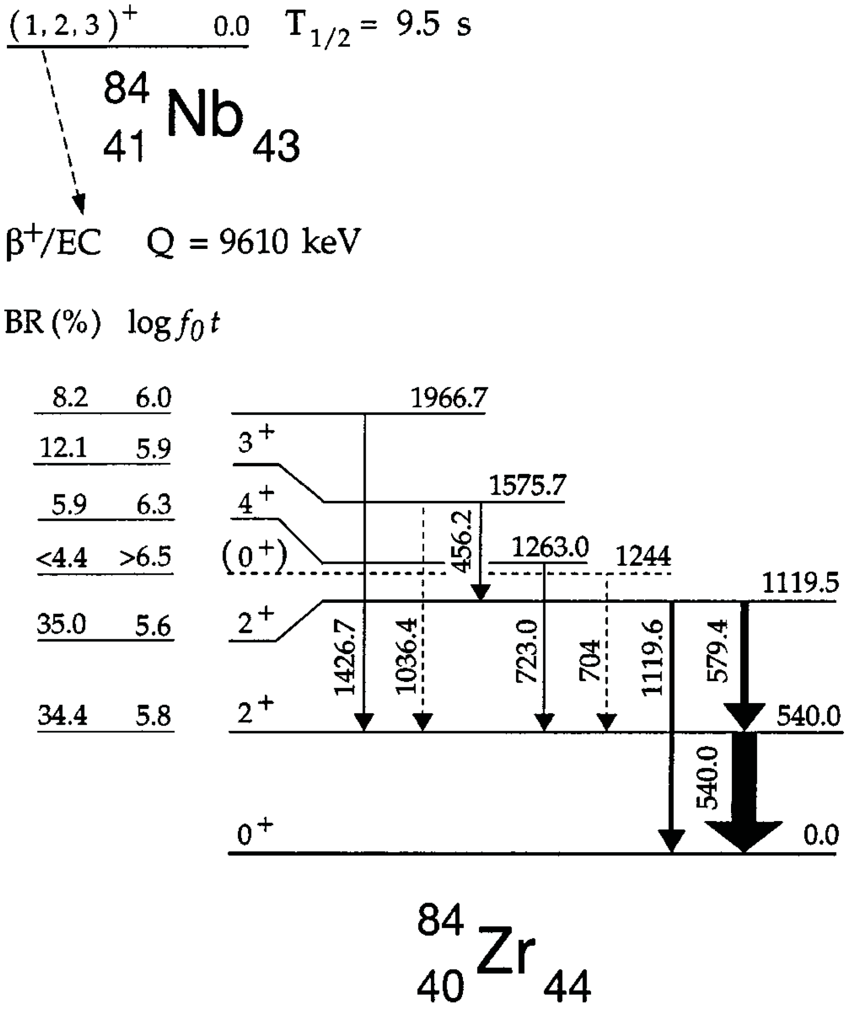

Figure 5.11. β decay level scheme of ^{84}Nb → ^{84}Zr. Logft values are determined from relative branching ratios that assume no ground state feeding. Transitions indicated by a dashed line have been placed tentatively. Taken from Ref. [34]

5.3.3 DSSD Implantation Profiles

The previous discussion in Sec. 5.1 indicated that a correlation time of 20 s was well below the average rate of implantations into a given DSSD pixel. However, two considerations were mentioned: half of the ^{84}Mo implantations would occur within less than 120 s of another implantation; and, the half-life of the isotope implanted within the correlation time impacts the probability for a false correlation. Both of these considerations were investigated.

To address the first consideration, the times of each implantation were tracked up to 20 s prior to each ^{84}Mo implantation. In total, 32% of the ^{84}Mo implantations occurred within 20 s following another implantation (back-to-back implantation) for a given pixel. The time distribution of those ^{84}Mo implantations relative to another implantation is described by the relation re^{-rt}, where r is the rate of implantations into a single pixel and t is the time between a ^{84}Mo and another implantation. The fraction of implantations that should occur within 20 s prior to a ^{84}Mo implantation is given by the integral:

$$\int_0^{20} re^{rt}\mathrm{d}t \tag{5.18}$$

Evaluation of equation (5.18) determined that ∼16% of the ^{84}Mo implantations should occur within 20 s following another implantation, based on the average rate of one implantation per 120 s per pixel. As noted earlier, the implantation profile over the face of the DSSD was not uniform. The implantation profile on the face of the DSSD for ^{84}Mo compared with that for all fragments is shown in Figure 5.3, and demonstrate that the location of ^{84}Mo on the face of the DSSD was roughly congruent with the majority of the implanted isotopes. This geometric overlap of ^{84}Mo with the bulk of the implantations explains why two times the number of back-to-back implantations occurred over that expected from the average rate of implantations per pixel.

In response to the second consideration, the DSSD profile was generated for each major isotope in this study. The RFFS-induced vertical displacement was unique for each isotope and determined the implantation profile observed on the face of the DSSD. The relative positions of ^{80}Y and ^{79}Sr, the two most abundantly produced fragments in this study, were shown in Figure 5.4. ^{80}Y was the most prolifically produced fragment and dominated the character of the overall implantation profile; ^{80}Y implantations also overlapped strongly with the ^{84}Mo implantation profile, whereas ^{79}Sr did not. An analysis of implantation times relative to ^{84}Mo implantations was completed to determine the identities of each isotope implanted back-to-back with ^{84}Mo. ^{80}Y accounted for $\sim$51% of these back-to-back implantations, while $\sim$36% were attributable to ^{73}As. Not a single back-to-back implantation was attributable to ^{79}Sr. The half-life of ^{73}As is $\sim$80 days, so back-to-back implantations with ^{73}As will not result in a false correlation and were ignored. The possible contribution of ^{80}Y to false correlations is more complex. An ^{80}Y back-to-back implantation within 20 s occurred for 16% of the ^{84}Mo implantations (8% for a 10 s correlation time). ^{80}Y also has two β-decaying states. The isomeric 1^- state of ^{80}Y decays with a half-life of 4.7(3) s, whereas the 4^- ground state has a half-life of 30.1(5) s. Decays from the ^{80}Y ground state, therefore, would not be a large contributor to false correlations. The isomeric decay is more problematic, due to its shorter half-life. Assessment of the ^{80}Y impact on the ^{84}Mo correlation therefore requires knowledge of the isomer/ground state production ratio. The amount of ^{80}Y in the isomeric state is directly related to the rate of the background decays out of that state. Too high of a rate would result in a background that could not be assumed to be random/flat within t_c.

The level scheme for ^{80}Y β decay from the 4^- ground state and 1^- isomer is shown in Figure 5.12. The 1^- isomeric state also decays via a 229 keV isomeric transition to the 4^- ^{80}Y ground state. This back-to-back implantation analysis concerned only the fraction of ^{80}Y that β decays out of the 1^- isomeric state. The β-decay branching ratios and half-lives from each state are shown. Greater than 99% of all the β-decay

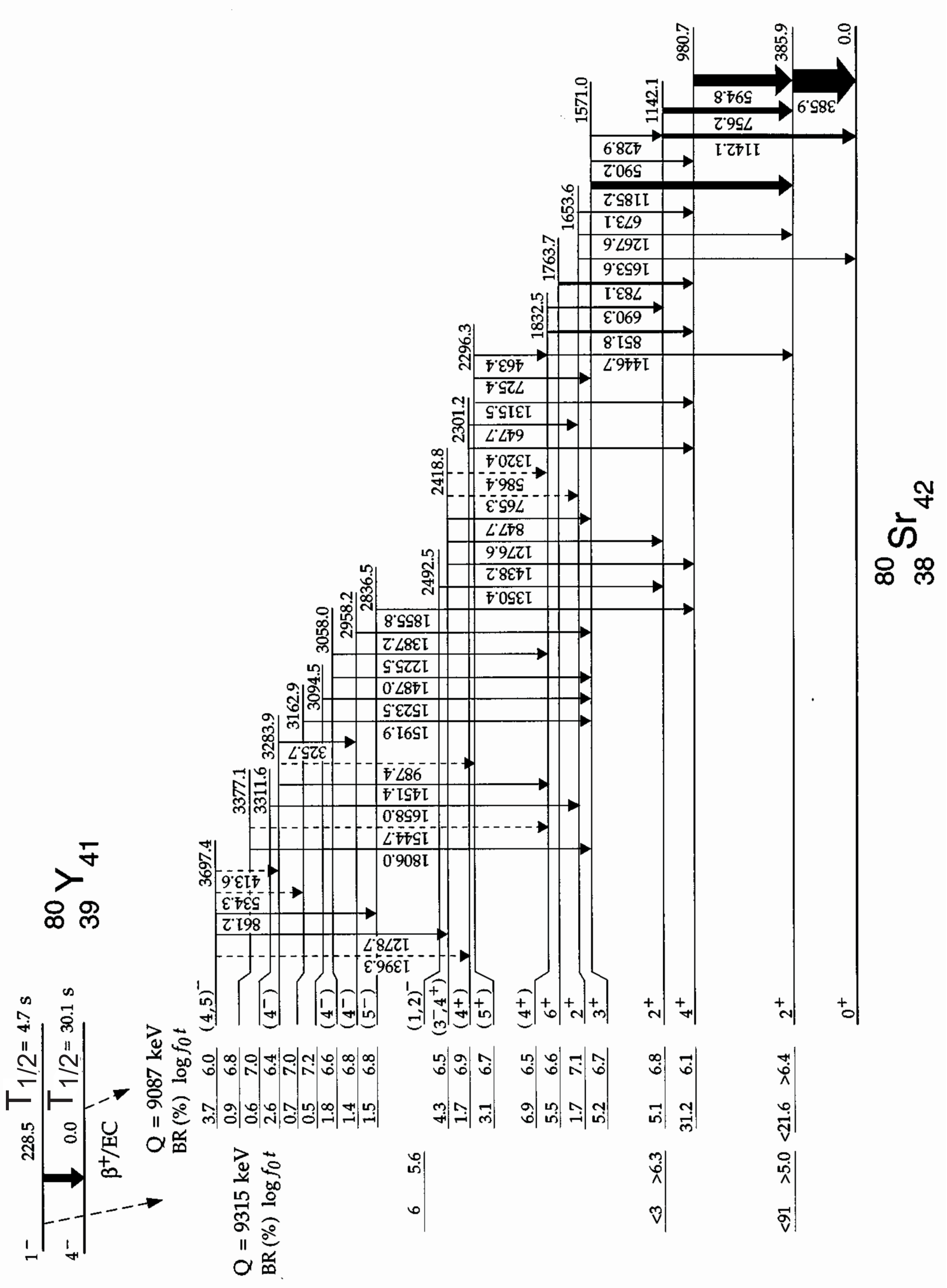

Figure 5.12. β decay level scheme of ^{80}Y → ^{80}Sr. Transitions indicated by a dashed line have been placed tentatively. Taken from Ref. [54]

branching from the ^{80}Y ground state reaches the 386 keV 2_1^+ state either directly or via γ cascade. However, both the ^{80}Y 1^- isomer and the ground state decay feed ^{80}Sr levels that eventually populate the 2_1^+ state in ^{80}Sr, which decays to the ground state via a 386 keV γ-ray transition. A state in ^{80}Sr that is uniquely fed via β decay from either the 4^- ground state or 1^- isomer is required to determine the relative amounts of each decay pathway. The 981 keV 4_1^+ state in ^{80}Sr is populated either directly or via γ cascade by ~53% of the states in ^{80}Sr fed from β decay from the ^{80}Y ground state. Feeding of the 4^+ state is not expected following decay of the 1^- state of ^{80}Y. The 4_1^+ state in ^{80}Sr decays to the 2_1^+ state via a 595-keV γ-ray transition, therefore, the intensity of the 595-keV peak can be fully attributed to γ decay from states fed by the ^{80}Y ground-state β decay. The intensity of the 595 keV γ-ray transition is given by $A_{595}/\varepsilon_{\gamma 595}$, where A_{595} represents the intensity of the transition at 595 keV and $\varepsilon_{\gamma 595}$ represents the absolute efficiency of SeGA at 595 keV. This 595-keV intensity can be normalized to the full γ-ray intensity attributable to decay from the ^{80}Y ground state by dividing by the β-branching ratio (~0.53) that reaches the 981-keV ^{80}Sr level either directly or via γ cascade. A similar normalization to the full γ-ray intensity could be performed for the 386-keV transition except that the portion of the 386-keV intensity attributable to just the ^{80}Y ground state is not known. However, both the absolute SeGA efficiency at 386 keV ($\varepsilon_{\gamma 386}$) and the ^{80}Y ground state branching through the 386 keV state are known. Therefore, the intensity of the 386-keV transition (A_{386}) attributable to the ^{80}Y ground state [$A_{386(g.s.)}$] can be roughly determined by equating the two normalized equations as:

$$\left(\frac{A_{595}}{\varepsilon_{\gamma 595}}\right)\frac{1}{0.53} = \left(\frac{A_{386(g.s.)}}{\varepsilon_{\gamma 386}}\right)\frac{1}{0.99} \tag{5.19}$$

The value of $A_{386(g.s.)}$ determined from this relation represents ~91% of the total I_{386}. Therefore, the 1^- isomeric state, with half-life 4.7(3), accounts for ~9% of the total ^{80}Y β decays. Consequently, a β decay from the 1^- ^{80}Y isomeric state occurred for only 1.4% (0.7% for 10 s correlation time) of the ^{84}Mo implantations.

The contribution from the principle source of potential false correlations was then small. Considering the background rate in each of the Gaussian, Poisson, and MLH fits as random/flat was therefore appropriate.

5.3.4 Discussion

The new half-life value of ^{84}Mo, deduced as $\mathrm{T}_{1/2} = 2.2(2)$ s, is more than 1σ below the value of $3.7\,^{+1.0}_{-0.8}$ s deduced from 37 implantations by Kienle *et al.* [2]. This shorter value continues the observed systematic trend observed in other re-measurements of half-lives first reported in Ref. [2], as shown in Table 1.1. The previously measured half-lives listed in Table 1.1 are shown in Figure 5.13, with the newly-determined half-life value for ^{84}Mo. The difference in the ^{84}Mo results is more pronounced than that for any of the other re-measurements. This larger deviation may be attributed to low statistics, or other uncertainties in the β-decay chain parameters at the time of the Kienle *et al.* measurement. For instance, the ε_{β}, t_c, and half-lives of the daughter and granddaughter decay generations were needed to perform an MLH analysis of the ^{84}Mo decay chain data. The daughter half-life of 9.5±1.0 s [34], held as a fixed parameter in this study, was not published until two years after the ^{84}Mo half-life was reported by Kienle *et al.* It is likely that Kienle *et al.* employed the previously adopted value of 12±3 s [33] for ^{84}Nb to fit their ^{84}Mo decay data, which would give a half-life for ^{84}Mo that was longer than what would be deduced using a 9.5±1.0 s daughter.

The newly measured half-life can be used to differentiate between the two theoretical treatments of $N = Z$ half-lives at $A = 84$ were initially shown in Figure 1.6. The comparison of the new half-life value of ^{84}Mo with these theoretical results is shown in Figure 5.14. The new half-life is consistent with the previously discussed level density functional employed by Sarriguren *et al.* [21]. The Sarriguren *et al.* half-lives relied on a mean field approximation calculated from density functionals using the

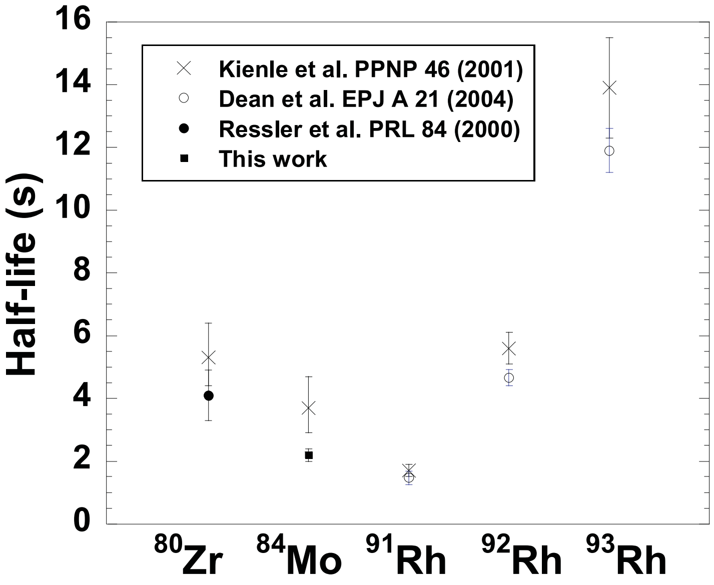

Figure 5.13. Plot of the previously measured half-lives for ^{80}Zr [2, 15] and $^{91-93}$Rh [2, 29], which are listed in Table 1.1, and the previous literature [2] and newly determined half-life values for ^{84}Mo.

level densities of the nuclei of interest. The level density is not directly related to the half-life of a nucleus, so a measured half-life that was inconsistent with their calculation may have implied that their assumptions for other factors, such as the overlap between the initial and final decay states, needed to be revised. The generally good agreement that was observed between the Sarriguren *et al.* calculated half-lives with experimental values is now extended to ^{84}Mo, further demonstrating the robustness of the QRPA approach in this region using the Skyrme and SG2 functionals. The consistency of the newly measured ^{84}Mo half-life with a equilibrium shape calculated from a self-consistent level density affirms the trend towards a spherical ^{100}Sn implied by the measured values of $R_{4/2}$ for ^{84}Mo and ^{88}Ru [19].

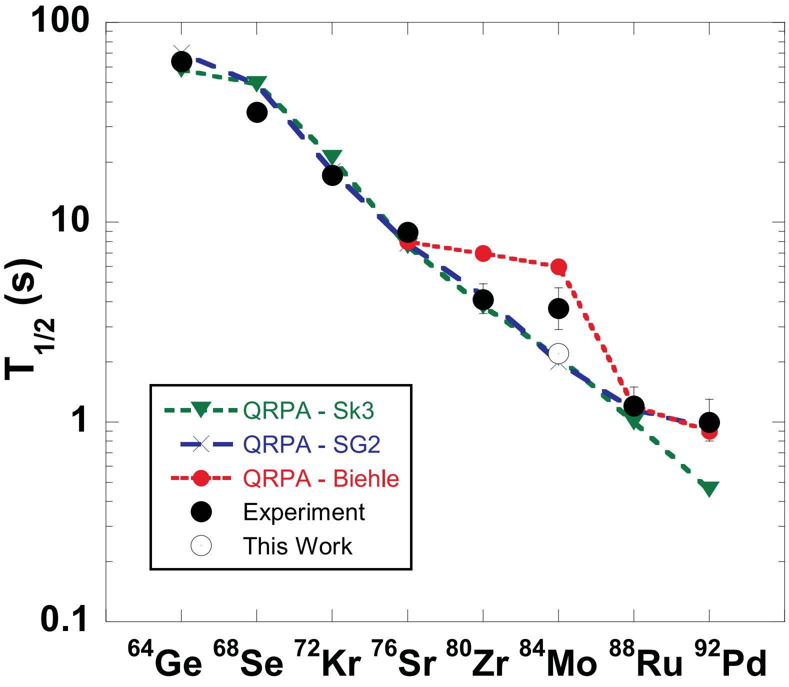

Figure 5.14. The lines show half-lives of even-even $N = Z$ nuclei ($A = 64 - 92$) deduced using the QRPA. Details of different theoretical self-consistent parameters are given in text [21, 22]. The experiment values for $A = 64, 68, 72, 76, 80$ [27], $A = 84, 88, 92$ [2], and this work are shown by the points with error bars.

Astrophysical Implications

The impact of the newly measured ^{84}Mo half-life on the final $A = 84$ abundances produced during the *rp*-process was calculated using a single zone X-ray burst model based on ReaclibV1 rates from the JINA Reaclib online database [68]. The abundance as a function of burst duration is shown in Figure 5.15 for ^{84}Mo (solid lines) and for all $A = 84$ isobars (dashed line). The shaded region results from the range of previously predicted half-lives (0.8 s $\leq$ $T_{1/2}$ $\leq$ 6.0 s) from various models [21, 22, 69]. The dot-dashed line represents the yield calculated using the experimental upper limit of 4.7 s taken from the previously adopted ^{84}Mo $T_{1/2}$. Such time-dependent abundance calculations also rely on the masses of *rp* process nuclei, and will become more accurate as the uncertainties in these masses are reduced [12].

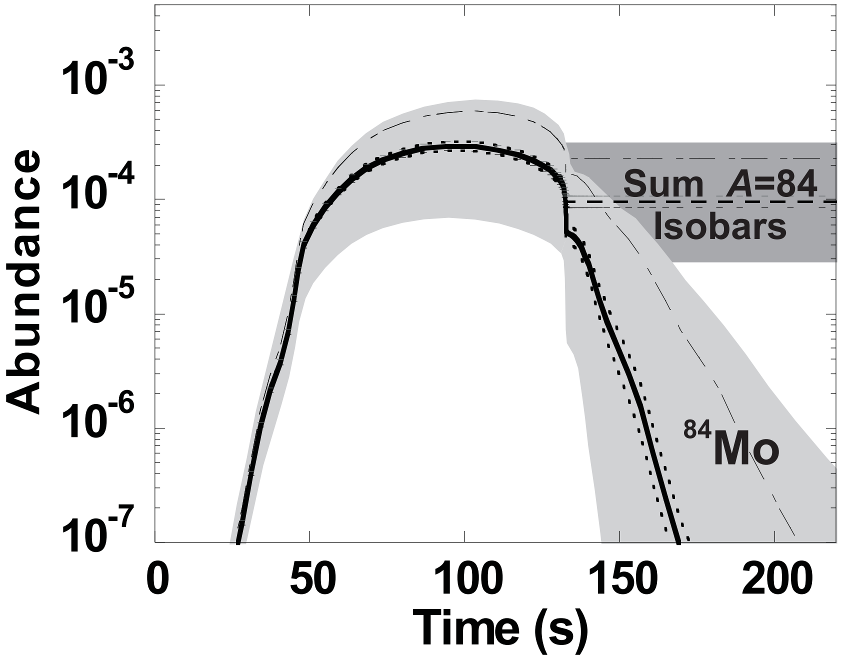

Figure 5.15. Impact of ^{84}Mo half-life on the final $A = 84$ isobar abundance using a single zone X-ray burst calculation. Abundance is reported as a ratio of (mass fraction)/(mass number). Time zero corresponds to the hydrogen-ignition start time. The solid line, bounded above and below with dotted uncertainties, shows the result using the newly-measured ^{84}Mo half life [$T_{1/2} = 2.2(2)$ s]. The dashed line corresponds to summed abundance of all $A = 84$ isobars. The dot-dashed line represents the yield calculated using the experimental upper limit of 4.7 s taken from the previously adopted ^{84}Mo $T_{1/2}$. Shaded regions highlight the range in abundance based on half-lives predicted previously ($0.8 \text{ s} \leq T_{1/2} \leq 6.0 \text{ s}$).

The location of ^{84}Sr as the most proton-rich $A = 84$ stable isobar shields all other $A = 84$ masses from β decay processes from the proton-rich side of the valley of β stability. Therefore, the final abundance for all $A = 84$ isobars is equivalent to the final abundance of ^{84}Sr. The order of magnitude uncertainty in the final ^{84}Sr abundance is reduced to less than a factor 2 with the new, more precise, half-life of ^{84}Mo reported here. The ratio of the mass fraction of an isotope produced in a particular process to its mass fraction in the solar system is called the overproduction factor of an isotope. Assuming the *rp* process was the astrophysical reaction sequence solely responsible for producing ^{84}Sr, then the *rp*-process overproduction factor determined for ^{84}Sr would be larger than that determined for every other isotope. Similarly, if the *rp* process was responsible for the bulk solar production of two or more isotopes, than the overproduction factors for the predominantly synthesized isotopes would need to be large relative to that determined for other isotopes that were not chiefly produced in the *rp* process. The values of the overproduction factors determined for isotopes produced in the *rp* process are given below.

A similar calculation was performed for the abundances of $A = 92$, 94, 96, and 98 isobars. The final abundances of the mass 92, 94, 96, and 98 isobars directly determine the amount of ^{92}Mo, ^{94}Mo, ^{96}Ru, and ^{98}Ru, respectively, that are produced in the *rp* process. ^{92}Mo and ^{96}Ru showed significant overproduction factors in this calculation. The abundances with respect to burst duration are shown in Figure 5.16. The abundances were determined using the newly-measured ^{84}Mo half-life. The isobars are represented by the solid ($A = 92$), dotted ($A = 94$), dashed ($A = 96$), and dash-dot ($A = 98$) lines. The uncertainty in abundances for the $A = 92$, 94, 96, and 98 isobars depends upon the uncertainties for all the rate-determining steps in the *rp*-process reaction sequence prior to $A = 92$; so the abundance uncertainties determined solely from the ^{84}Mo half-life uncertainty are small, and are not included in Figure 5.16. A comparison of the final isobar abundances in Figures 5.15 and

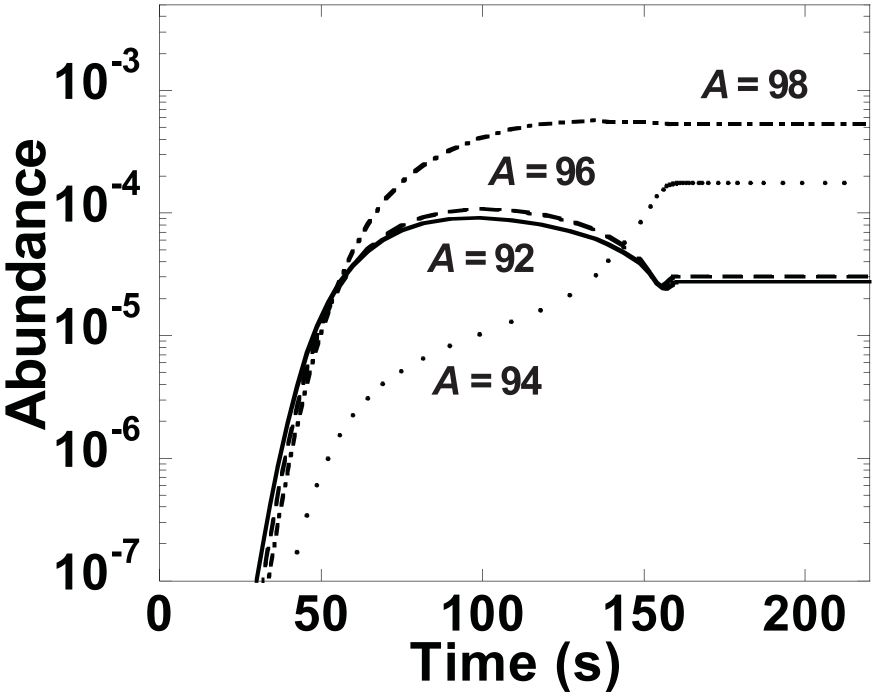

Figure 5.16. Similar to Figure 5.15, except for $A = 92$, 94, 96, and 98. The abundances were determined using the newly-measured ^{84}Mo half life [$T_{1/2}$ = 2.2(2) s]. The isobars are represented by the solid ($A = 92$), dotted ($A = 94$), dashed ($A = 96$), and dash-dot ($A = 98$) lines. The *rp*-process isobar sums for masses 92, 94, 96, and 98 are equivalent to the final abundances of ^{92}Mo, ^{94}Mo, ^{96}Ru, and ^{98}Ru, respectively. Details are in the text.

5.16 reveals that the *rp* process produces amounts for $A = 84, 94$, and 98 are of the same order. Consequently, this simulation was extended to determining the *rp*-process overproduction factors. Considerations of the *rp* process as a source of solar production for ^{94}Mo and ^{98}Ru must also include ^{84}Sr, if the overproduction factors are of the same order.

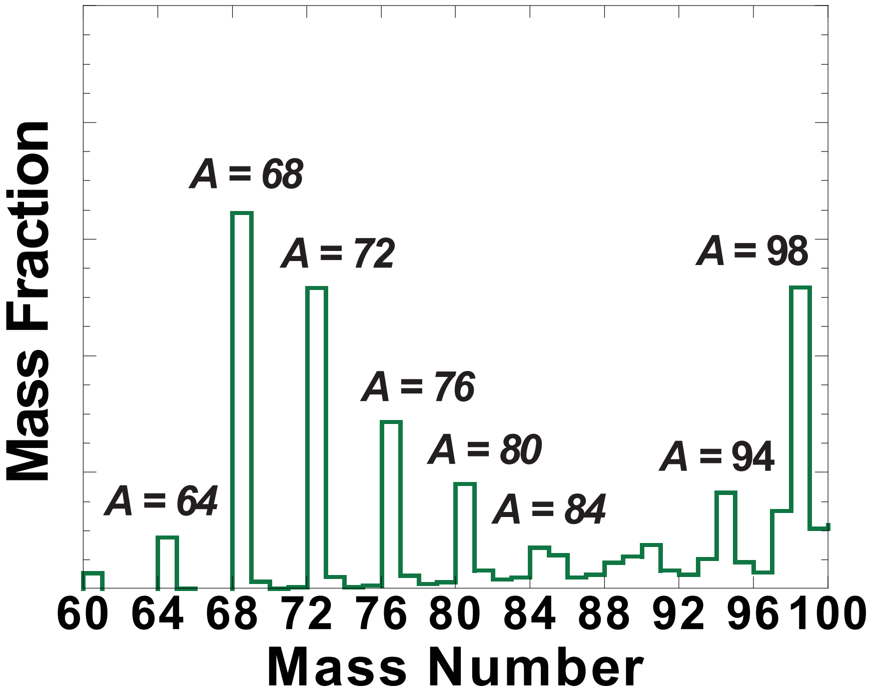

Figure 5.17. Plot of mass fractions from $A = 60 - 100$ determined from a single zone X-ray burst *rp*-process simulation.

A plot of the mass fractions with respect to the total *rp*-process yield shows which isotopes were the most prolifically produced. Figure 5.17 is a plot of the mass fractions of species produced in a single zone X-ray burst simulation with $A = 60 - 100$. The peaks at mass 64, 68, 72, 76, 80, and 84 correspond to the *p*-nuclei produced from β decay out of the *rp*-process waiting points ^{64}Ge, ^{68}Se, ^{72}Kr, ^{76}Sr, ^{80}Zr, and ^{84}Mo. The peaks at $A = 94$ and $A = 98$ represent the mass fraction attributed to the nuclei ^{94}Mo and ^{98}Ru. The *rp*-process overproduction factors for ^{84}Sr, ^{92}Mo, ^{94}Mo, ^{96}Ru,

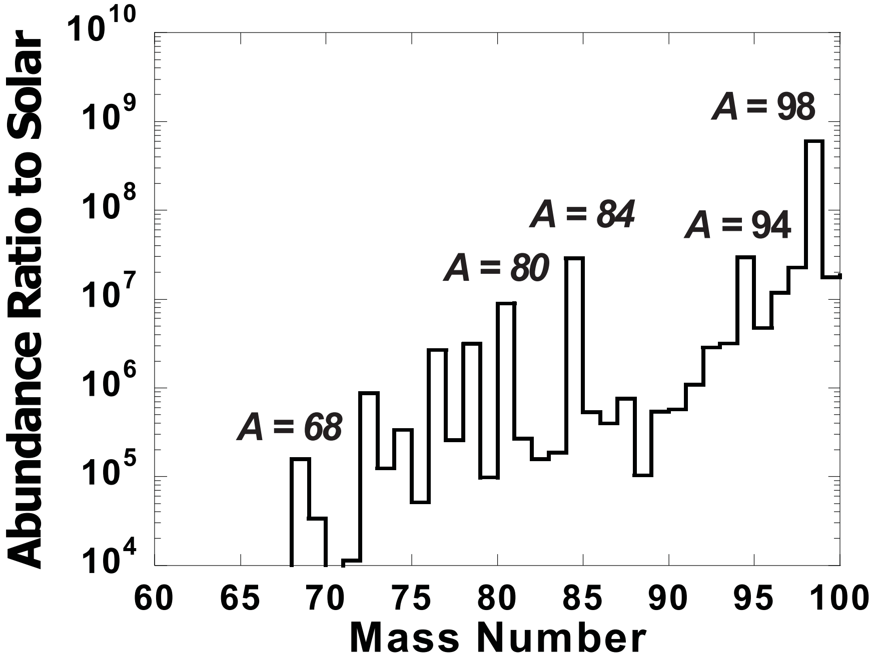

Figure 5.18. Plot of overproduction factors for $A = 60-100$ determined from the ratio of mass abundances, calculated from a single zone X-ray burst *rp*-process simulation, to solar abundances.

and ^{98}Ru were determined from the mass fractions shown in Figure 5.17 and known solar abundances [70]. The overproduction factors for the mass range $A = 60-100$ are shown in Figure 5.18. The new ^{84}Mo half-life of 2.2(2) s reported in this work reduces the overproduction factor for $A = 84$ by a factor of 2 relative to that determined using the previous half-life of $3.7^{+1.0}_{-0.8}$ s. However, the direct impact of the new ^{84}Mo half-life on the *rp*-process production of $A = 92$ and above is small. Nevertheless, the $A = 84$ isobar remains one of the more prolifically produced masses in the *rp* process. The plot of the ratio of *rp*-process abundances to known solar abundances, shown in Figure 5.18, demonstrates that the $A = 84, 94$, and 98 isobars receive the highest contribution from the *rp* process, using the conditions specified here, to their solar abundances relative to other masses.

Based on the X-ray burst simulations performed in this work, *rp*-process scenarios with burst duration of order 100 s or greater produce a substantial amount of ^{84}Sr, ^{94}Mo, and ^{98}Ru. It is conceivable that an *rp* process as discussed in this paper would contribute to the solar abundances of these isotopes, though underproduction of ^{92}Mo and ^{98}Ru shown here require additional proton capture reaction mechanisms for the production of *p*-nuclei, which have been proposed [71].

The newly reported half-life is still longer than the 1.1 s value used for simulations in Ref. [1]. A longer half-life leads to a more pronounced bottleneck in a Zr-Nb cycle *rp*-process endpoint than predicted. A measurement of the ^{84}Mo α-separation energy is critical to verify the establishment of a Zr-Nb cycle and the full impact that ^{84}Mo may have on the *rp*-process mass flow. The α-separation energy is determined in part from the calculated mass value for ^{84}Mo. The demonstrated offset between measured and extrapolated masses in this region [12] of up to 1 MeV make a measurement of the α-separation energy especially necessary.

CHAPTER 6

Summary and Outlook

A new half-life of 2.2(2) s has been deduced for the ground state of ^{84}Mo. The ^{84}Mo ions were produced by the fragmentation of a fast ^{124}Xe beam. The isolated ^{84}Mo fragments represented a sample size that was more than 30 times larger than previously realized. The correlation of β decays with beam fragments required a carefully controlled rate of implantations into each DSSD pixel. This was achieved through A1900 filtration coupled with the first application of the RFFS towards selective rate reduction of fast fragmentation beams at NSCL. An overall reduction of order 10^2 was achieved with the RFFS, with principle contaminants being rate reduced of order 10^5, while the rate of the isotope of interest was not affected. The TOF-specific vertical deflection applied to each fragment by the RFFS resulted a unique implantation profile on the face of the DSSD for each fragment. Fragments implanted in the same pixel within t_c of a ^{84}Mo implantation were analyzed to ensure that a random treatment of the background was appropriate.

All nuclei implanted into the DSSD were monitored for prompt and β-delayed γ rays using 16 Ge detectors from SeGA. Prompt γ rays from the known μs isomer in ^{73}As were used to provide unambiguous identification of the isotopes implanted into the DSSD. The half-life for ^{84}Mo was deduced from the decay times of β events correlated with ^{84}Mo fragment implantations. The ^{84}Mo decay curve was fitted considering decay contributions from parent, daughter, and granddaughter decay generations and a random background, taking the daughter and granddaughter decay half-lives as fixed parameters. The new half-life value of 2.2(2) s reinforces the observed trend of re-measured half-lives that are systematically lower than the values originally reported by Kienle *et al.* The 3σ difference from the Kienle *et al.* value with the new value reported in this work is attributed to higher statistics, improved background treatment, and more accurate information on daughter and granddaughter decays.

The ^{84}Mo β-delayed γ rays were analyzed to identify candidate β-delayed γ rays that could be used to isolate the β particles specific to the ^{84}Mo parent decay. Unfortunately, no γ rays attributable to the ^{84}Nb known level structure were identified. Implications on the ^{84}Nb ground state, favoring a $J^{\pi} = 1^{+}$ spin assignment, were presented based on the lack of γ rays observed in the ^{84}Mo β-delayed γ-ray spectrum.

Collecting ^{84}Mo β-decay statistics sufficient for identifying one or more β-decay fed excited states in ^{84}Nb would be valuable for two reasons: First, a ^{84}Mo half-life could be deduced from parent β decays in coincidence with γ-ray transitions out of the ^{84}Nb excited states. This ^{84}Mo half-life deduced from a background-suppressed β-decay histogram would provide a check on the ^{84}Mo half-life determined from the MLH fit algorithm presented in this work. Second, the $\log ft$ values elucidated from the ^{84}Mo β fed excited states in ^{84}Nb would allow characterization of the ^{84}Nb ground and excited states. Collecting the statistics necessary to characterize the ^{84}Mo β-decay fed excited states in ^{84}Nb would probably require an accelerator facility that could produce ^{84}Mo at intensities of order 10 to 100 times more than what was realized in this study. Improving the efficiency of β and γ detection would also aid in improving the number of statistics collected.

The new ^{84}Mo half-life value is in line with the theoretical predictions of Sarriguren *et al.* of the mid-mass $N = Z$ region consistent with a ^{84}Mo nucleus that begins a shape transition towards a spherical ^{100}Sn. ^{84}Mo is an important waiting point in the *rp* process, determining mass abundance at and impacting mass procession above $A = 84$. A measurement of the ^{84}Mo α-separation energy is critical to determine the existence of a Zr-Nb cycle high temperature endpoint and the full impact of ^{84}Mo on the *rp*-process mass flow. Rapid proton capture processes have also been postulated to be aided by neutrino winds, which may reduce the impact of β-decay waiting points on reaction progression to higher masses [72]. The new ^{84}Mo half-life may also be incorporated into such models that occur on accreting neutron stars and in other astrophysical rapid proton reaction environments; most notably would be the rapid proton capture sequences believed to occur in supernovae [6].

APPENDIX A

A.1 β Detection Efficiency

The efficiency for β detection was a fixed parameter for MLH half-life analysis. ε_β was determined from the ratio:

$$\varepsilon_\beta = N_\beta / N_I \tag{A.1}$$

where N_I is the number of implantations observed for a parent nucleus and N_β is the number of parent β events observed within t_c. N_I was determined directly from the number of experimentally observed fragment implantations for a given isotope. N_β was determined by integrating the parent component of the decay curve fits for a given isotope. Equation (2.12):

$$\lambda_1 n_1(t) = \lambda_1 n_1(0) e^{-\lambda_1 t},$$

taken from the Bateman equations, describes the parent contribution to the decay curve. Recall from Equation (2.6) that

$$A = N\lambda.$$

Where A is the activity of the sample, N is the number of nuclei present, and λ is their decay constant. The number of counts observed during an experiment is a product of the activity of the sample and the efficiency of the detector.

$$C = A \cdot \varepsilon_\beta \tag{A.2}$$

A simple substitution of Equation (A.2) into (2.12) yields:

$$C_t = C_0 e^{-\lambda_1 t}. \tag{A.3}$$

N_β was defined as the total number of parent decay events observed from $t = 0$ to $t = t_c$. N_β can therefore be directly determined through the integration of Equation (A.3) from $t = 0$ to $t = t_c$

$$N_\beta = \int_0^{t_c} C_0 e^{-\lambda_1 t} \mathrm{d}t \tag{A.4}$$

where t_c represents the fragment-β correlation time. Equation (A.4) can be simplified to read:

$$N_\beta = \frac{C_0}{\lambda_1}(1 - e^{-\lambda_1 t_c}).$$

Where C_0 represents the number of decays observed from the parent nucleus at $t = 0$. The error in the efficiency is calculated from the relation:

$$\sigma^2_{\varepsilon_\beta} = \left(\frac{\sigma_{N_\beta}}{N_\beta}\right)^2 \varepsilon^2_\beta + \left(\frac{\sigma_{N_I}}{N_I}\right)^2 \varepsilon^2_\beta. \tag{A.5}$$

Where σ_{N_I} and σ_{N_β} are the errors associated with N_I and N_β, respectively. The parameter N_I is taken directly from an experimental measurement. σ_{N_I} was determined solely based on Gaussian statistics from $\sqrt{N_I}$. The uncertainty in N_β depends on the parameters C_0, λ_1, and t_c and was calculated via two different methods. First, via the relation:

$$\sigma^2_{N_\beta} = \left(\frac{\partial N_\beta}{\partial C_0}\right)^2 \sigma^2_{C_0} + \left(\frac{\partial N_\beta}{\partial \lambda_1}\right)^2 \sigma^2_{\lambda_1} + \left(\frac{\partial N_\beta}{\partial t_c}\right)^2 \sigma^2_{t_c}. \tag{A.6}$$

The necessary partial derivatives to evaluate Equation (A.6) are:

$$\frac{\partial N_\beta}{\partial C_0} = \frac{1}{\lambda_1}\left(1 - e^{-\lambda_1 t_c}\right) \tag{A.7}$$

$$\frac{\partial N_\beta}{\partial \lambda_1} = \frac{C_0}{\lambda_1}\left(\frac{-1}{\lambda_1} + \frac{1}{\lambda_1} e^{-\lambda_1 t_c} - t_c e^{-\lambda_1 t_c}\right) \tag{A.8}$$

$$\frac{\partial N_\beta}{\partial t_c} = C_0 e^{-\lambda_1 t_c} \tag{A.9}$$

The second method for evaluating the uncertainty in N_β was to integrate Equation (A.4) using the $\pm 1\sigma$ range of the parameters C_0 and λ_1 to define the upper and lower limits of N_β. For example, the $+1\sigma$ (-1σ) value for N_β was calculated by simultaneously inserting the $C_0 + \sigma_{C_0}$ ($C_0 - \sigma_{C_0}$) and the $\lambda_1 - \sigma_{\lambda_1}$ ($\lambda_1 + \sigma_{\lambda_1}$) into Equation (A.4) and integrating over t_c. The second method produced slightly larger uncertainties for N_β relative to the uncertainties determined through the error propagation formula provided by Equation (A.6). These larger, more conservative values were taken for σ_{N_β}.

The values of ε_β for ^{84}Mo, ^{83}Nb, and ^{81}Zr were deduced from their individual decay curves. These particular nuclei were the only nuclei available which could be reliably correlated (see Table 5.1) based on their known half-lives and the average implantation rate per pixel in this work. The decay curve for each of these nuclei, with time bins of 1 s, was fitted based on the maximization of a Poisson probability distribution function, which was independent of ε_β, that considered contributions from the exponential parent decay and the exponential growth and decay of the daughter, and a linear background. The value of t_c for each decay curve was 20 s, consistent with the t_c used for extracting the ^{84}Mo half-life with the MLH fit. The fit deduced for ^{84}Mo is provided in Figure A.1. Values of 282(47), 1.8(3) s, and 0.27(5) were obtained for N_β, $T_{1/2}$, and ε_β, respectively, using Equation (A.6) to determine the uncertainty for N_β. By integrating Equation (A.4) using the $\pm 1\sigma$ range of the parameters C_0 and λ_1, values of 282(66) and 0.27(6) were obtained for N_β and ε_β, respectively.

The decay curve obtained for ^{83}Nb is shown in Figure A.2. A daughter half-life of 37.8 s [73] was taken as a fixed parameter. The granddaughter had a long $T_{1/2}$ and was effectively included in the background. The correlation time for ^{83}Nb was taken as 20 s, and decays and implantations were correlated using a 5-pixel search geometry. Values of 5927(378) and 0.29(2) were obtained for N_β and ε_β, respectively,

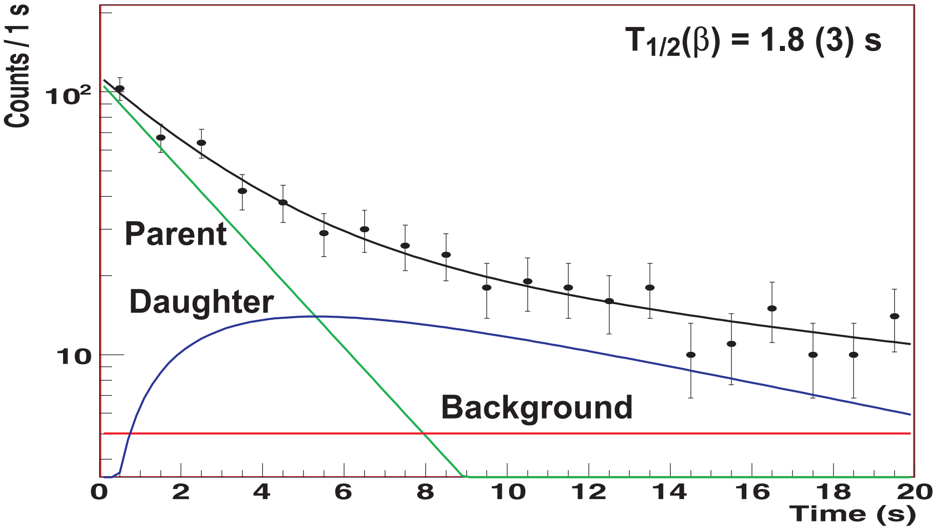

Figure A.1. Similar to Figure 5.6. A daughter half-life of 9.5 s was taken as a fixed parameter. The initial activity, parent decay constant, and background were free parameters in the fit.

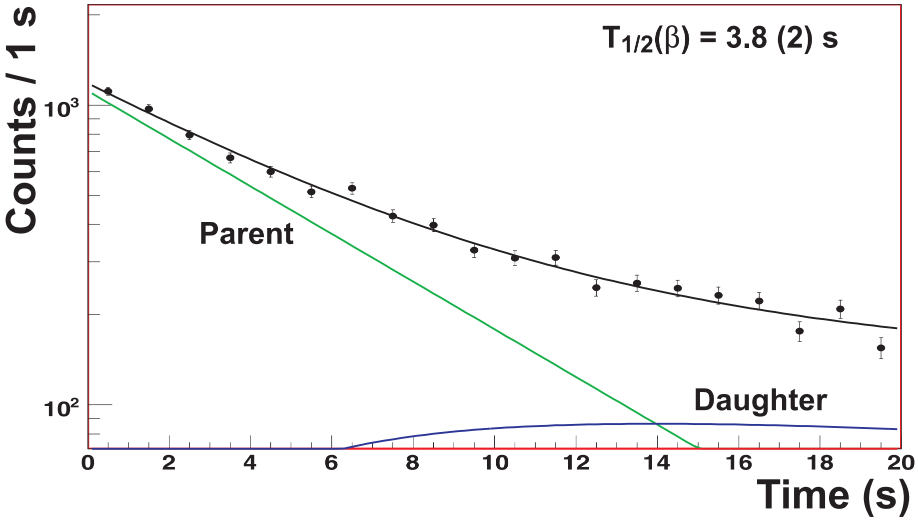

Figure A.2. Similar to Figure 5.6, except for ^{83}Nb. A daughter half-life of 37.8 s was taken as a fixed parameter. The initial activity, parent decay constant, and background were free parameters in the fit. The fitted background rate of < 70 counts/s lies below the horizontal axis.

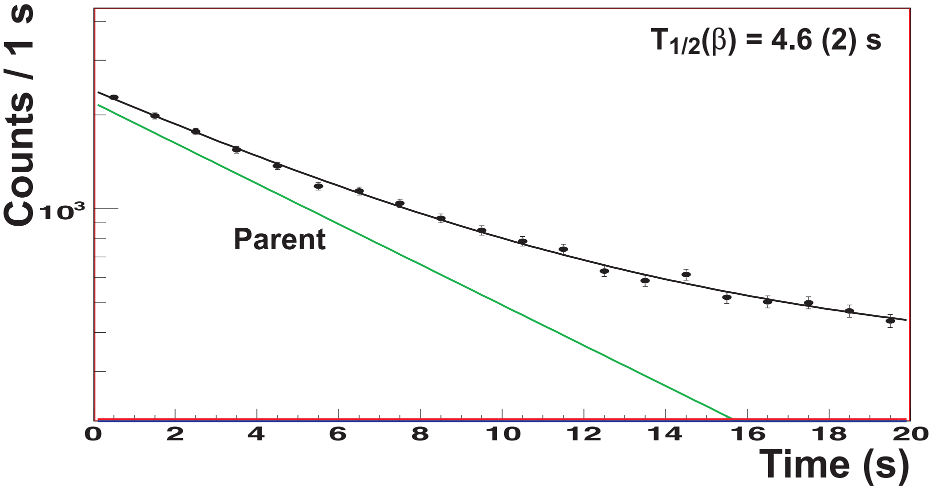

Figure A.3. Similar to Figure 5.6, except for ^{81}Zr. A daughter half-life of 72.0 s was taken as a fixed parameter. The initial activity, parent decay constant, and background were free parameters in the fit. The exponential growth and decay of the daughter and the fitted background rate of ∼100 counts/s both lie below the horizontal axis.

using Equation (A.6) to determine the uncertainty for N_β. By integrating Equation (A.4) using the $\pm 1\sigma$ range of the parameters C_0 and λ_1, values of 5927(454) and 0.29(2) were obtained for N_β and ε_β, respectively. The half-life of 3.8(2) s deduced for ^{83}Nb is in good agreement with the previously reported value of 4.1(3) s [51]. The parameters deduced for ^{83}Nb are summarized in Table A.1.

The decay curve obtained for ^{81}Zr is provided in Figure A.3. A daughter half-life of 72.0 s [55] was taken as a fixed parameter. The correlation time for ^{81}Zr was taken to be 20 s, and decays and implantations were correlated using a 5-pixel search geometry. Values of 13900(746) and 0.37(2) were obtained for N_β and ε_β, respectively, using Equation (A.6) to determine the uncertainty for N_β. By integrating Equation (A.4) using the $\pm 1\sigma$ range of the parameters C_0 and λ_1, values of 13900(795) and 0.37(2) were obtained for N_β and ε_β, respectively. The half-life of 4.6(2) s deduced for ^{81}Zr agrees, within error, with the previously reported value of 5.3(5) s. The parameters deduced for ^{81}Zr are summarized in Table A.1.

The total ε_β, was computed from the weighted average of the ε_β deduced individually for ^{84}Mo, ^{83}Nb, and ^{81}Zr. The parameters deduced for the individual isotopes that were used to determine the total ε_β are summarized in Table A.1. The values and uncertainties for the parameters N_β and ε_β provided in Table A.1 were determined using the above mentioned method of integrating Equation (A.4) using the ±1σ range of the parameters C_0 and λ_1.

Table A.1. Parameters for determining ε_β. The $T_{1/2}$ and N_β parameters were deduced from the decay curves in Figures A.1, A.2, and A.3 for the nuclei ^{84}Mo, ^{83}Nb, and ^{81}Zr, respectively. The uncertainties in the N_β were determined by integrating Equation (A.4) using the ±1σ range of the parameters C_0 and λ_1. The N_I were determined directly from the number of fragments identified for each isotope from the particle identification plot.

Isotope	$T_{1/2}$ (s)	N_β	N_I	ε_β
^{84}Mo	1.8(3)	282(66)	1037(32)	0.27(6)
^{83}Nb	3.8(2)	5927(454)	20121(142)	0.29(2)
^{81}Zr	4.6(2)	13900(795)	37246(193)	0.37(2)
Weighted Average				0.34(2)

BIBLIOGRAPHY

[1] H. Schatz, A. Aprahamian, J. Gorres, M. Weischer T. Rauscher, J F Rembges, F K Thielemann, B Pfeiffer, P Moller, K L Kratz, H Herndl, B A Brown, and H Rebel. *Phys. Rep.* **294**:167, 1998.

[2] P. Kienle, T. Faestermann, J. Friese, H. J. Korner, M. Munch, R. Schneider, A. Stolz, E. Wefers, H. Geissel, G. Munzenberg, *et al. Prog. Part. Nucl. Phys.* **46**:73, 2001.

[3] J. I. Prisciandaro, A. C. Morton, and P. F. Mantica. *Nucl. Instrum. and Methods A* **505**:140–143, 2003.

[4] W. F. Mueller, J. A. Church, T. Glasmacher, D. Gutknecht, G. Hackman, P. G. Hansen, Z. Hu, K. L. Miller, and P. Quirin. *Nucl. Instrum. and Methods A* **466**:492, 2001.

[5] D. Gorelov, V. Andreev, D. Bazin, M. Doleans, T. Grimm, F. Marti, J. Vincent, and X. Wu. *RF-Kicker System for Secondary Beams at the NSCL.* In C. Horak, editor, *Proceedings of 2005 Particle Accelerator Conference*, page 3880. Knoxville, TN, 2005.

[6] E. M. Burbidge, G. R. Burbidge, W. A. Fowler, and F. Hoyle. *Rev. Mod. Phys.* **29**(4):547, 1957.

[7] J. Grindlay and H. Gursky. *Astrophys. J. Lett.* **205**:L127, 1976.

[8] J. Jose. *Nucl. Phys. A* **752**:540c, 2005.

[9] H. Schatz. *Nucl. Phys. A* **746**:347c, 2004.

[10] H. Schatz, A. Aprahamian, V. Barnard, L. Bildstein, A. Cumming, M. Oullette, T. Rauscher, F K Thielemann, and M. Wiescher. *Phys. Rev. Lett.* **86**:3471, 2001.

[11] R. Hynes. Http://www.phys.lsu.edu/ rih/.

[12] A. Kankainen, L. Batist, S. A. Eliseev, V. V. Elomaa, T. Eronen, U. Hager, J. Hakala, A. Jokinen, I. Moore, Yu. N. Novikov, *et al. Eur. Phys. J. A* **29**:271, 2006.

[13] N. Weinberg, L. Bildstein, and H. Schatz. *Astrophys. J.* **639**:1018, 2006.

[14] R. N. Boyd. *Eur. Phys. J. A* **13**:203, 2002.

[15] J. J. Ressler *et al. Phys. Rev. Lett.* **84**(10):2104, 2000.

[16] W. Walters. *Beta Decay Half-Life of* ^{84}*Mo*, 1998. Proposal to the Holifield Radioactive Ion Beam Facility.

[17] R. F. Casten, N. V. Zamfir, and D. S. Brenner. *Phys. Rev. Lett.* **71**(2):227, 1993.

[18] D. Bucurescu, C. Rossi Alverez, C. A. Ur, N. Marginean, P. Spolaore, D. Bazzacco, S. Lunardi, D. R. Napoli, M. Ionescu-Bujor, A. Iordaschescu, *et al. Phys. Rev. C* **56**(5):2497, 1997.

[19] N. Marginean, C. Rossi Alvarez, D. Bucurescu, C. A. Ur, A. Gadea, S. Lundardi, D. Bazzacco, G. de Angelis, M. Axiotis, M. De poli, *et al. Phys. Rev. C* **63**(031303), 2001.

[20] N. Marginean. *Eur. Phys. J. A* **20**:123, 2004.

[21] P. Sarriguren, R. Alvarez-Rodriguez, and E. Moya de Guerra. *Eur. Phys. J. A* **24**:193, 2005.

[22] G. T. Biehle and P. Vogel. *Phys. Rev. C* **46**(4):1555, 1992.

[23] E. J. Kaptein, H. P. Blok, L. Hulstman, and J. Blok. *Nucl. Phys. A* **260**:141, 1976.

[24] M. K. Kabadiyski, C. J. Gross, A. Harder, K. P. Lieb, D. Rudolph, M. Weiszflog, J. Altmann, A. Dewald, J. Eberth, T. Mylaeus, H. Grawe, J. Heese, and K. H. Maier. *Nucl. Phys. A* **260**:141, 1976.

[25] C. Lingk, A. Jungclaus, D. Kast, K. P. Lieb, C. Teich, M. Weiszflog, C. Ender, T. Hartlein, F. Kock, D. Schwalm, *et al. Phys. Rev. C* **56**(5), 1997.

[26] C. Plettner, H. Grawe, I. Mukha, J. Doring, F. Nowacki, L. Batist, A. Blazhev, C. R. Hoffman, Z. Janas, R. Kirchner, *et al. Nucl. Phys. A* **733**:20, 2004.

[27] G. Audi, O. Bersillon, J. Blachot, and A. H. Wapstra. *Nucl. Phys. A* **729**:3, 2003.

[28] E. Wefers. *Zerălle extrem neutronenarmer Kerne unterhalb von* ^{100}*Sn.* Ph.D. thesis, Technischen Universitat Munchen, 2001.

[29] S. Dean, M. Gorska, F. Aksouh, H. de Witte, M. Facina, M. Huyse, O. Ivanov, K. Krouglov, Yu Kudryavtsev, I. Mukha, *et al. Eur. Phys. J. A* **21**:243, 2004.

[30] R. Schneider. *Nachweis und Untersuchung des Zerfalls von ^{100}Sn und benachbarter Kerne.* Ph.D. thesis, Technischen Universitat Munchen, 1996.

[31] C. Longour, J. G. Narro, B. Blank, M. Lewitowicz, Ch. Miehe, P. H. Regan, D. Applebe, L. Axelsson, A. M. Bruce, W. N. Catford, *et al.* *Phys. Rev. Lett.* **81**(16):3337, 1998.

[32] J. Uusitalo, D. Seweryniak, P. F. Mantica, J. Rikovska, D. S. Brenner, M. Huhta, J. Greene, J. J. Ressler, B. Tomlin, C. N. Davids, *et al.* *Phys. Rev. C* **57**(5):2259, 1998.

[33] G. Korschinek, E. Nolte, H. Hick, K. Miyano, W. Kutschera, and H. Morinaga. *Z. Phys. A* **281**(409), 1977.

[34] J. Doring, R. A. Kaye, A. Aprahamian, M. W. Cooper, J. Daly, C. N. Davids, R. C. de Haan, J. Gorres, S. R. Lesher, J. J. Ressler, *et al.* *Phys. Rev. C* **67**(014315), 2003.

[35] G. Friedlander, J. W. Kennedy, E. S. Macias, and J. M. Miller. *Nuclear and Radiochemistry.* John Wiley & Sons, 1981.

[36] H. Bateman. *Proc. Cambridge Phil. Soc.* **15**:423, 1910.

[37] W. Loveland, D. J. Morrissey, and G. T. Seaborg. *Modern Nuclear Chemistry*, page 420. John Wiley & Sons, Inc., 2005.

[38] R. Pfaff, D. J. Morrissey, W. Benenson, M. Fauerbach, M. Hellstrom, C. F. Powell, B. M. Sherrill, M. Steiner, and J. A. Winger. *Phys. Rev. C* **53**(4):1753, 1996.

[39] D. J. Morrissey, B. M. Sherrill, M. Steiner, A. Stolz, and I. Wiedenhoever. *Nucl. Instrum. and Methods B* **204**:90, 2003.

[40] O. Tarasov, D. Bazin, M. Lewitowicz, and O. Sorlin. *Nucl. Phys. A* **701**:661, 2002.

[41] S. N. Liddick. *Beta-Decay Studies of Neutron-Rich Nuclides and the Possibility of an $N = 34$ Subshell Closure.* Ph.D. thesis, Michigan State University, 2004.

[42] O. B. Tarasov and D. Bazin. *Nucl. Phys. A* **746**:411c, 2004.

[43] R. G. Helmer and C. van der Leun. *NIM A* **450**:35, 2000.

[44] C. W. Reich and R. G. Helmer. *Nucl. Data Shts. $A = 154$* **85**(2):171, 1998.

[45] C. W. Reich. *Nucl. Data Shts. $A = 155$* **104**(1):1, 2005.

[46] L. P. Ekstrom and R. B. Firestone. *WWW Table of Radioactive Isotopes, database version 2/28/99.* Http://ie.lbl.gov/toi/index.htm.

[47] J. Katakura. *Nucl. Data Shts. A = 125* **86**(955):1, 1999.

[48] W. T. Milner. *DAMM.TXX.* Oak Ridge National Laboratory, unpublished.

[49] D. Quitmann, J. M. Jaklevic, and D. A. Shirley. *Phys. Lett. B* **30**(5):329, 1969.

[50] T. Faestermann. *Astrophys. J. A* **15**:185, 2002.

[51] T. Kuroyanagi, S. Mitarai, B. J. Min, H. Tomura, Y. Haruta, K. Heiguchi, S. Suematsu, and Y. Onizuka. *Nucl. Phys. A* **484**:264, 1988.

[52] C. F. Liang *et al. Z. Phys A* **309**:185, 1982.

[53] W. X. Huang, R. C. Ma, X. J. Xu, S. W. Xu, Y. X. Xie, Z. K. Li, Y. X. Ge, Y. Y. Wang, C. F. Wang, T. M. Zhang, *et al. Z. Phys. A* **359**:349, 1997.

[54] J. Doring, A. Aprahamian, R. C. de Haan, J. Gorres, H. Schatz, M. Wiescher, W. B. Walters, L. T. Brown, C. N. Davids, C. J. Lister, and D. Seweryniak. *Phys. Rev. C* **59**(1):59, 1999.

[55] C. J. Lister, P. E. Haustein, D. E. Alburger, and J. W. Olness. *Phys. Rev. C* **24**(1):1981, 1981.

[56] R. K. Girgis, R. A. Ricci, and R. van Lieshout. *Nucl. Phys.* **13**:473, 1959.

[57] J. Kyles, J. C. McGeorge, F. Shaikh, and J. Byrne. *Nucl. Phys. A* **150**:143, 1970.

[58] J. A. Rice. *Mathematical Statistics and Data Analysis.* Wadsworth-Brooks Cole, 1995.

[59] G. F. Grinyer. *High Precision Measurements of* ^{26}*Na* β^- *Decay.* Master's thesis, The University of Guelph, 2004.

[60] G. F. Knoll. *Radiation Detection and Measurement*, page 787. John Wiley & Sons, Inc., 2000.

[61] P. T. Hosmer, H. Schatz, A. Aprahamian, O. Arndt, R. R. C. Clement, A. Estrade, K. L. Kratz, S. N. Liddick, P. F. Mantica, W. F. Mueller, *et al. Phys. Rev. Lett.* **94**(112501), 2005.

[62] D. Bazin, F. Montes, A. Becerril, G. Lorusso, A. Amthor, T. Baumann, H. Crawford, A. Estrade, A. Gade, T. Ginter, C. J. Guess, *et al. Phys. Rev. Lett.* , (accepted).

[63] A. Stolz. *Untersuchung des Gamov-Teller-Zerfalls in der Nachbarschaft von* ^{100}Sn. Ph.D. thesis, Technischen Universitat Munchen, 2001.

[64] S. K. Saha, P. E. Haustein, D. E. Alburger, C. J. Lister, J. W. Olness, R. A. Dewberry, and R. A. Naumann. *Phys. Rev. C* **26**(6):2654, 1982.

[65] N. Marginean, D. Bucurescu, C. A. Ur, D. Bazzacco, S. M. Lenzi, S. Lundardi, C. Rossi Alvarez, M. Ionescu-Bujur, G. de Angelis, M. De Poli, *et al. Eur. Phys. J. A* **4**:311, 1999.

[66] J. K. Tuli. *Nucl. Data Shts. A = 84* **81**(331):331, 1997.

[67] C. Chandler, P. H. Regan, B. Blank, C. J. Pearson, A. M. Bruce, W. N. Catford, N. Curtis, S. Czajkowski, Ph. Dessagne, A. Fleury, *et al. Phys. Rev. C* **61**(044309), 2000.

[68] S. Warren. Http://www.nscl.msu.edu/∼nero/db.

[69] K. Takahashi and K. Yokoi. *Nucl. Phys. A* **404**:578, 1983.

[70] M. Asplund, N. Grevesse, and J. Sauval. *Nucl. Phys. A* **777**:1, 2006.

[71] J. Pruet, R. D. Hoffman, S. E. Woosley, H. T. Janka, and R. Buras. *Astrophys. J.* **644**:1028, 2006.

[72] C. Frohlich, G. Martinez-Pinedo, M. Liebendorfer, F. K. Thielmann, E. Bravo, W. R. Hix, K. Langanke, and N. T. Zinner. *Phys. Rev. Lett.* **96**(142502), 2006.

[73] E. Hagberg, J. C. Hardy, H. Schmeing, E. T. H. Clifford, and V. T. Koslowsky. *Nucl. Phys. A* **395**:152, 1983.